Study of Skimming Flow in Flat Slope Stepped Channels

Author: Daniel López de Mesa Aguilar
Director: Evelio Andrés Gómez Giraldo, Ph.D.

Universidad Nacional de Colombia - Sede Medellín
Master's Thesis
Program: Maestría en Ingeniería de Recursos Hidráulicos
2017

Contents

List of Figures

List of Tables

To my parents, my brother, Melissa and Juanita
for their unconditional love and constant support

Acknowledgements

I want to start by thanking God for everything.

I thank Professor Andrés Gómez in a special way for his guidance, support and willingness in the development of this work.

I am very grateful to Melissa, the person who was with me throughout this process, who plays an important role in my life and helped me to achieve this goal.

Study of Skimming Flow in Flat Slope Stepped Channels

Abstract: In this thesis, the results of a numerical modeling study that addresses the skimming flow properties in flat slope stepped channels, are presented and analyzed. Experimental data of mean flow velocity profiles from Hunt and Kadavy's physical model [5, 42] was used for the calibration of the results obtained with a numerical model performed with the commercial CFD tool: Ansys Fluent. $SST\ k-\omega$ was selected for turbulence modeling and Mixture model for the free surface tracking process, but as the flow aeration downstream the inception point wasn't captured by the mentioned models, a "data adjustment procedure" was proposed to be able to compare the experimental data from measuring stations with air entrance, with the numerical results. This work presents a hydrodynamical diagnosis addressing the relations between the mean flow velocity, static pressure, turbulent kinetic energy production and viscous dissipation rates along the skimming flow domain. Additional runs with wall roughness, riser height (h) and tread length (l) variations were performed to conclude about the effects in the mentioned hydrodynamical variables.

keywords: flat slope stepped spillways, skimming flow, aerated flow, non-aerated flow, turbulence modeling, multiphase flow modeling, $SST\ k-\omega$ model, mixture model, viscous sub-layer, log-law region.

Estudio del Flujo Rasante en Canales Escalonados de Baja Pendiente

Resumen: En esta tesis se presentan y analizan los resultados de un estudio de modelación numérica que aborda las propiedades del flujo rasante en canales escalonados de baja pendiente. Los datos experimentales de los perfiles de velocidad del flujo medio del modelo físico de Hunt y Kadavy [5, 42], se usaron para la calibración de los resultados obtenidos con un modelo numérico realizado con la herramienta comercial CFD: Ansys Fluent. $SST\ k-\omega$ fue seleccionado para el modelado de la turbulencia y el modelo "Mixture" para el proceso de rastreo de la superficie libre, pero como la aireación de flujo aguas abajo del punto de incepción no fue capturada por los modelos mencionados, se realizó un "procedimiento de ajuste de datos" para poder comparar la información experimental de las estaciones de medición con entrada de aire, con los resultados numéricos. Este trabajo presenta un diagnóstico hidrodinámico que aborda las relaciones entre la velocidad, la presión estática y las tasas de producción y disipación viscosa de la energía cinética turbulenta del flujo medio, en todo el dominio del flujo rasante. Se llevaron a cabo corridas adicionales con variaciones en la rugosidad de la pared, la altura de la contrahuella (h) y la longitud de la huella (l) para concluir acerca de los efectos en las variables hidrodinámicas mencionadas.

Palabras clave: Descargas escalonadas de baja pendiente, flujo rasante, flujo aireado, flujo no aireado, modelado de la turbulencia, modelado del flujo multifásico, modelo $SST\ k-\omega$, modelo "Mixture", sub-capa viscosa, capa logarítmica.

1 Problem statement

Stepped structures are used for the discharge of water from dams or for conduction of flow in natural streams. Due to the innovations in materials and constructive processes, as well as in the design parameters and implementation of numerical models with advances in Computational Fluid Dynamics (CFD), the interest in research on flow over stepped channels has increased considerably in recent decades [1, 2]. A stepped spillway is an open channel configured at its bottom by a series of falls or steps, and skimming flow is characterized because water flows as a coherent stream over the bottom and fully occupies the cavities between the risers and the treads, and the steps act as a macro-roughness that decreases the flow velocity; in addition, the generated turbulence contributes to the raise of the boundary layer and the subsequent entry of air into the stream, distinguishing between two regions: aerated and non-aerated [3].

The results of investigations in stepped structures using physical models have proved to be useful only for the study case from which they have been obtained and have only been used as a guide for similar cases. One of the problems for the design of this type of structures is the lack of knowledge on the quantitative representation of the complex flow in each step [1, 3] like the characteristics of the recirculation vortices in the steps cavities; the energy dissipation generated by these vortices, the air entrainment and the friction with the channel material; the pressure and the velocity field, as well as the flow height, mainly in the area upstream of air entry or inception point.

In addition, the physical models of biphasic water - air flows require the similarity in Froude (Fr), Weber (Re) and Reynolds (Re) numbers to be simultaneously fulfilled, in order to avoid that parameters such as the bubbles size and turbulent scales, are affected by scale effects. This is impossible unless one works on the same scale as the prototype [4], which is economically and technically unviable in most engineering projects. Consequently, the distortions happening in modeling occur because reduced scale physical models fail to scale viscous forces and surface tension effects [5].

In order to reduce the scale effects associated with air entrance to the flow over a stepped chute, it is recommended to work with $10:1$ scale models or larger [6], with a Reynolds number of 10^5 and a Weber number of at least 100 [7]; however, recent research has shown that scale effects can even affect laboratory models with $2:1$ to $3:1$ scales [4].

The pressure distribution in skimming flow along the step faces has been widely studied for steeply sloping stepped spillways, finding negative pressures in the upstream half of the treads and the maximum values in the upper corners of the risers [8–10]. The reason of focussing the investigation efforts in the larger slopes chutes is because these are more prone to cavitation due to the large negative pressure magnitudes, mainly in the non aerated region [9] where the lack of the cushioning effect of the entrained air increases the cavitation potential [3]. Then, it is important to verify if the pressure distributions found for high slopes are also valid for flatter slopes, and determine the design modifications that can be applied to reduce pressure magnitudes in case that these put in danger the channel structural integrity.

An important task for skimming flow researchers has been to propose general expressions to quantify the energy dissipation along a stepped chute. The majority of the proposed equations are valid only for cases where a condition of completely developed aerated flow is reached [2]. In flat slope stepped channels the energy dissipation is due to the the combined effect of the recirculating vortices and

the flow friction with the bottom solid boundary [11]. There is today a lack of knowledge with respect to the quantification of the dissipated energy in the non-aerated region of flat slope stepped channels, and the fractions of that energy that are dissipated due to the shear stress transfer between the main stream and the recirculating zones, and the friction with channel material.

In the context of the scale issues in the stepped spillways physical models, it is important to look for complementary alternatives. With the increase in the performance of computers and the aforementioned advances in CFD models, numerical modeling emerges as an important alternative in the research and design of stepped channels. It is therefore necessary to answer the question of whether with appropriate equations and coefficients, suitable numerical methods and turbulence and multiphase flow models that involve a lower investment in computational capacity capturing the complexity of the phenomenon, and an optimal mesh size that produces good results with a smaller discretization error, numerical modeling may or may not correctly quantify skimming flow properties in flat slope stepped structures. Properties such as the pressure distribution along the step phases, and the dissipated energy due to the recirculating vortices and the friction with the bottom, mainly in the non-aerated region. This implies a validation of the results with experimental measurements of the flow characteristics.

2 Justification

In hydraulics of natural channels it is important to identify the minimum flow velocity and tractive efforts with the capacity to initiate the motion of soil particles that compose the channel bed and banks. In the last century experiments have been made with variable particle diameters between fine sands and coarse gravels, concluding that speeds between 0.457 and $1.520 m/s$, and tractive forces between 1.29 and $43.6 Pa$ respectively, are the maximum permissible limits before the beginning of the erosion and scour phenomena [12]. In high slope natural currents channels (greater than 3 to 5%) these maximum limits are overcome with slack; and in urban centers with population settlements close to the banks of rivers and streams, it is necessary to control the river dynamics caused by the washing of soil particles that can result in stability problems, migration of curves, among other phenomena that trigger human and economic losses. Consequently, alternative engineering solutions arise for the protection of beds and banks and the dissipation of flow energy.

Smooth spillways are open channels with a smooth-aligned bottom that require special dissipation structures in the delivery to the natural channel. Depending on the Froude number (Fr) expected at the channel exit, the dissipation structures can vary from a simple concrete apron with low longitudinal slope that induce the formation of a hydraulic jump, to concrete blocks or baffle piers, dentated end-sills and ski jumps. When more than one dissipation structure is required, substantial increases in costs are generated, an alternative is the implementation of steps at the channel bottom [3]. Stepped structures guarantee a continuous energy dissipation along the whole channel, and not in a punctual way as it happens with the special structures at the toe.

Skimming flow in stepped structures is characterized by the formation of recirculating vortices in the cavities between tread and riser; which are one of the main responsible for energy dissipation. Depending on the channel slope, described as the ratio between the riser (h) and tread (l) lengths, this vortex may or may not occupy the entire cavity. In flat slope stepped channels ($0.21 < h/l < 0.27$), the impact of the vortex occurs upstream the edge of the next step, so the energy dissipation is due to the combined action of the vortices on the upstream portion of the tread, and the roughness of the channel material downstream the vortices [11]. It is then important to conduce a study about the fraction of the total energy dissipation that takes place at each of these two regions, and quantify its increase due to a rise in the roughness of the material downstream the vortex impact by means of stuck stone, hollows, baffle walls, among others. Details about the longitude of the recirculation zone and how it varies with the stepped channel slope and riser and tread lengths are important for the channel designers to install the roughness elements only in the skin friction zone, preventing these elements height to interfere with the vortices formation.

A study about the pressure distribution along the step faces should also be carry out to verify that the positive and negative values found by other authors in steeply sloping spillways and their location, are also valid for the slope range: $0.21 < h/l < 0.27$. Depending on the location and magnitude of the maximum pressure values (negative or positive), the designer can decide about whether or not it is necessary to reinforce certain zones of the channel, depending on its material and structural vulnerability to the forces generated by the pressure distribution. All of the above explains the need to quantify skimming flow properties through numerical modeling, in order to be able to propose an adequate design of this type of channels.

3 Objectives

3.1 General objective

To estimate qualitatively and quantitatively by means of numerical modeling the skimming flow properties in flat slope stepped channels.

3.2 Specific objectives

- To identify the potentialities and weaknesses of the turbulence and multiphase flow models available in literature, for numerical modeling of skimming flow in flat slope stepped channels.
- To evaluate the suitability of applying numerical models with potentialities, for the representation of data measured in physical models or prototypes.
- To investigate, through the use of the validated numerical model as a tool, the relationships between the variables of skimming flow in flat slope stepped channels.

4 Theoretical framework

4.1 Applications and uses of stepped spillways

The main application of stepped channels is the flow energy dissipation in water discharges. The above is mainly useful in dams, where stepped chutes are designed to evacuate the maximum probable flow as a result of the dam structure overflow [13], and in high slope streams, in which the flow has a high erosive potential, making necessary the protection of the bed and the banks together with a continuous dissipation granted by the successive falls generated by the steps.

The applications reach fields as diverse as the water quality in rivers and streams by flow aeration, as well as the improvement of the water - air transfer of atmospheric gases in the water treatment plants. Check dams are transverse structures built in mountain creeks with high sediment transport capacity and act as sediment traps for the protection of settlements or populations downstream; and in turn decrease the bed slope between adjacent dams and dissipate the flow energy in the successive falls formed by each dam. Finally, among the most modern uses are the stepped ditches for roads, sewer systems with stepped sinks, and fish ladders that allow its transport from the dam to the river that has been modified by the construction of the dam [2].

4.2 Flow regimes

The flow in stepped channels is divided into three types according to the regime: nappe flow, transition flow and skimming flow. The nappe flow is characterized by a series of successive drops of free falling jets, with an air gap between the jet and the step riser. In Skimming flow, the flow passes as a single coherent stream over a pseudo-bottom formed by the straight imaginary line joining all the steps outer edges that act as a macro-roughness. The air chamber disappears as the flow never separates from the stepped structure [11]. The transition flow is an intermediate case between the two previous ones in which the air chamber appears in some steps and disappears in others, and in the cavities between steps a recirculation flow is formed. Free surface is characterized by being chaotic and presenting splash areas [14].

A detailed description of the three flow regimes is given below.

4.2.1 Nappe flow

The series of successive drops characteristic of nappe flow are responsible for the energy dissipation, which is achieved in three specific stages [2]:

- The jet break-up into air.
- The jet impact on the downstream step tread.
- The mixing on the downstream step tread, and the formation of a partially or fully developed hydraulic jump.

This type of flow is given for small discharges, and flat slopes. Depending on the formation of the hydraulic jump, nappe flow is divided into three [2]:

- Flow with fully developed hydraulic jump, which is supercritical in the jet impact adjacent zone, until the flow becomes subcritical due to the hydraulic jump, and later critical in the step edge before the next fall.
- Flow with partially developed hydraulic jump, in which discharge is greater, or the step tread is not long enough. The hydraulic jump development interferes with the next step edge.
- Flow without hydraulic bump, which occurs for greater discharges or very short steps. In this case flow is always supercritical, and the formation of waves on the surface has been reported.

4.2.2 Transition flow

Transition flow is given for intermediate discharges, which don't adopt all the characteristics of nappe flow, nor all of skimming flow. Initially air entrance doesn't occur, and air chambers don't appear in any of the cavities. Surface profile is wavy and continues to accelerate downstream until the first free-falling water jet appears. It is from this point towards downstream that aerated flow takes place, characterized by air chambers of different size and shape in each of the steps cavities, and considerable water splashes and droplet ejections. Flow reaches high speeds in cavities without air chambers or with very small ones, and energy dissipates in the steps with the presence of free-falling jets. Downstream the inception point, the air-water mixture flows parallel to the channel pseudo-bottom, despite the presence of air chambers. In general terms, flow is chaotic and droplet ejections reach heights of up to 3 to 8 times the riser height [14].

4.2.3 Skimming flow

Skimming flow occurs for large discharges or steep slopes and water flows as a coherent stream over the pseudo-bottom, under which recirculating vortices form and get sustained by the shear stresses transfer from the water current flowing in the upper part. It is possible to distinguish three flow patterns: non-aerated flow, gradually varying aerated flow and uniform aerated flow, as shown in Figure 1.

Initially, downstream the first step in the non-aerated region, water surface has a smooth appearance. At the channel bottom, steps generate turbulence and boundary layer grows until it reaches the free surface, in the so-called inception point. From there the turbulence is strong enough to generate air entrance. Downstream, the flow composed of air and water behaves as gradually varied until it reaches uniform flow conditions if the channel is long enough [2, 11].

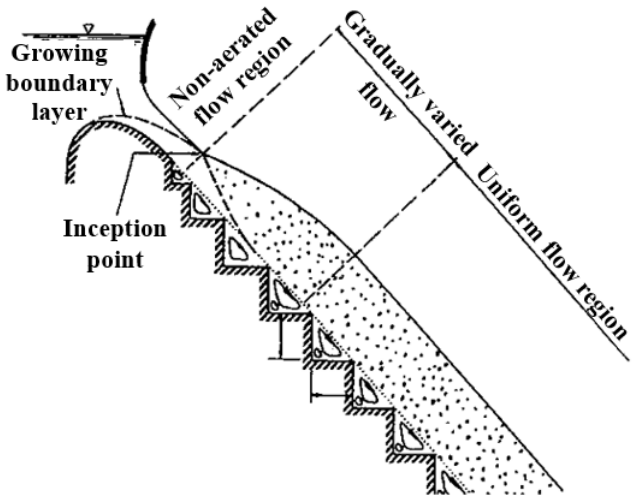

Figure 1: Skimming flow in stepped channels. Taken from [11]

Depending on the channel slope, three skimming flow sub-regimes are distinguished. For flat slopes ($h/l < 0.27$), flow pattern is called SK1 sub-regime or wake step interference, in which the outer limit of the recirculation vortex impacts the tread intermediate zone; therefore energy dissipation is given by the effect of recirculation and subsequent friction with the channel bottom material. For intermediate slopes ($0.27 < h/l < 0.47$), flow sub-regime SK2 or wake-wake interference is given, for which the recirculation zone of one step interferes with that of the adjacent downstream step, and in energy dissipation process the participation of friction with the channel bottom dissappears. On steep slopes ($h/l > 0.47$) SK3 or recirculating cavity sub-regime occurs, characterized by large two-dimensional recirculation vortices between the outer edges of the steps, responsible of the energy dissipation [2, 11].

4.3 Flow regimes limits

Several authors have been concerned about defining the nappe and skimming flow limits. If y_c is the flow critical depth, there are in the literature various expressions for the maximum value of the relation with the riser height $(y_c/h)_{upper}$ to guarantee the nappe flow regime, and for the minimum value $(y_c/h)_{onset}$ to guarantee the skimming flow regime; however equations for these limits became valid as the existence of a transition flow was considered. Llano [2] performed a correlation analysis between the existing mathematical relationships to determine the limits, and the experimental data available up to that time. His results proved that the most appropriate expressions for the nappe flow upper limit as a function of the relation between de riser height and the tread length h/l, are those proposed by Yasuda and Ohtsu [15] and Chanson [16] respectively:

$$\left(\frac{y_c}{h}\right)_{upper} = \frac{\left(1.4 - \frac{h}{l}\right)^{0.26}}{1.4} \tag{4.1}$$

$$\left(\frac{y_c}{h}\right)_{upper} = 0.89 - 0.4\left(\frac{h}{l}\right) \tag{4.2}$$

As well, the expressions proposed by Yasuda and Ohtsu [15] and Chanson [16] respectively for the skimming flow lower limit, are those that have a better correlation with the experimental data:

$$\left(\frac{y_c}{h}\right)_{onset} = 0.862\left(\frac{h}{l}\right)^{-0.62} \tag{4.3}$$

$$\left(\frac{y_c}{h}\right)_{onset} = 1.2 - 0.325\left(\frac{h}{l}\right) \tag{4.4}$$

By a trend-regression procedure of equations (4.1) and (4.2); and (4.3) and (4.4) respectively, Llano [2] proposes the following expressions for the nappe flow upper limit,

$$\left(\frac{y_c}{h}\right)_{upper} = -0.372\frac{h}{l} + 0.886 \tag{4.5}$$

and for the skimming flow lower limit,

$$\left(\frac{y_c}{h}\right)_{onset} = 1.176e^{(-0.304h/l)} \tag{4.6}$$

which are valid for the slope range $0.20 < h/l < 1.43$. For very flat slopes in the range $0.06 < h/l < 0.20$, Llano [2] proposes the next expressions for the nappe flow upper limit,

$$\left(\frac{y_c}{h}\right)_{upper} = 11.01\left(\frac{h}{l}\right)^2 - 4.398\frac{h}{l} + 1.249 \tag{4.7}$$

and for the skimming flow lower limit,

$$\left(\frac{y_c}{h}\right)_{onset} = 17.476\left(\frac{h}{l}\right)^2 - 7.247\frac{h}{l} + 1.846 \tag{4.8}$$

4.4 Skimming flow numerical modeling

For skimming flow numerical modeling, the differential form of the mass conservation (continuity) and linear momentum equations for incompressible mean flow, is used. These are represented by equations (4.9) and (4.10) respectively:

$$\frac{\partial U_i}{\partial x_i} = 0 \tag{4.9}$$

$$\rho\frac{\partial U_i}{\partial t} + \rho U_j\frac{\partial U_i}{\partial x_j} = -\frac{\partial P}{\partial x_i} + \rho g_i + \frac{\partial\left(T_{ij} - \rho\overline{u_i u_j}\right)}{\partial x_j} \tag{4.10}$$

where:
U_i is the mean flow velocity vector, in which $i = 1, 2$ or 3 stands for the three directions in space
x_i is the spatial direction x_1, x_2 or x_3
t is the time variable
P is the mean flow pressure
g_i is the gravitational acceleration vector
T_{ij} is the mean flow deviatoric stress tensor
u_i is the flow velocity vector for fluctuations
$-\rho\overline{u_i u_j}$ is the Reynolds stress tensor

A suitable discretization method must be chosen to be able to approximate the partial differential equations (4.9) and (4.10) by a system of algebraic equations as a function of the unknown variables at a set of discrete locations in space and time [17].

4.4.1 Discretization methods

There are several approaches, but the most common ones are: finite difference (FD), finite volume (FV) and finite element (FE) methods [17].

In the FD method, the starting point are the equations to be solved in differential form. The domain is discretized by points, which together make up the grid. At each point, partial derivatives of the differential equations are approximated through Taylor series expansions in terms of the nodal values of the unknowns. Resulting algebraic equations per grid node are function of the variables at that node and its neighbours. The main advantage of this method is its easy implementation; however its restricted to simple grids and non complex geometries, and it doesn't conserve mass, energy and momentum in low resolution grids [17].

In the FV method, the solution domain is discretized into control volumes (CV), in which the nodes are the cell centroids. The starting point are the differential equations to be solved, integrated in each CV. Trough the Gauss divergence theorem, each term is expressed as a surface integral. Interpolation is used to express variable values at the CV surfaces in terms of the nodal values. In consequence an algebraic equation per CV is obtained. The main differences with FD method, lie in that FV method is conservative for mass, momentum and energy, no matter grid resolution, and that is applicable for complex geometries because it can accommodate any type of grid [17].

Finally, FE method is similar to FV method, because the domain is also divided into a set of discrete volumes; but the equations to be solved are multiplied by a weight function, before they are integrated. The idea is to minimize the difference between the exact solution and the approximation function within each element. The latter is accomplished globally, so local conservation is not always satisfied [17].

4.4.2 Pressure velocity coupling

Several problems arise when solving the discretized algebraic mass and momentum conservation equations. First, the advective terms in the momentum equations have no lineal terms and, second, the pressure term appears in all the momentum equations but it doesn't have its own transport equation, so it's a coupled system [18].

Given a pressure field, discretized momentum equations are solved for each control volume, so that velocity fields are obtained. If the pressure field is correct, calculated velocities should satisfy continuity equation. Below, the pressure-velocity coupling algorithms used or mentioned in this thesis are described [18].

SIMPLE (Semi-Implicit Method for Pressure-Linked Equations) is a segregated algorithm in which an initial pressure guess $p*$ is made in each node, to be able to obtain initial approximations of the velocity fields with the momentum equations. The discretized continuity equation is used to derive an expression for pressure correction p'. Finally, corrected pressure field ($p* + p'$) is used to correct velocity fields. Corrected results replace the initial guess, and the above procedure is repeated until convergence is achieved [18]. Besides SIMPLE, there are other segregated algorithms such as SIMPLER (SIMPLE Revised), SIMPLEC (SIMPLE Consistent) and PISO (Pressure Implicit with Splitting of Operators).

Furthermore, a modification to the solution procedure of segregated algorithms have been proposed in the COUPLED method. With this one, a robust and efficient single phase implementation for steady-state flows is obtained, with a better performance than segregated methods. This kind of algorithm should be implemented in transient flows when poor quality mesh and/or large time steps are used. The main difference with the previous methods is that COUPLED solves the momentum and pressure correction equations together [19].

4.4.3 Interpolation schemes

In the FD method, to be able to express first and second derivatives as functions of nodal values; and in the FV method, to be able to express unknown variables and derivatives in CV faces as functions of nodal values; interpolation schemes become necessary. The interpolation schemes used in this thesis are:

- *Least Squares Cell-Based Gradient Evaluation*: With this interpolation scheme the gradient of an arbitrary scalar ϕ in a node, is assumed to be linear with respect to its neighbours. Thus, the change in ϕ between any node c_0 and any of its neighbours c_i, along the distance vector r_i from c_0 to c_i, can be expressed as [19]:

$$(\nabla\phi)_{c_0} \cdot r_i = (\phi_{c_i} - \phi_{c_0}) \tag{4.11}$$

  where:
  $(\nabla\phi)_{c_0}$ is the gradient of a scalar ϕ in the central node c_0.
  ϕ_{c_i} is the scalar ϕ value in a neighbour node.
  i is an indicator of the neighbour node.
  ϕ_{c_0} is the scalar ϕ value in the central node.

  Equation (4.11) represents an expression for each of the neighbour nodes. This linear system is solved in a least-squares sense, by decomposing the coefficient matrix using the Gram-Schmidt process. This scheme is less expensive to compute than others [19].

- *PRESTO! - PREssure STaggering Option*: If a high variable pressure field is present in the analysis domain, as it happens in skimming flow, storing pressure and velocity in the same nodes can wrongly smooth the pressure field [18]. This interpolation scheme uses a "staggered" control volume with a centroid located in the face of the original control volume, to calculate the face pressure, and thus, correctly capture the high pressure field variability. In consequence, this scheme is recommended in high-speed rotating flows and strongly curved domains [19].

- *QUICK - Quadratic Upwind Interpolation for Convective Kinetics*: It's a third order interpolation scheme, which assumes a parable between two points upstream and one point downstream, or vice versa depending on flow direction. If one wishes to calculate the ϕ value in the eastern face of the control volume ϕ_e; a parabolic variation of the scalar is assumed between the centroidal node P, and the western and eastern nodes, W and E respectively [17]. In a uniform grid for example, expression (4.12) is used:

$$\phi_e = \frac{6}{8}\phi_P + \frac{3}{8}\phi_E - \frac{1}{8}\phi_W \tag{4.12}$$

4.4.4 Turbulence models

The Reynolds Stress tensor term, $-\rho\overline{u_i u_j}$, in equation (4.10), adds six extra unknowns. To be able to get a solution for the equations system, transport equations have been deduced for the Reynolds stresses; however, each new transport equation adds new unknowns to the system. Therefore, as experimentally it's been observed that turbulence decays unless there are shear stresses, and that it grows proportionally to the mean rate-of-strain; the Boussinesq assumption is proposed [18] as shown in (4.13):

$$-\rho\overline{u_i u_j} = 2\mu_t S_{ij} - \frac{2}{3}\rho k \delta_{ij} \tag{4.13}$$

where:
μ_t is the turbulent eddy viscosity. It's modelled as a function of the turbulent velocity u and length l scales of large eddies.
S_{ij} is the mean rate-of-strain tensor.
k is the turbulent kinetic energy.
δ_{ij} is the Kronecker delta.

Two equation models use the square root of the turbulent kinetic energy to estimate the turbulent velocity scale; so that a transport equation for k is necessary. For the length scale, various solutions are proposed depending on the turbulence model [20]:

- $k - Epsilon(\epsilon)$ *model*: This model estimates the turbulent length scale as a function of the viscous dissipation rate ϵ. Therefore, besides equations (4.9) and (4.10), transport equations for k and ϵ are required. Equations and closure coefficients for this model are summarized in equations (4.14) to (4.18) [20].

  Eddy vistosity:

$$\mu_t = \rho C_\mu k^2/\epsilon \tag{4.14}$$

  Turbulence kinetic energy:

$$\rho\frac{\partial k}{\partial t} + \rho U_j \frac{\partial k}{\partial x_j} = -\rho\overline{u_i u_j}\frac{\partial U_i}{\partial x_j} - \rho\epsilon + \frac{\partial}{\partial x_j}\left[(\mu + \mu_t/\sigma_k)\frac{\partial k}{\partial x_j}\right] \tag{4.15}$$

  Dissipation rate:

$$\rho\frac{\partial \epsilon}{\partial t} + \rho U_j \frac{\partial \epsilon}{\partial x_j} = C_{\epsilon 1}\frac{\epsilon}{k}\left(-\rho\overline{u_i u_j}\right)\frac{\partial U_i}{\partial x_j} - C_{\epsilon 2}\rho\frac{\epsilon^2}{k} + \frac{\partial}{\partial x_j}\left[(\mu + \mu_t/\sigma_\epsilon)\frac{\partial \epsilon}{\partial x_j}\right] \tag{4.16}$$

  Closure coefficients:

$$C_{\epsilon 1} = 1.44 \qquad C_{\epsilon 2} = 1.92 \qquad C_\mu = 0.09 \qquad \sigma_k = 1.0 \qquad \sigma_\epsilon = 1.3 \tag{4.17}$$

  Auxiliary relations:

$$l = C_u k^{3/2}/\epsilon \tag{4.18}$$

  where:
  $C_{\epsilon 1}$, $C_{\epsilon 2}$ and C_μ are closure coefficients obtained from experimental information; and σ_k and σ_ϵ are the Prandtl/Schmidt turbulent numbers for k and ϵ respectively.

  μ is the fluid dynamic viscosity.

- $k - Omega(\omega)$ *model*: This model estimates the turbulent length scale as a function of the dissipation per unit of turbulent kinetic energy ω, or especific dissipation rate. Therefore, transport equations for k and ω are required. Equations and closure coefficients for this model are summarized in equations (4.19) to (4.23) [20].

  Eddy vistosity:

$$\mu_t = \rho k/\omega \tag{4.19}$$

  Turbulence kinetic energy:

$$\rho\frac{\partial k}{\partial t} + \rho U_j\frac{\partial k}{\partial x_j} = -\rho\overline{u_i u_j}\frac{\partial U_i}{\partial x_j} - \beta^*\rho k\omega + \frac{\partial}{\partial x_j}\left[(\mu + \mu_t\sigma^*)\frac{\partial k}{\partial x_j}\right] \tag{4.20}$$

  Specific dissipation rate:

$$\rho\frac{\partial \omega}{\partial t} + \rho U_j\frac{\partial \omega}{\partial x_j} = \alpha\frac{\omega}{k}(-\rho\overline{u_i u_j})\frac{\partial U_i}{\partial x_j} - \beta\rho\omega^2 + \frac{\partial}{\partial x_j}\left[(\mu + \mu_t\sigma)\frac{\partial \omega}{\partial x_j}\right] \tag{4.21}$$

  Closure coefficients:

$$\alpha = 5/9 \qquad \beta = 3/40 \qquad \beta^* = 9/100 \qquad \sigma = 1/2 \qquad \sigma^* = 1/2 \tag{4.22}$$

  Auxiliary relations:

$$\epsilon = \beta^*\omega k \qquad l = k^{1/2}/\omega \tag{4.23}$$

  where:
  α, β and β^* are closure coefficients obtained experimentally; and σ and σ^* are the Prandtl/Schmidt turbulent numbers for k and ω respectively.

  In both of the above two-equation models, $-\rho\overline{u_i u_j}\partial U_i/\partial x_j$ is defined as the turbulent kinetic energy production term G_k. To evaluate it in a manner consistent with the Boussinesq approximation; relation (4.24) is proposed in [19]:

$$-\rho\overline{u_i u_j}\frac{\partial U_i}{\partial x_j} = G_k = \mu_t S^2 \tag{4.24}$$

  where:
  S is the modulus of the mean rate-of-strain tensor; $S = \sqrt{2S_{ij}S_{ij}}$.

- *Shear Stress Transport (SST)* $k - Omega(\omega)$ *model*: In this model, the $k - \epsilon$ formulation is transformed as a function of ω, and a blending function that takes values of approximately one close to the wall and zero far away from it; is used to activate $k - \omega$ model close to the solid boundaries, and the transform $k - \epsilon$ model in the freestream region [19].

As the previously cited two equation models are based on expressions (4.9) and (4.10), deduced from the decomposition of the instantaneous flow variables in the mean flow and the fluctuating flow variables through the Reynolds decomposition technique, these kind of turbulence models are called RANS, which stands for Reynolds Averaged Navier Stokes equations models, and none of the turbulent scales are directly solved [20]. On the other hand, Large Eddy Simulation-LES models directly solve the largest eddies scales [19].

- *Large Eddy Simulation - LES models*: LES models are an intermediate solution between RANS and Direct Numerical Simulation - DNS, because they solve the largest eddies scales, and model the smallest ones. The logic in which these kind of models are based can be resumed into two general ideas: First, momentum, mass and energy are mostly transported by the largest structures, which are more dependent of geometry and boundary conditions; and second, smallest eddies, responsible of turbulent kinetic energy dissipation, are less dependent of geometry, tend to be more isotropic, and in consequence there are more chances to find a universal turbulence model, that can represent the influence of smallest scales in the directly solved ones [19].

4.4.5 Multiphase flow models

To correctly model skimming flow, a multiphase air-water model should be implemented to take into account two phenomena: the flow free surface, or air-water inter-phase; and the air entrainment to the flow downstream the inception point. Volume of Fluids-VOF model and Mixture model are briefly explained in what follows as both of them are used in this thesis.

- *VOF model*: To simulate multiphase flow, this model uses a unique set of conservation equations for the total flow domain. The set must consider the differences in the properties of multiple fluids involved, as well as surface tension in the interfaces. Mass conservation equation in expression (4.9) doesn't change. Flow movement is governed by the Navier Stokes Equations for an incompressible fluid presented in expression (4.10), with an extra term to account for surface tension in air-water interface [21]. Let's call this term A:

$$A = \int \sigma \kappa' n' \delta^{\beta}(x - x') \, \mathrm{d}s' \tag{4.25}$$

where:
σ is the surface tension coefficient.
κ' is the free surface curvature in 2D domains, and twice the mean value of the curvatures in 3D domains.
n' is the unit vector normal to the free surface. δ^{β} is the Dirac delta function, where $\beta = 2$ stands for 2D domains and $\beta = 3$ for 3D domains.
x is the coordinate of the point where the equation is evaluated and x' is a point in the free surface, such that only if $x = x'$ then δ function isn't zero, guaranteeing that A term is only evaluated in the fluids interface.
$\mathrm{d}s'$ is the free surface differential area.

In equations (4.9) and (4.10) ρ is replaced by the air-water mixture density ρ_m [21]:

$$\rho_m = \alpha \rho_w + (1 - \alpha) \rho_a \tag{4.26}$$

where:
α is the water volumetric fraction, defined as the ratio of the water volume to the total mixture volume.
ρ_w is the water density.
ρ_a is the air density.

Finally, an extra transport equation, for water volumetric fraction α is necessary [21] (see expression (4.27)).

$$\frac{\partial \alpha}{\partial t} + \frac{\partial}{\partial x_i}(\alpha U_i) = 0 \tag{4.27}$$

- *Mixture model*: This model is useful when there is a suspension of a dispersed phase - secondary phase (air bubbles downstream the inception point for skimming flow), in a continuous fluid - primary phase (water flowing over the pseudo-bottom), which follows closely the fluid motion [22]. Equations used are the mass conservation and momentum equations for the air-water mixture, and the continuity equation for the dispersed phase. As the momentum equation for the dispersed phase is not taken into account, relative or slip velocity, which is defined as the velocity of the secondary phase p, relative to the velocity of the primary phase q (see equation (4.28)), is considered with a closure algebraic formulation [19, 22].

$$\vec{v}_{pq} = \vec{v}_p - \vec{v}_q \tag{4.28}$$

where:
$\vec{v}_{pq}$ is the relative or slip velocity.

In this thesis, Manninen *et al.* [23] formulation for the algebrahic slip velocity closure expression is used:

$$\vec{v}_{pq} = \frac{\tau_p}{f_{drag}} \frac{(\rho_p - \rho_m)}{\rho_p} \vec{a} \tag{4.29}$$

where:

$$\tau_p = \frac{\rho_p d_p^2}{18 \mu_q} \tag{4.30}$$

is the particle (air bubble of the dispersed phase) relaxation time.
f_{drag} is the drag function.
ρ_p and ρ_m are the dispersed phase and mixture densities respectively.
$\vec{a}$ is the secondary phase particle's acceleration.
d_p is the secondary phase particle's diameter.
μ_q is the primary phase dynamic viscosity.

In this research, the drag function f_{drag} is calculated with Schiller and Naumann [24] expression:

$$f_{drag} = \begin{cases} 1 + 0.15\mathrm{Re}^{0.687} & \mathrm{Re} \leq 1000 \\ 0.0183\mathrm{Re} & \mathrm{Re} > 1000 \end{cases} \tag{4.31}$$

where:
Re is the relative Reynolds number:

$$\mathrm{Re} = \frac{\rho_q |\vec{v}_p - \vec{v}_q| d_p}{\mu_q} \tag{4.32}$$

5 State of the art

The advances in the Roller-Compacted Concrete (RCC) construction method for gravity dams combined with its economical advantages, generated an increment in the research of skimming flow over the stepped spillways during the 1980's [3,25]. At the time, physical models were performed to provide the adequate stepped geometry during the design stages of the dam construction projects, but no general application design techniques were available for engineers [3]. Young [26] conducted a model study to determine the feasibility of the stepped chute for the Upper Stillwater Dam, finding an energy reduction 75% greater than with a smooth spillway of the same height. Sorensen [27] carried out a stepped spillway model to investigate about the steps design and spacing to optimize the energy dissipation and achieve a smooth transition of the flow, from the spillway crest to the stepped face.

Later on, the attention of the investigations focused on proposing expressions for the prediction of the dissipated energy as a function of the the skimming flow properties and the channel geometry, but only for cases where uniform flow is reached along the channel. Stephenson [28] found that the energy loss is proportional to the dam height and not only a function of the step configuration. Christodolou [29] proved that the highest dissipation correspond to the small values of the ratio of the critical depth of flow passing over the spillway to the step height y_c/h, and decreases with increasing y_c/h. Chanson [30] proposed an equation to calculate the energy dissipation function of the Darcy friction factor f, with the experimental data indicating skimming flow situations with friction factors between 0.5 and 4, with a mean value of 1.3.

The appropriate calculation of the friction factor is a key element in the prediction of energy dissipation in skimming flow downstream the inception point, because the presence of air bubbles does not affect the velocity distribution, but reduces the shear stress between the flow layers [31]. Chanson [31] analysed prototype and model data and proposed and expression to estimate de reduction in the flow resistance due to the self-aeration, by calculating the relation between the aerated and the non-aerated friction factor f_e/f, that decreases as the air concentration increases. Hartung and Scheuerlein [32] studied open channel flows on rockfilled channels with an extremely rough bottom that induced a highly turbulent flow with air entrainment, and with the experimental results proposed a similar expression to the one of Chanson, for the relation f_e/f. Chanson and Toombes [33] proposed that drag reduction results from interactions between the entrained air bubbles and the developing mixing layer, and that small air bubbles tend to resist stretching leading to vortex inhibition.

Several researchers have turned their attention in the last two decades to analyse the magnitude of the forces and the pressure distributions on the steps. Sánchez-Juny, Bladé and Dolz [8] measured the pressure field on the bottom of a stepped spillway in the aerated flow region, and proposed equations to calculate the magnitude and the location of negative pressures along the step faces. On the treads, negative pressures were observed at the upstream half for values of $y_c/h > 1.3$, and at the risers, positive pressures were only observed close to the downstream adjacent horizontal face. Amador, Sánchez-Juny and Dolz [9] conducted physical model investigations in stepped chutes to characterize the non-aerated flow region which is potentially prone to cavitation damage, mainly at the vertical step face closer to the inception point, and through the analysis of the pressure variations at that region, a maximum flow velocity of $15m/s$ was proposed to protect steeply sloping spillways from high negative pressures. Daneshfaraz *et al.* [10] carried out several numerical modelations for various step configurations and concluded that pressure distribution behaviour was the same for

all the cases, with the maximum negative value at the step outer edges. However, in spite of the physical and numerical model results and that significant flood releases have already occurred in some large dams, like the Shuidong and Dachaoshan RCC dams in China and the Dona Francisca dam in Brazil, cavitation damage has not been reported, and in consequence there are no precise conclusions about the maximum unit discharge for which a stepped spillway can be designed to guarantee a given operational life [25].

With respect to the inception point and the region downstream where uniform flow conditions are reached, several authors have studied whether or not that regions are achieved along the chute depending on the flow and channel properties. With statistical analysis of a large number of experimental data obtained in laboratory models and prototypes, Chanson [34] proposed two equations to calculate the distance to the inception point measured from the crest L_{in} and the flow depth at that point d_{in}, valid for steep stepped channels. Chanson suggested that the unit discharge q predominantly governs the value of L_{in} while the step height h has a small influence, and that for higher channel slopes the aeration takes place closer to the spillway crest. Boes and Minor [35] suggested that the vertical distance normalized with respect to y_c, required for uniform flow to be attained increases approximately linear with the relation h/l and proposed an equation to estimate it. Although on moderate to steep slopes it is widely accepted that the air entrainment corresponds to the intersection of the outer edge of the developing boundary layer with the free-surface; it is untrue for very flat slopes: $\alpha < 5$ to $10°$ [36]. Physical observations from Chanson [36] and from Chanson and Toombes [37] proved that in very flat slope channels, air entrainment occurs far upstream of the intersection of the boundary layer outer edge with the free-surface, and is believed to be associated with the interactions of the latter with vortical structures [38].

Regarding the clear water area upstream the inception point, the authors have focused their efforts in determining its length along the spillway, the turbulent boundary layer growth and the rate of energy dissipation, defined as the ratio of the dissipated energy at a point to the maximum head available at the spillway crest. Pfister, Hager and Minor [39] and Zamora *et al.* [40] stated that as the unit flow rate become higher, the length of the non-aerated flow region too, so the absence of air close to to the step's faces can induce to cavitation, such that aerators at the first riser can be installed to add air to the chute bottom. Matos and Meireles [25] established that the measured turbulence intensities upstream the inception point near the pseudo-bottom are much higher than the ones for smooth channels, so a larger boundary layer growth rate takes place. In Chanson [34], the boundary layer growth rate for stepped chutes is 2.8 times larger than for smooth channels. Matos and Meireles [41] reported that the velocity distribution is well described by a power law in the non-aerated region and with regard to the rate of energy dissipation, values lower than 0.3, similar to those of Hunt and Kadavy [42] were obtained.

In the last decades, a variety of non-conventional stepped bottom geometries have been tested. André [43] performed a experimental study of nappe, transition and skimming flow over stepped chutes equipped with macro-roughness: endsills at the step corners occupying the whole channel width and spaced blocks, concluding than the latter is an optimal alternative for energy dissipation, with transverse spacing larger than the width of the blocks and fixed alternately over the conventional steps. Gonzalez, Takahasi and Chanson [44] conducted measurements in a large-size laboratory facility with two step conditions: smooth and with macro-roughness, and contrary to what was expected, the results showed higher flow velocities on rough step chutes and the inception point location further downstream than for a smooth stepped chute submitted to the same flow rate. Felder and Chanson [45] conducted a physical study in a stepped spillway with a slope $1V : 2H$

and five configurations of non-uniform step heights, concluding that the rate of energy dissipation was approximately equal for uniform and non-uniform configurations, but the latter might induce flow instabilities for smaller flow rates.

Significant conclusions on the turbulent flow properties in the non-aerated region were pointed out by Amador, Sanchez-Juny and Dolz [46,47], and in the aerated region by Chanson and Toombes [48], Gonzalez and Chanson [49] and Felder and Chanson [50, 51]. These studies coincide in highlighting that the turbulence intensity in the mixing layer downstream the step edges, is associated with the large flow velocity gradients in there, and the bubble turbulence interactions downstream the inception point. Gonzalez and Chanson [49] collected experimental data in a stepped channel with $1V : 2.5H$ slope, using triangular longitudinal vanes in the step cavities to control the recirculation vortices, finding a strong influence of the vanes on the cavity recirculation patterns and the aerated flow properties, resulting in the highest rate of energy dissipation for the vanes placed in zigzag.

Given that the reduced scale physical models fail to scale viscous forces and surface tension effects [5], numerical modeling emerges as an important alternative in the research of the flow properties in stepped channels. The tools and methodologies used by different authors for the numerical modeling of skimming flow, as well as their contributions and conclusions, are described below.

For the execution of the numerical model it is necessary to start by selecting the numerical method that allows to obtain an approximate solution of the partial differential equations that describe the flow. Two widely used numerical methods are the finite difference (FD) and the finite element (FE) method, previously described in the Theoretical Framework of this thesis. Tabbara, Chatila and Awwad [52] used the FE method to model skimming flow in stepped chutes with different slopes; mainly to predict the position of the free surface, the development of the flow over the recirculation vortices and the energy dissipation, obtaining results very similar to those measured experimentally. Bombardelli, Meireles and Matos [53] emphasize the importance of modeling the non-aerated flow region, mainly for short discharges or for stepped channels that transport a large discharge, and use a finite volumes/finite differences computational method for numerical modeling, obtaining satisfactory results in agreement with experimental measurements. Benmamar, Kettab and Thirriot [54] also used the FD method to model the turbulent flow upstream of the inception point, by the development of a numerical model for the boundary layer two-dimensional flow.

Another numerical method of wide acceptance is the Finite Volumes (FV) method, which was introduced above. Unami *et al.* [55] perform the modeling of skimming flow in steps using the FE and the FV method, reaching the important conclusion that the latter requires a less computational effort. Carvalho and Amador [56] perform a comparison of flow velocities between a physical model in which the data were taken with Particle Image Velocimetry technique, and a numerical model solved with the FV method; obtaining satisfactory results.

The selection of a suitable turbulence model is of great importance for capturing the phenomena of turbulent kinetic energy production and dissipation. The eddy-viscosity isotropic models, such as the $k-\epsilon$, $k-\omega$ and $SST k-\omega$ models introduced in the Theoretical Framework chapter, are based on the Boussinesq assumption (equation (4.13)). On the other hand, the anisotropic turbulence models, such as the Reynolds stress models (RSM), calculate all the components of the Reynolds stress tensor. Morovati, Eghbalzadeh and Javan [57] used a $RNG\, k-\epsilon$ renormalization group turbulence model, in a pooled stepped spillway, and found an acceptable agreement with experimental data; in

addition they concluded that the velocity distribution and the energy dissipation vary significantly in the width of the channel. Bombardelli *et al.* [53] successfully used the turbulence models $k-\epsilon$ and $RNG\, k-\epsilon$ for the simulation of the non-aerated region, and demonstrated that although a greater range of applicability is generally considered in the $RNG\, k-\epsilon$, there are actually no significant differences between the results obtained with both. Tadayon and Ramamurthy [58] performed the comparison between the RSM and the $k-\epsilon$ models for the simulation of the flow in circular spillways, finding a greater concordance between the experimental data and the RSM results.

Besides, in skimming flow, an appropriate multiphase flow model should be selected. Volume of Fluids-VOF and Mixture model were introduced before. Chakib and Mohammed [59] performed a numerical simulation for the special case of flow over stepped channels with flat slopes, obtaining the inception point by simulating the multiphase flow with the VOF method, and finding results in agreement with the experimental data. Zhang and Chanson [60] proposed an analytical solution of the air diffusion equation for the rapidly varying flow region immediately downstream of the inception point, in stepped spillways; and the results showed an adequate concordance with experimental data of air concentrations. Qian *et al.* [61] used the Mixture model together with the turbulence models: $k-\epsilon\, Realizable$, $SST\, k-\omega$, and LES to simulate the flow in stepped chutes, and compare the results obtained with experimental data; concluding that the combination of Mixture and $k-\epsilon\, Realizable$ is the one that presents a smaller error in the simulation of the velocity profiles and the pressures field in the steps.

Although diversity of successful cases of CFD models for the simulation of skimming flow are cited, these cannot yet be established as a definitive replacement of physical models [62], since further studies are needed to determine numerical methods, turbulence and multiphase flow models that best capture the properties and relationships between variables of the phenomenon in question. Matos and Meireles [25] suggested that there is a gap today between the multiphase numerical flow models applied to skimming flow modelation and the stepped channels hydraulic design, based on Bombardelli [63] who stated that the prediction capability of these models at the aerated region isn't as good as in the non-aerated zone, then further research is required to provide two-fluid models that accurately predict skimming flow properties along all its domain.

6 Methodology

In the present thesis a numerical model of the skimming flow over a flat slope stepped channel was carried out. The stepped bottom configuration, the spillway geometry and the discharge magnitude were taken from Hunt and Kadavy [5,42] experimental set-up. Several mesh resolutions were tested until a mesh independent solution was obtained, and the mean flow velocity profiles and free-surface levels measured by Hunt and Kadavy were used to validate the results obtained with the numerical model. Finally the optimized mesh and the validated numerical model were used to study the variations of the flow velocity and pressure field, and the turbulent kinetic energy production and dissipation in the flow domain due to modifications in the step tread and riser lengths, in the relation h/l and in the bottom roughness. Three general stages were performed: information search and processing, model set-up and validation, and hydrodynamic diagnosis.

6.1 Information search and processing

A general information search was carried out that allowed the selection of the physical model and experimental data to later validate the numerical model results, and an understanding of the different variables involved in a numerical model, to be able to make the best choice about the CFD tool, turbulence and multiphase models considering an equilibrium condition between the quality of the results and the computer memory and time requirements.

6.1.1 Experimental data

Initially, a search and collection of experimental data measured in physical models of skimming flow was performed. Data of flow velocities, water depths, inception point location, air volume fraction, and energy losses should be contained. Special care was taken in that the model or prototypes from where the measures were taken, had a slope $h/l < 0.27$ so that it could be considered in the flat slopes range. A research was done about the limitations of the equipment used for the measurements, basically the range of speeds, turbulence conditions and air concentrations in which experimental reliable data could be taken without being distorted by the flow conditions.

Considering the requirements mentioned above, the experimental data of Hunt and Kadavy [5,42] was selected. They built a physical model of a two-dimensional stepped discharge (wide channel) in order to measure: the inception point, velocity profiles and energy dissipation. As shown in Figure 2, the stepped channel was constructed with a broad-crest at the entrance of $2.4m$ length, the end of which coincided with the $0.0m$ measuring abscissa and the $0th$ step or riser. The stepped bottom risers had a hight of $h = 38mm$, and the treads a length of $l = 152mm$; therefore the pseudo-bottom had a longitudinal slope of $4H : 1V$ ($14.04°$). The channel width was $1.83m$ and considering an average water depth of $0.10m$, the influence of lateral walls on flow properties along the channel's central axis was negligible. The total vertical fall was $1.50m$.

The unit discharge for which the measurements of mean flow velocity profiles were taken was $0.28m^3/ms$. The data collection was executed along the central axis of the channel and in normal sections to the pseudo-bottom at the abscissas $0.00m$, $0.61m$, $1.22m$, $1.83m$, $3.05m$, $3.66m$, $4.27m$, $4.88m$ and $5.49m$. The velocity was measured with an Acoustic Doppler Velocimeter (ADV), a Pitot tube with differential pressure transducer, and a two-tipped fiber optic probe.

The ADV used was limited by a maximum velocity of $4.6m/s$ and could not be used in highly turbulent flow conditions [42]. Therefore, it was only employed upstream of the inception point,

where the lowest velocities were found and the turbulent boundary layer had not intercepted the free surface. The Pitot tube could be used at speeds greater than the above mentioned limit, therefore it was used downstream of the inception point, and upstream as a verification of the profiles measured by the ADV. However, it is important to mention that one of the main sources of error in the measurement of pressure, and therefore in the calculation of velocity is the presence of highly aerated flows. This instrument required air concentrations below 70% [64].

Finally the two-tipped fiber optic probe can be used to measure velocity profiles and air concentrations in aerated flows. Therefore, it was employed downstream of the inception point, to verify and correct the profiles measured by the Pitot tube, mainly close to the free surface where the volumetric air fraction in the flow was greater than 70%.

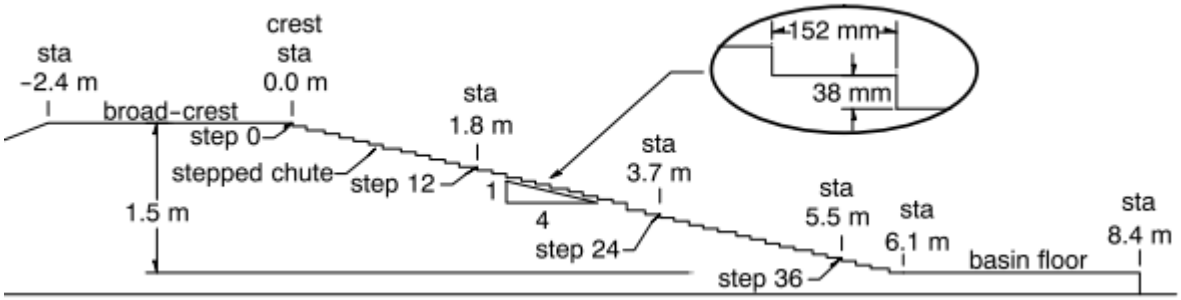

Figure 2: Schematic of the two-dimensional stepped discharge physical model geometry. Taken from [5, 42]

Figures 7 and 8 show the mean flow velocity profiles measurement results, with the three measuring instruments for a unit discharge $q = 0.28m^3/ms$. In the graphs, $U_{x'}$ represents the mean flow velocity in the channel longitudinal direction (x' axis, parallel to the stepped channel pseudo-bottom); and y' is the distance to the channel bottom, perpendicular to the longitudinal direction x'. Each measuring abscissa was then located at a step border. Upstream the air entrance point, located at abscissa $3.05m$, ADV and Pitot tube collected data had a good agreement.

Downstream the inception point where the ADV was not used, Pitot tube and fiber optic measures highly differed for the maximum y' values, because air volume fractions were certainly larger than 70% in that region close to the free surface. Accordingly, Fiber optic results are assumed to be the correct ones.

Figure 3 shows the measured mean flow void fraction (C) profiles, obtained with the two-tipped fiber optic probe downstream the inception point. Void fraction is the same as air volume fraction, so that if α is the water volume fraction, then:

$$C = 1 - \alpha \tag{6.1}$$

6.1.2 CFD tool selection and numerical models

For the CFD tool selection two choices were taken into account: OpenFOAM and Ansys Fluent. A remarkable fact about OpenFOAM is that it is open access and that the user can modify its code to add processes or algorithms that are not available in the original package. This CFD library

works with the Finite Volume Method (FVM) and all the turbulence models analyzed in this thesis investigation are contained: $k-\epsilon$, $k-\omega$, $SST\ k-\omega$ and LES. With respect to multiphase flow it contains the VOF model [65]. Regarding to the Mixture model the closure algebraic formulation for relative velocity is based in a water-slurry model (ideal for sedimentation analysis), and to be able to use it in skimming flow for the air-water interaction, modification of the original C++ code is required.

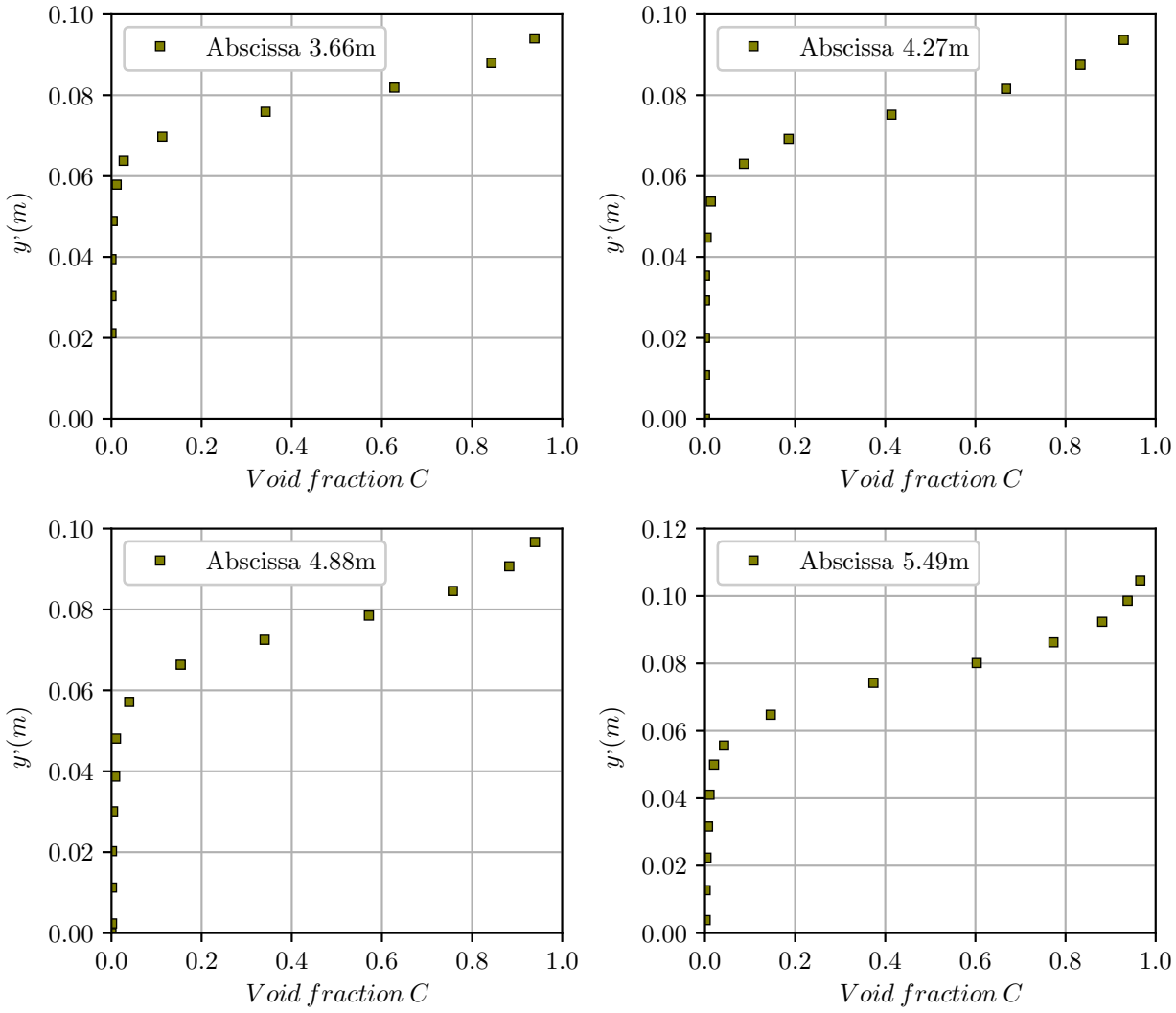

Figure 3: Measured mean flow void fraction profiles, for $q = 0.28m^3/ms$, at the abscissas: 3.66, 4.27, 4.88, and $5.49m$ - downstream the inception point. Taken from [5, 42].

ANSYS Fluent is a commercial software which main comparative advantages about OpenFOAM are its graphic interface and accessibility to information. The first one allows an easier and friendlier pre and post-processing of the model and the second is about the theoretical manual, where in comparison to the OpenFOAM's one, the user can find a rigorous description of the mathematical and physical methods involved in the modelation and their bibliographic references. A remarkable disadvantage is the impossibility to modify the source code. It works with FVM as well and the same turbulence models mentioned for OpenFOAM are available to be used in Fluent for skimming flow

simulation. In the multiphase flow case, both VOF and Mixture models are completely developed to be used in flow over stepped discharges. Contrary to OpenFOAM, relative velocity closure model described in equations (4.28) to (4.32) is available. To be able to compare and validate the results obtained with both: VOF and Mixture, ANSYS Fluent was used in the present research.

Information was searched about the turbulence models: $k-\epsilon$, $k-\omega$, $SST\ k-\omega$ and LES. Initially an understanding of the theoretical background for each of the models was conducted, giving special attention to the comparative advantages and disadvantages of applying each of them for general turbulence cases. For the first three cases which can be grouped in two equations RANS turbulence models and differ because of the second variable used to calculate the turbulent velocity and length scales (ϵ or ω), a research was made of the prediction capacities at the boundary layer and at the free stream zone, as well as the boundary conditions at atmosphere, inlet, outlet and wall frontiers. A study was accomplished of the suitability to completely model the flow properties through the whole boundary layer including the viscous sub-layer and the consequent mesh requirements in the stream-wise and span-wise direction. It was also important to study the model's behaviour at zones with phenomena special of skimming flow like the boundary layer separation at the step cavities. The above theoretical research was completed with academic articles in which the turbulence models were used and them compared with experimental data, concluding about the ones that better fit the flow profiles measured at physical models. With respect to LES, the consequences of directly solving the larger scales, in the mesh and time resolution were investigated arriving to the conclusion that it requires a three-dimensional mesh and a transient solution, while the RANS models could be applied in bi-dimensional meshes with a steady solution. Academic papers in which the advantages of using a LES model for the representation of skimming flow properties were also considered.

The research papers with different combinations of the turbulence and multiphase flow models were analysed, giving special importance to the comparative advantages of applying the VOF or the Mixture model and the differences of combining them with RANS or LES. The mentioned investigations were completed with the verification of the ANSYS Fluent available tools and boundary conditions, to correctly set-up the turbulence and multiphase numerical models. Finally the selection of one turbulence and one multiphase flow numerical model to be later used in the CFD tool was fulfilled.

6.2 Model set-up and validation

6.2.1 Initial numerical modeling

The development of this stage consisted roughly in the numerical modeling of Hunt and Kadavy [5, 42] physical model flow conditions and stepped spillway geometry. Initially a two dimensional geometry was generated with the ANSYS assistant based in the dimensions presented in Figure 2. Later an initial mesh composed of quadrilateral elements was generated with an arbitrary resolution, but being careful that the elements close to the wall had a minor area. Several numerical model runs were performed until the mesh resolution close to the solid boundaries fulfilled the requirements for the boundary layer solution depending on the selected turbulence model, and a mesh independent solution was obtained in all the points of the flow domain. A mesh quality report was executed in the final resolution mesh to guarantee that mesh elements of low quality didn't affect the numerical calculations.

Afterwards the general set-up of the numerical Fluent model was done. It included the definition of

whether the numerical model to be ran was transient or steady, the introduction of the phases (water and air) properties, the selection of the turbulence and the multiphase model and the configuration of the boundary conditions which included the water and air inlet, the atmosphere in the upper part, the solid bottom and the outlet. The selection of the solution methods was then performed by defining the pressure-velocity coupling and discretization schemes. Finally the initial numerical model could be ran.

6.2.2 Validation

Development of this stage consisted in the comparison between the results obtained with the CFD tool, and the selected experimental data from Hunt and Kadavy [5, 42]. The mean flow velocity profiles, mean flow free-surface level and specific energy in the measuring abscissas mentioned before, were contrasted qualitatively with graphs and quantitatively with the calculation of the coefficient of variation (CV). Since the air entrainment to the flow downstream the inception point was not captured by the numerical model in the present thesis research, the "downstream data adjustment procedure" described in detail in section 7.5.1, was proposed to be able to transform the fluid potential energy per unit volume due to the height increase produced by air entrance, into kinetic energy assuming that air entrapment never happened, and that way the numerical and experimental data could be compared under the same conditions.

6.2.3 Final numerical models

In this stage several simulations were executed with the optimum grid resolution and with the previously validated with Hunt and Kadavy [5, 42] data, turbulence and multiphase flow models; for different wall roughnesses and riser and tread lengths.

In first place, five simulations with variable wall roughnesses were executed as shown in Table 1. The same unit discharge $q = 0.28m^3/ms$, geometry of the stepped bottom, boundary conditions, mesh and numerical methods were used. $ks = 0.2mm$ corresponds to fine sands, $ks = 0.5mm$ and $ks = 1.0mm$ refer to medium sands, $ks = 4.0mm$ corresponds to coarse sands, and $ks = 10.0mm$ refers to fine gravels [66].

Table 1: Wall roughnesses $k_s(mm)$ at the stepped bottom

Run No.	$\boldsymbol{k_s(mm)}$
1	0.2
2	0.5
3	1.0
4	4.0
5	10.0

Four additional simulations with variable riser and tread lengths were done as shown in Table 2. The same unit discharge $q = 0.28m^3/ms$, boundary conditions, mesh and numerical methods were used. The same wall roughness that in the validated model, $ks = 0.0mm$, was maintained. Constants h and l in Table 2 are Hunt and Kadavy's [5, 42] step riser and tread lengths showed previously in Figure 2. It is clear that the step sizes (h and l) were modified by factors of 0.50, 0.75, 1.50 and 2.00, without changing the pseudo-bottom slope ($riser/tread$) which is $h/l = 0.25$. Equations (4.6) and (4.8) were considered to verify that skimming flow regime is accomplished in the four cases, despite the step magnitude increase.

Table 2: Riser and tread lengths

Run No.	$riser/tread$	$riser(m)$	$tread(m)$
6	$0.50h/0.50l$	0.019	0.076
7	$0.75h/0.75l$	0.029	0.114
8	$1.50h/1.50l$	0.057	0.229
9	$2.00h/2.00l$	0.076	0.305

Three additional simulations with different relations h/l were performed (Table 3). The same unit discharge $q = 0.28m^3/ms$, boundary conditions, mesh and numerical methods were used. The same wall roughness that in the validated model, $ks = 0.0mm$, was maintained. The three relations were lower than 0.27 to guarantee SK1 sub-regime flow pattern, which was sought in this thesis to satisfy the flat slope condition. Besides, Equations (4.6) and (4.8) were considered to verify that skimming flow regime was accomplished in the three cases.

Table 3: Relations h/l

Run No.	h/l	$riser(m)$	$tread(m)$
10	0.19	0.038	0.201
11	0.21	0.038	0.181
12	0.23	0.038	0.166

For all the cases, two dimensional channels in which walls are too far to perturb skimming flow properties in the central axe, were considered.

6.3 Hydrodynamic diagnosis

In this final stage, a detailed description of skimming flow properties in flat slope stepped channels, was made from the results obtained with the previous numerical modeling. A characterization of the pressure field was conducted giving special attention to the maximum and minimum pressure magnitudes along the step faces, and how these variate as a function of roughness, and riser and tread lengths. The pressure gradient in the longitudinal wall directions was used to explain the mean flow velocity profiles curvature at the wall, applying the Prandtl boundary layer simplifications [67]. The gradient was also related with the flow direction and the flow separation and reattachment phenomena. A characterization of the recirculating vortexes in the step cavities was presented and validated with experimental observations from literature, mainly in backward facing step experiments; and the mesh characteristics so that the numerical model captured the several sizes vortexes in the separation region, were presented.

A description of the turbulent kinetic energy production and dissipation fields was conducted, analysing the regions of maximum and minimum values. Several profiles along the tread and in its normal direction were analysed to conclude about the production and dissipation behaviour as a function of the distance to the wall. The non-dimensional wall distance $y+$ was also considered to describe the particularities of the turbulent kinetic energy gain and loss depending on the position inside the turbulent boundary layer. The influence of wall roughness increments at the stepped bottom, and riser and tread lengths variations in the mentioned fields and profiles was discussed, arguing about the skimming flow regions where production and dissipation rates increased or decreased. Calculations of the total production and dissipation achieved at the separation and

reattachment regions along the total channel longitude, by summing the punctual numerical results over these regions areas, was performed. With the obtained results, the fractions of the total production and dissipation at the separation region (where recirculating vortices take place) and reattachment region (where skin friction dominates) were stated.

7 Model set-up and validation

In this chapter different aspects of the model set-up and calibration are described.

7.1 Turbulence model

As it is demonstrated by Zhan, Zhang and Gong [68], numerical model of air entrance to the flow doesn't only depend on the multiphase flow model selected; but it is also a function of the turbulence model. In their research three cases are simulated: LES Smagorinsky-Lilly model for turbulence with VOF, LES Smagorinsky-Lilly with the Mixture model, and $RNGk-\epsilon$ with the Eulerian model for multiphase flow. The latter is similar to the Mixture model, but more complex because it solves the momentum equation for each of the phases involved. Despite the complexity of the multiphase flow algorithm in the third case, numerical model wasn't able to capture air entrance downstream the inception point because a RANS model was used for turbulence. Conversely, the first two cases accurately predicted mean flow air concentration with slight differences in the air volume fraction profiles, because of the LES selection for turbulence modelation. In conclusion, the largest turbulence structures are recommended to be solved for the air entrainment phenomenon to be captured. The main difference between the two initial cases in Zhan, Zhang and Gong [68] investigation, is that the mixture model allows the phases to be interpenetrating, which means that air and water volume fractions can take any value between 0 and 1 for a control volume, depending of the amount of each of them; while in VOF, volume fraction is only 0 or 1 into the phases, and can solely take intermediate values in the interface zone [19].

Despite LES is recommended to be selected to completely capture skimming flow properties, computational memory and processing demands are considerably larger than those of a RANS model. For representing Hunt and Kadaby [5, 42] physical model, a 3D geometry and mesh should be generated such that the eddy structures are solved in the span-wise direction [69]. Besides, mesh resolution demands are high close to the stepped bottom solid wall, because there, larger eddies directly solved are very small [69]. Hybrid models that use RANS in the inner region of the boundary layer, and LES outside, were taken into account and a 17 million nodes mesh resulted. The latter, combined with the transient character that a LES requires, yielded the impossibility to use LES due to time and computational requirement issues.

7.1.1 RANS model selection

If ω transport equation (4.21) is expressed as a function of ϵ with relation (4.23): $\epsilon = \beta^*\omega k$; a transport equation for ϵ is deduced from $k-\omega$ turbulence model. The resulting equation has the same terms that the one in original $k-\epsilon$ (equation (4.16)), except for an additional one called cross-disfussion term (CDT) [20]:

$$CDT = -2\sigma\nu_t \frac{\partial k}{\partial y}\frac{\partial(\epsilon/k)}{\partial y} \tag{7.1}$$

This term effect in the $k-\omega$ model is to control the increment rate of the turbulent length scale close to the wall [20]. When pressure gradients close to the wall don't exist, as $y \to 0$, $k \to constant$ and then, $\partial k/\partial y \to 0$; in consequence the CDT vanishes and both $k-\epsilon$ and $k-\omega$ have a similar performance. However, when pressure gradients are important, which is the case of skimming flow in the riser-tread cavity recirculation region, velocity gradients cause the k production term (equation (4.24)) to increase, such that $\partial k/\partial y \neq 0$ and CDT plays an important role. Due to its

absence in $k-\epsilon$, turbulent length scale close to solid boundaries is overestimated [20].

The latter is the reason why $SSTk-\omega$ is used in the present research, such that close to the stepped bottom $k-\omega$ is activated to control turbulent length scale; and far from the solid wall boundary $k-\epsilon$ is applied to take advantage of its good performance in the free stream region (where $k-\omega$ present issues) [19]. Furthermore, LES time and computational demands are relieved, because with $SSTk-\omega$ a two dimensional representation of Hunt and Kadavy stepped channel [42] can be achieved, by considering that sidewalls are far away from central axis; and a steady simulation saves a lot of computational calculation time, in the face of that unit discharge doesn't change over time ($q = constant = 0.28m^3/ms$).

7.2 Geometry and boundary conditions

Geometry for the numerical model is presented in Figure 2. The domain is divided into five frontiers: *inlet water* where water enters the domain; *inlet air* where air enters; *atmosphere* which is the top limit; *wall* which is the stepped bottom; and *outlet* that is the right boundary, where water and air leave the domain (see Figure 4). Boundary conditions used at each frontier are described next:

- *Inlet water*: A velocity-inlet boundary condition is used. A mean water velocity of $1.21m/s$ is specified such that distributed in the $0.23m$ frontier height produces a unit discharge of $q = 0.28m^3/ms$. Air velocity is set to $0m/s$ and air volume fraction is 0 as well, to guarantee that only water crosses that boundary. As turbulent kinetic energy and specific dissipation experimental data are not available, these are estimated with the approximations of equations (7.2) and (7.3) [18], where U_{ref} is the mean flow velocity; T_i is the turbulence intensity, defined as the ratio of the root-mean-square of the turbulent velocity fluctuations, to the mean velocity, where values of medium intensity (3 to 5%) can be used [18, 70]; and l is the turbulent length scale, approximated as a function of a characteristic length L, that can be assumed to be the hydraulic diameter [70]. C_μ and β^* are closure coefficients of $k-\epsilon$ and $k-\omega$ models, already presented in equations (4.17) and (4.22).

$$k = \frac{3}{2}(U_{ref}T_i)^2 \tag{7.2}$$

$$\omega = C_\mu^{3/4}\frac{k^{1/2}}{l\beta^*}, \quad l = 0.07L \tag{7.3}$$

  Turbulent kinetic energy of $0.002\ (m^2/s^2)$ and specific dissipation rate of $5\ (1/s)$, are used.

- *Inlet air, atmosphere and outlet*: A pressure-outlet boundary condition is used. A Gauge atmospheric pressure of $0Pa$ is established, and a backflow air volume fraction of 1 is defined to guarantee that in counter-flow cases, only air enters the domain.

- *Wall*: A stationary wall boundary condition is established at the channel bottom with a no-slip shear condition. A wall roughness height $k_s = 0mm$ is specified, considering that Hunt and Kadavy [5, 42] physical model has a smooth wood-made bottom in which roughness effect is negligible.

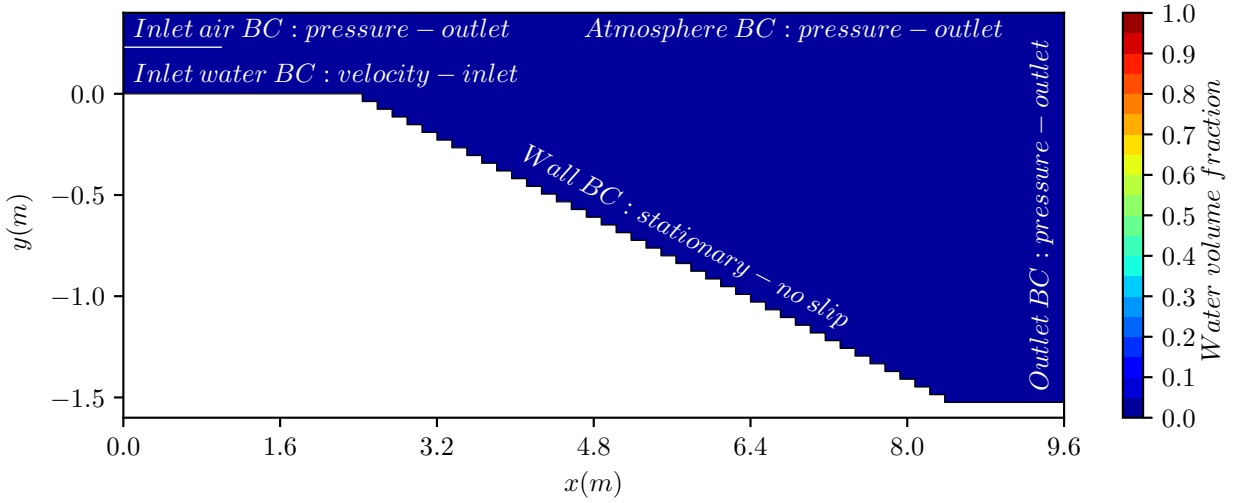

Figure 4: Initail and boundary conditions (BC) for 2D numerical modeling of Hunt and Kadavy [5, 42] physical model

As shown in Figure 4, for the initial conditions the domain is supposed to be completely filled of air ($water\ volume\ fraction = 0$), with zero velocity and submitted to Gauge atmospheric pressure ($0Pa$); and water is just about to begin to flow into the domain through the Inlet water BC.

7.3 Mesh characteristics and quality report

For mesh generation, ANSYS Fluent theory guide recommendations are taken into account, as well as a sensibility analysis of several mesh increasing resolutions, until the final output ensures that numerical results are independent of spacial discretization refinement. Mesh final characteristics are described below:

- *Near wall resolution*: $SSTk-\omega$ model is a near-wall model. Latter means that it produces a complete boundary layer solution that includes viscous sub-layer. Boundary layer can be divided in multiple layers which are limited by specific dimensionless wall distances $y+$; in viscous sub-layer, closer to the wall, Reynolds stresses are negligible, flow is dominated by viscous forces and is valid for $y+ < 5$; buffer layer is a transition region in which both viscous and Reynolds stresses are important, and is valid for $5 < y+ < 30$; log-law region is a fully turbulent zone that has a logarithmic relation between dimensionless velocity $U+$ and $y+$, and is valid for $30 < y+ < 500$ [18, 20].

  Then, first mesh nodes dimensionless distances to the stepped bottom should be approximately 1 to consider viscous sub-layer [19]. In consequence, first layer total height is $1x10^{-5}m$. Also, an inflation algorithm with 17 layers and a growth rate of 1.3 is applied to the wall BC, as shown in the *bottom right* part of Figure 5. Number of layers and growth rate is selected to fulfill ANSYS Fluent [19] recommendation: 15 to 20 cells is a desirable number to cover boundary layer.

  Additionally, an edge sizing algorithm with an element size of $1x10^{-3}m$ is applied to wall boundary. This refines the mesh in the normal direction to the previous inflation as can

be seen in the *bottom right* part of Figure 5. The size selection is made to guarantee that pressure gradients near the wall are mesh independent.

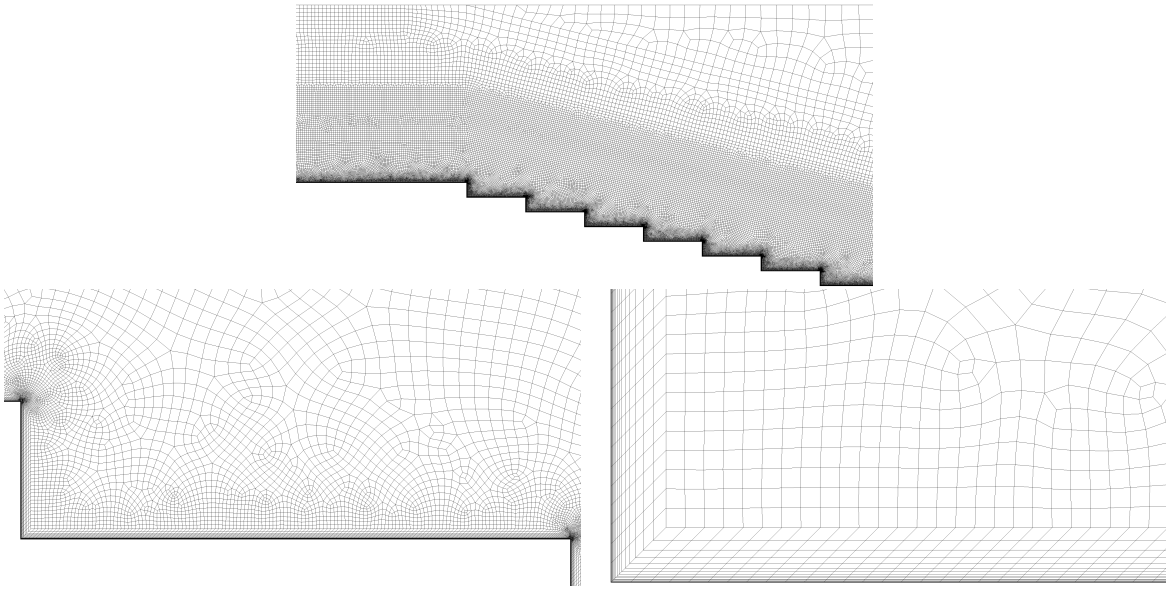

Figure 5: Numerical model mesh characteristics. *Top*: Total mesh. *Bottom left*: Zoom to one step mesh. *Bottom right*: Zoom to one riser-tread intersection

- *Water domain resolution*: In the part of the mesh where the water is expected to flow, outside the inflation zone; a quadrilateral dominant face sizing algorithm, with an element size of $5x10^{-3}m$ is applied (see the *bottom left* and the *bottom right* part of Figure 5). Element size is selected such that skimming flow properties in the boundary layer outer part, and in the free stream region, are mesh resolution independent.

- *Air domain resolution*: In the part of the mesh where the air is expected to flow; a quadrilateral dominant face sizing algorithm, with an element variant size from $5x10^{-3}m$ to $5x10^{-2}m$ is applied (see the *top* part of Figure 5). Element size is selected such that water flow properties aren't affected by mesh resolution in the air region, no matter if the air results are grid independent or not.

A resulting bidimensional mesh composed by 500241 cells and 506162 nodes is obtained. In Table 4, minimum mesh orthogonal quality, maximum aspect ratio and maximum cell skewness are presented. The first clearly satisfies the general rule that for all types of cells should be more than $1.00x10^{-2}$ [70]. Initially, very poor orthogonal quality values (lower than 0.1) are obtained in the tread-riser intersections; the solution implemented in this thesis is to apply a vertex sizing at all these intersections with an element size of $1.00x10^{-4}m$, lower than the wall edges resolution of $1.00x10^{-3}m$ justified previously, as is shown in *intermediate* part of Figure 5; increasing minimum quality value.

Maximum aspect ratio reaches a very large value, due to the high quadrilateral sides relations (or elongated shape) of the closer cells to the wall. However, the inflation growth rate of 1.3 ensures that sudden and large changes in cell aspect ratios don't occur, mainly in the tread, where rough variations can affect modelation of pressure and velocity gradients [70]. Finally, maximum

cell skewness is kept under the maximum recommended value of $9.50x10^{-1}$, which can lead to convergence problems and the need to reduce under-relaxation factors [70].

Table 4: 2D Mesh quality report

Quality property	Value
Minimum orthogonal quality	$6.53x10^{-1}$
Maximum aspect ratio	$1.02x10^{3}$
Maximum cell skewness	$7.22x10^{-1}$

7.4 Multiphase flow model and numerical properties

As mentioned before, to capture air entrapment a LES model should be used [68]. The above is ratified by Figure 6, which shows that the results of water volume fraction with $SST\ k-\omega$ are the same for both multiphase flow models considered: VOF and Mixture; and none of these reproduce air-water mixing downstream the inception point. Taking into account that air entrance phenomenon isn't captured by numerical model, experimental data is processed later to be able to compare it with numerical results. **Mixture model is used in this research as the default multiphase flow model.**

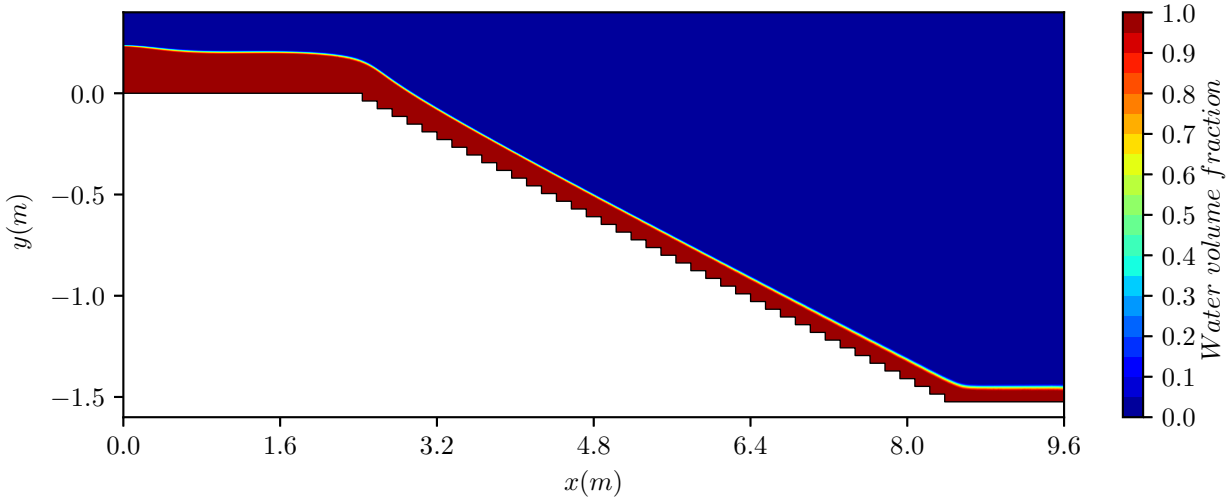

Figure 6: Water volume fraction results for two modeling combinations: $SST\ k-\omega$ + VOF, and $SST\ k-\omega$ + Mixture model

The final models, numerical methods and properties are:

- **General set-up:** Bi-dimensional (x, y spatial coordinates) and steady formulation. The gravitational acceleration vector is $\vec{g} = [0, -9.81, 0](m/s^2)$.
- **Turbulence and multiphase models:** $SST\ k-\omega$ for turbulence. Mixture for multiphase flow with Manninen *et al.* [23] formulation for the algebraic slip velocity closure expression (see equation (4.29)); and Schiller and Naumann [24] expression for the drag function f_{drag} (see equation (4.31)).

Water is selected as the primary phase, and air as the secondary, with particles diameter of $d_p = 5x10^{-3}m$.

- **Solution methods:** COUPLED is selected for the pressure-velocity coupling algorithm. *Least Squares Cell-Based* Spatial discretization scheme is selected for gradient calculation; *PRESTO!* for pressure; and *QUICK* for momentum, volume fraction, turbulent kinetic energy and specific dissipation rate.

7.5 Post-processing and validation

Experimental data of mean flow velocity profiles from Hunt and Kadavy [5,42], shown in Figure 8; which corresponds to abscissas: 3.66, 4.27, 4.88 and $5.49m$, measured with two-tipped fiber optic prove downstream the inception point; is processed so that it can be compared to the numerical results that don't take air entrance into account. Next, the data adjustment procedure is explained.

7.5.1 Downstream data adjustment procedure

At abscissas 3.66, 4.27, 4.88 and $5.49m$, equivalent clear water normal depth at each measuring point i, can be determined with equation (7.4) [71]:

$$y_{cwi}^{'} = \sum_{a=1}^{n} [(1 - C_a)\Delta y_a^{'}] \tag{7.4}$$

where:
$y_{cwi}^{'}$ is the equivalent clear water normal depth at a measuring point i.
n is the number of measuring points in the water column under point i.
C_a is the void fraction at a point a.
$\Delta y_a^{'}$ is the influence height of the measuring point a. It's assumed to cover halfway to its top $(a+1)$ and bottom $(a-1)$ points.

At each measuring point, fluid potential energy per unit volume due to the height increase produced by air entrance, is transformed to kinetic energy assuming that air entrapment never happens (as it is actually predicted by numerical model). Potential energy per unit volume, at a point i, for the water-air mixture case is determined with equation (7.5). Potential energy per unit volume, at a point i, for the only water case (assuming air entrance don't occur), is determined with equation (7.6).

$$\frac{EP_i}{Vol} = (\rho_w(1 - C_i) + \rho_a C_i)\, g y_i \tag{7.5}$$

$$\frac{EP_{cwi}}{Vol} = \rho_w(1 - C_i) g y_{cwi} \tag{7.6}$$

where:
EP_i/Vol is the potential energy per unit volume, for water-air mixture case, at point i.
ρ_w is the water density.
ρ_a is the air density.
C_i is the void fraction at point i.
g is the gravitational constant.
y_i is the water-air mixture vertical depth at a measuring point i.
EP_{cwi}/Vol is the potential energy per unit volume, for the only water case, at point i.

y_{cwi} is the only water vertical depth at a measuring point i.

In consequence, potential energy increment due to air entrapment, is calculated as the difference between equations (7.5) and (7.6). After some mathematical operations, equation (7.7) is obtained.

$$\frac{\Delta EP_i}{Vol} = \rho_w(1 - C_i)g(y_i - y_{cwi}) + \rho_a C_i g y_i \tag{7.7}$$

where:
$\Delta EP_i/Vol$ is the potential energy increment per unit volume, due to air entrance.

Potential energy increment is transformed into kinetic energy with equation (7.8):

$$\frac{1}{2}\rho_w(1 - C_i)(U_{x\cdot i+})^2 = \frac{\Delta EP_i}{Vol} \tag{7.8}$$

where $U_{x\cdot i+}$ can be easily calculated, and is the mean flow velocity increment with respect to the original measure $U_{x\cdot i}$, at point i. Then, the modified velocity is $U_{x\cdot i} + U_{x\cdot i+}$.

Mean flow modified velocities obtained with this process generate erratic velocity profiles because the maximum corrections happen close to the flow free surface; but near the wall, at approximately wall distances of 0 to $0.06m$, where $C \approx 0$ (see Figure 3); the term $\Delta EP_i/Vol$ becomes zero, and hence velocity increments too. This results should be corrected, so that the velocity profile homogenization caused by momentum transfer due to viscous diffusivity and Reynolds stresses, is considered.

With the hypothesis that with no air entrance, $SST\ k - \omega$ model generates an accurate velocity profile shape, total kinetic energy obtained by the above correction process at each measuring abscissa downstream the inception point, is redistributed such that in each measuring point, the relation between its kinetic energy and total abscissa kinetic energy is the same that in the numerical model.

Total kinetic energy per unit volume in a measuring abscissa ($KE_{measured}/Vol$), produced by the modified velocity $U_{x\cdot i} + U_{x\cdot i+}$, is found with expression (7.9).

$$\frac{KE_{measured}}{Vol} = \sum_{i=1}^{N}\left[\frac{1}{2}\rho_w(U_{x\cdot i} + U_{x\cdot i+})^2\right] \tag{7.9}$$

where N is the total number of measuring points in an abscissa. On the other hand, total kinetic energy per unit volume in the same abscissa but determined with the CFD tool (KE_{num}/Vol), is found with expression (7.10).

$$\frac{KE_{num}}{Vol} = \sum_{i=1}^{N}\frac{KE_{i-num}}{Vol} = \sum_{i=1}^{N}\left[\frac{1}{2}\rho_w(U_{x\cdot i-num})^2\right] \tag{7.10}$$

where $U_{x\cdot i-num}$ is the mean flow velocity obtained with numerical modelation, at the exact same points $i = 1\ to\ N$, of each abscissa where measures were performed. KE_{i-num}/Vol is the kinetic energy per unit volume at point i, produced by $U_{x\cdot i-num}$.

Finally, measured kinetic energy per unit volume in point i of any abscissa downstream the inception point, modified by transformation of potential to kinetic energy, and by the velocity profile shape obtained with numerical modelation (let's call it $KE_{i-measured2}/Vol$), is determined with equation (7.11).

$$\frac{KE_{i-measured2}}{Vol} = \left(\frac{\frac{KE_{i-num}}{Vol}}{\frac{KE_{num}}{Vol}} \right) \left(\frac{KE_{measured}}{Vol} \right) \tag{7.11}$$

Final measured mean flow velocity at point i, $U_{x\cdot i-final}$, modified by no air-entrance so that it can be contrasted with numerical results, is equated with expression (7.12).

$$U_{x\cdot i-final} = \left[\frac{2}{\rho_w} \left(\frac{KE_{i-measured2}}{Vol} \right) \right]^{1/2} \tag{7.12}$$

7.5.2 Validation of numerical results with experimental modified measures

For numerical model validation, upstream the inception point the root-mean-square error ($RMSE$) between $SST\ k-\omega$ + Mixture model mean flow velocity results, and measured data with both: the Pitot tube and ADV, is calculated for each abscissa.

$$RMSE = \sqrt{\frac{\sum_{i=1}^{N} \left[\left(U_{x\cdot i} - U_{x\cdot i-num} \right)^2 \Delta y_i^{\cdot} \right]}{y_{i-max}^{\cdot}}} \tag{7.13}$$

where:
$\Delta y_i^{\cdot} = [(y_{i+1}^{\cdot} - y_i^{\cdot})/2] + [(y_i^{\cdot} - y_{i-1}^{\cdot})/2]$.
$y_{i-max}^{\cdot}$ is the flow normal depth.

The coefficient of variation (CV) is then determined as the ratio of $RMSE$ to the mean velocity ($\overline{U_{x\cdot}}$) calculated with measured data (see equation (7.14)).

$$CV = \frac{RMSE}{\left(\frac{\sum_{i=1}^{N} \left[U_{x\cdot i} \Delta y_i^{\cdot} \right]}{y_{i-max}^{\cdot}} \right)} \times 100 \tag{7.14}$$

In Figure 7, mean flow velocity profiles upstream the inception point, are presented. The profiles numerically obtained have a good agreement with the measured ones, for abscissas: 0.0, 0.61, 1.22 and $1.83m$. Numerical and measured data concordance shows a reduction at abscissa $3.05m$, where air entrance phenomenon begins. The latter can be checked in Table 5 where the maximum coefficient of variation, determined with expressions (7.13) and (7.14), corresponds to abscissa $3.05m$.

In Figure 8, it is clear that there is no reason to compare numerical results downstream inception point, with experimental profiles derived from the fiber optic probe measurements, because the absence of air in the calculations of the firsts, causes a considerable coefficient of variation of approximately 20%.

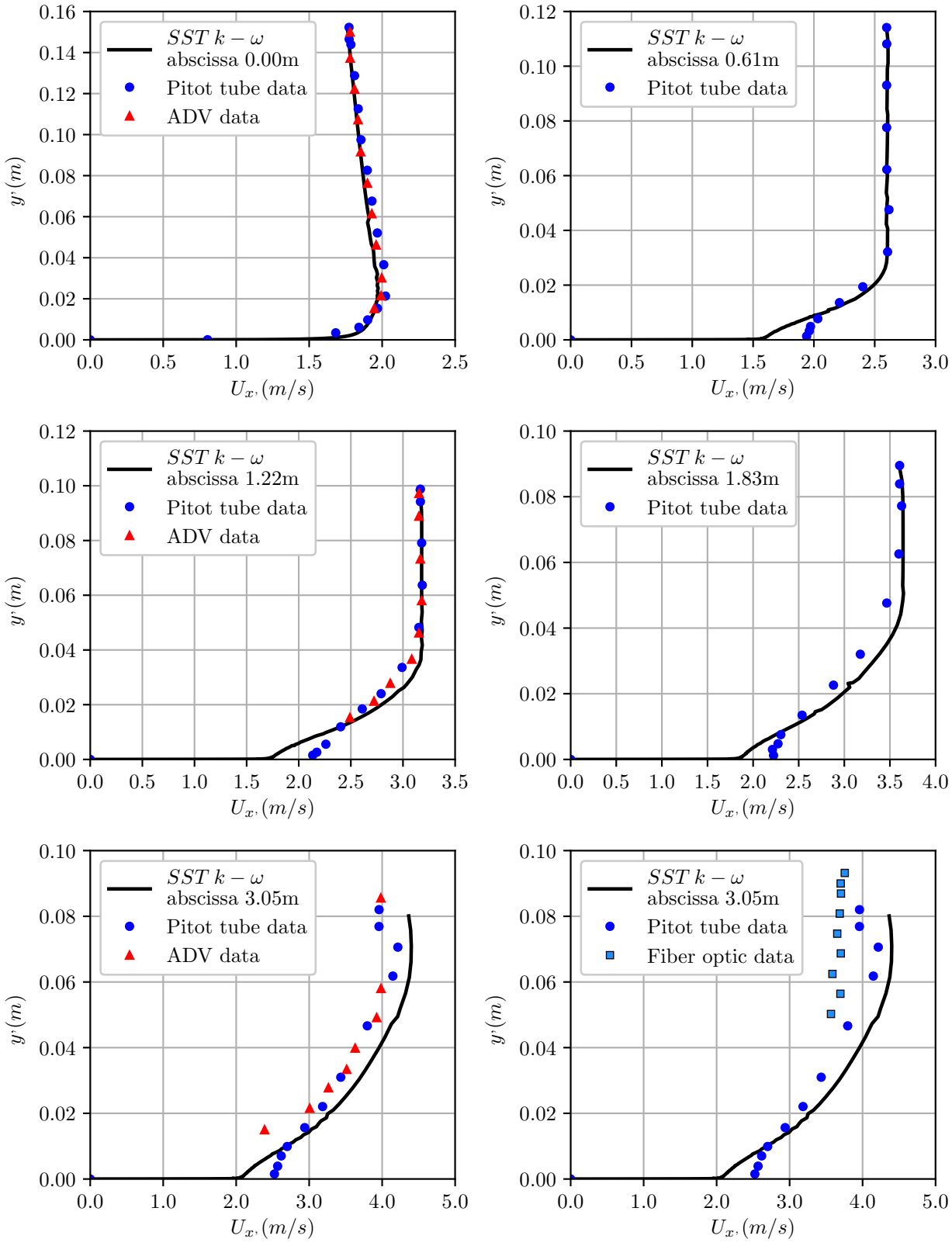

Figure 7: Modeled and measured mean flow velocity profiles for $q = 0.28 m^3/ms$ upstream the inception point

Table 5: Coefficient of variation (CV) for numerical mean flow velocity results, with respect to measured data upstream the inception point

Abscissa (m)	***CV* - Pitot tube (%)**	***CV* - ADV (%)**
0.00	2.24	1.06
0.61	2.71	–
1.22	3.98	2.54
1.83	4.47	–
3.05	7.43	11.49

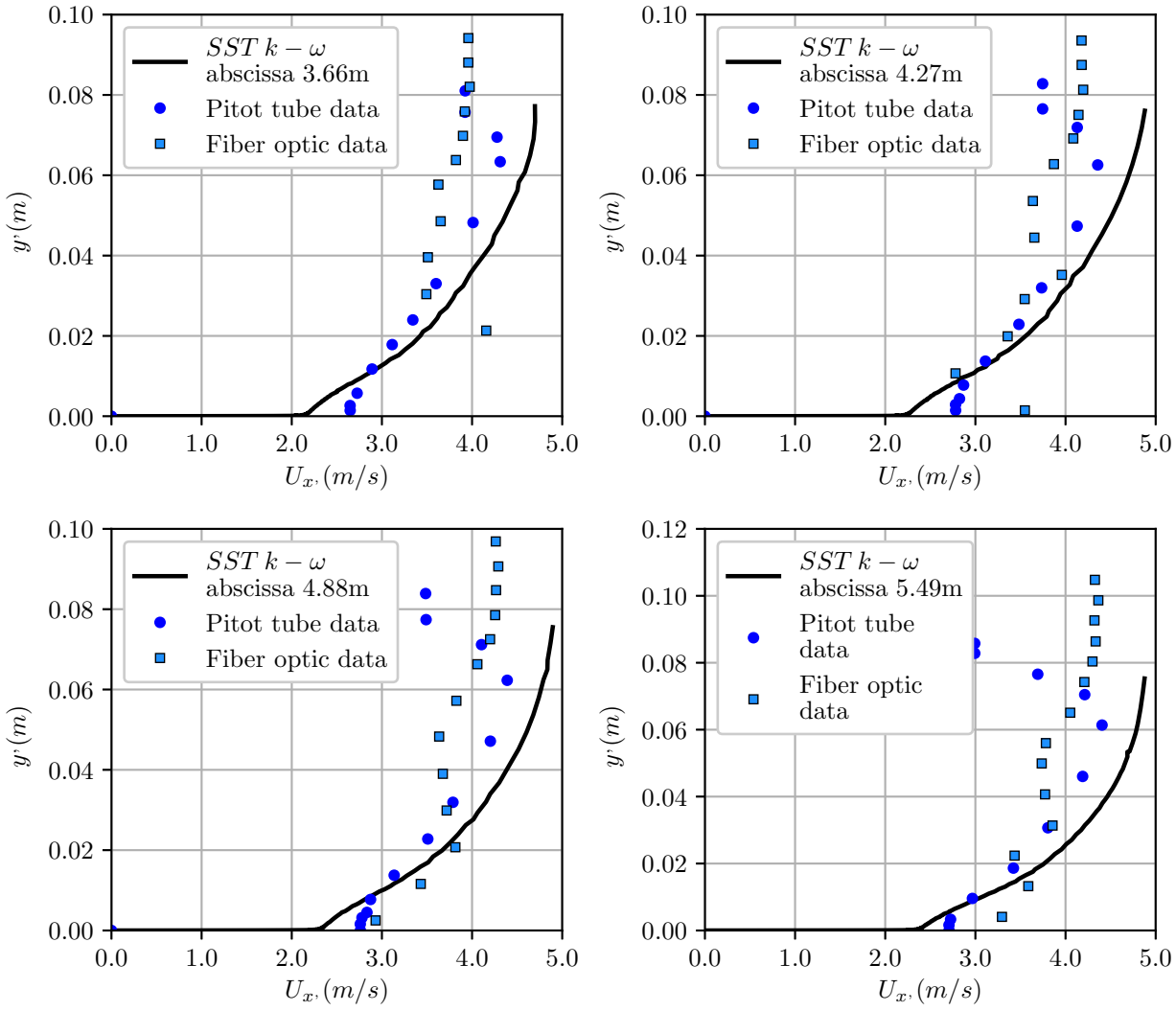

Figure 8: Modeled and measured mean flow velocity profiles for $q = 0.28 m^3/ms$ downstream the inception point

After applying the "downstream data adjustment procedure" proposed in section 7.5.1 of this thesis, with equations (7.4) through (7.12), to the two-tipped fiber optic probe measurements, Figure 8

turns into Figure 9. The profiles concordance shows a great improvement, which is reflected in the coefficients of variation in Table 6. These are also calculated with expressions (7.13) and (7.14), but $U_{x,i}$ is replaced by $U_{x,i-final}$ from equation (7.12).

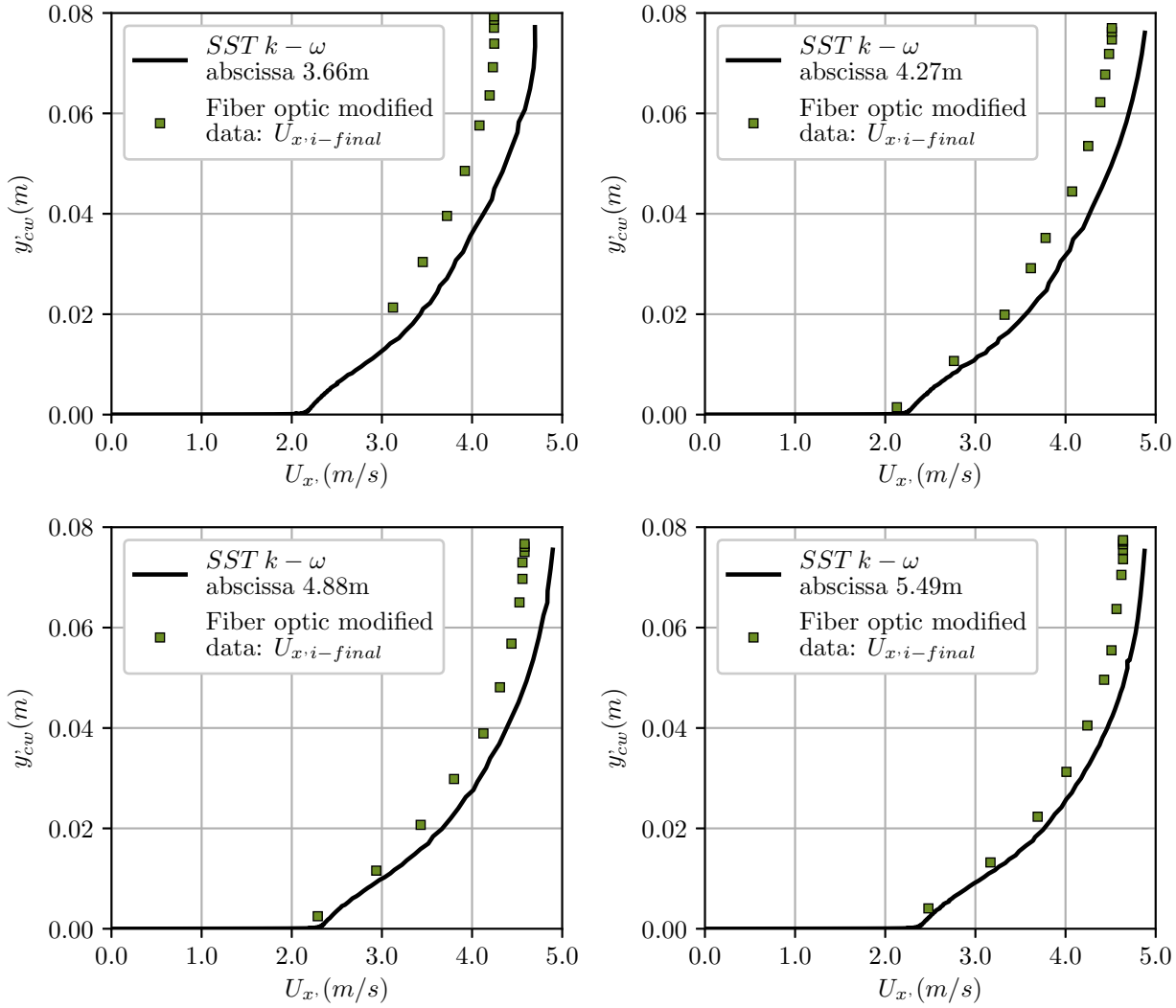

Figure 9: Modeled and measured mean flow velocity profiles modified with equation (7.12), for $q = 0.28m^3/ms$ downstream the inception point

Besides the velocity profiles, specific energies (H) for numerical model and experimental data are also contrasted. To calculate it, equation (7.15) is applied [42].

$$H = y_{i-max}^{'} \cos\theta + \alpha_c \frac{(\overline{U_x})^2}{2g} \tag{7.15}$$

where:
θ is the pseudo-bottom angle with respect to a horizontal plane.
α_c is the energy coefficient, which stands for the effect of the non-uniform velocity distribution on the energy calculation. Expression (7.16) is used to determine it [42].

$$\alpha_c = \frac{\sum_{i=1}^{N} \left[(U_{x_i^{'}})^3 \Delta y_i^{'} \right]}{\overline{U_{x^{'}}} y_{i-max}^{'}} \tag{7.16}$$

When applying equations (7.15) and (7.16) downstream the inception point, data from Figure 9 is used; it means that in stead of $y_{i-max}^{'}$, the total equivalent clear water normal depth $y_{cwi-max}^{'}$ calculated with (7.4) is considered; and in stead of $U_{x_i^{'}}$, modified mean flow velocity $U_{x_{i-final}^{'}}$ is used.

Table 6: Coefficient of variation (CV) for numerical mean flow velocity results, with respect to modified measured data downstream the inception point

Abscissa (m)	***CV* - Fiber optic modified data (%)**
3.66	11.48
4.27	8.05
4.88	6.82
5.49	5.25

In Figure 10 it can be seen that upstream the inception point, just before abscissa $3.05m$, measured and numerically modeled flow normal depths are approximately equal, thus reaffirming the conclusion obtained from Figure 7: $SST\ k-\omega$ + Mixture model make a great performance in representing skimming flow variables and characteristics upstream the air entrapment point. This is finally stated in Figure 11 where the specific energy calculated with equations (7.15) and (7.16), is graphed for the data collected upstream air entrance with the Pitot tube; downstream the inception point with the fiber optic probe, later modified by the "downstream data adjustment procedure"; and for the numerical model. In there, agreement between numerical and measured data until abscissa $3.05m$ is remarkable: a coefficient of variation of 5.65% (see Table 7), is obtained applying equations (7.13) and (7.14) to specific energy data.

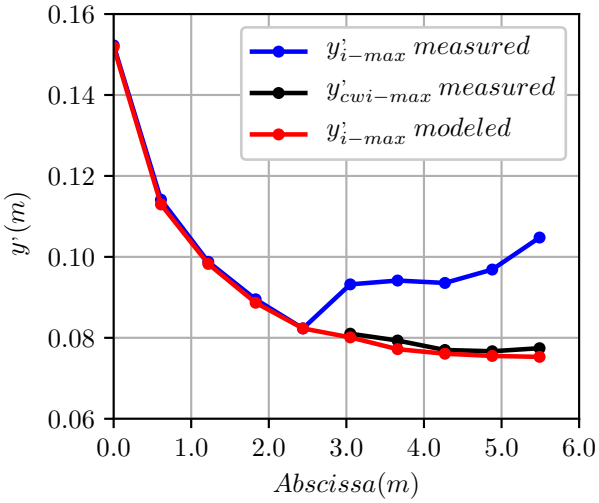

Figure 10: Flow measured, equivalent clear water and modeled normal depth

Downstream the inception point, Figure 10 shows an obvious considerable divergence between the original measures from Hunt and Kadavy [5, 42], that consider air-water mixture; and the numerically obtained flow normal depths. By applying equation (7.4), clear-water profile is derived and can be contrasted with the one from numerical model: a coefficient of variation of 1.99%, presented in Table 7, confirms the good agreement visualized in Figure 10.

For the specific energy (H) downstream the inception point, a coefficient $CV = 11.22\%$ is presented in Table 7. The higher numerical deviations respect to experimental data, occur downstream abscissa $3.05m$ as shown in Tables 6 and 7. There, energy dissipation is smaller in the numerical model, which is why in Figures 9 and 11 mean flow velocities and specific energy are a little larger, respectively. In general, numerical model results quality decreases downstream the inception point, due to the absence of air entrance phenomenon when using a RANS turbulence model; however, coefficients of variation for mean flow velocity profiles, clear water normal depth, and specific energy, vary from 2 to 11%, which is acceptable.

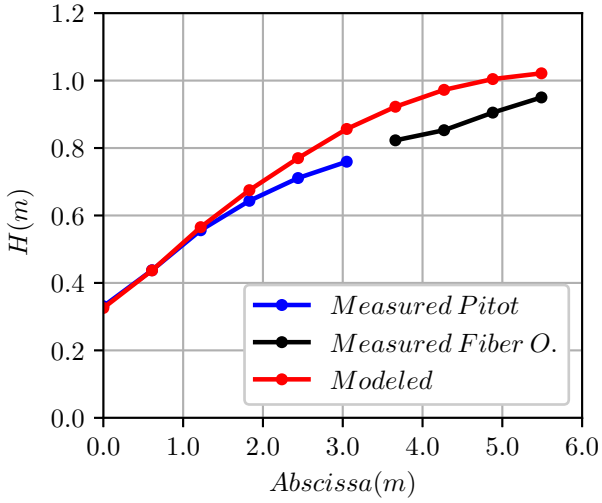

Figure 11: Measured and modeled flow specific energy (H)

Table 7: Coefficient of variation for numerical modeled mean flow normal depth (y) and specific energy (H) with respect to measured data upstream, and modified measured data downstream the inception point

Description	***CV*** **(%)**
y *upstream*	0.66
y *downstream*	1.99
H *upstream*	5.65
H *downstream*	11.22

8 Hydrodynamic diagnosis

In this chapter, variations of hydrodynamic skimming flow properties such as: mean flow pressure and velocity, turbulent kinetic energy production and dissipation, and wall shear stresses ; are described giving special attention to the areas of the domain where its magnitudes are maximum and minimum, and to the variation as a function of wall roughness, riser and tread magnitudes, and relations h/l.

Several figures with the variation of the hydrodynamic variables are presented below for a typical step. When several profiles are plotted among the tread longitude at specific distances measured from the riser, the next conventions are used:

- ***al***: indicates that the profile is obtained with the numerical model ($SST\, k-\omega$ + Mixture), at a distance from the riser equal to the fraction $\boldsymbol{a}$ of the tread length $\boldsymbol{l}$.
- $\boldsymbol{y_n}$: distance in y direction measured from the step tread.

8.1 Mean Flow Pressure and Velocity

The most important influence of surface pressure gradient at the step tread, is on boundary layer separation. By applying Prandtl boundary layer simplifications, momentum equation (4.10) in the x direction, turns into (8.1) [67].

$$\rho U_x \frac{\partial U_x}{\partial x} + \rho U_y \frac{\partial U_x}{\partial y} = -\frac{\partial P}{\partial x} + \mu \frac{\partial^2 U_x}{\partial y^2} \tag{8.1}$$

At the wall, both mean flow velocity components (U_x and U_y) are zero, so (8.1) reduces to (8.2) [67]:

$$\mu \left(\frac{\partial^2 U_x}{\partial y^2} \right)_{wall} = \left(\frac{\partial P}{\partial x} \right)_{wall} \tag{8.2}$$

where:
$\left(\partial^2 U_x/\partial y^2\right)_{wall}$ is the mean flow velocity profile curvature next to the wall.
$(\partial P/\partial x)_{wall}$ is the static longitudinal pressure gradient next to the wall. Static pressure includes the kinetic contribution associated to the flow pattern, and a hydrostatic part that accounts for the gravity effect.

Immediately downstream of each step edge, at the intersection between the riser and the tread, there is a favourable pressure gradient (negative $\partial P/\partial x$), as shown in the *left* panel of Figure 12 and the *right* panel of Figure 13. In consequence with (8.2), it can be concluded that $\left(\partial^2 U_x/\partial y^2\right)_{wall} < 0$, which can be verified in the *left* part of Figure 13 where the velocity profile curvature is negative close to the wall at $0.1l$. In that region, boundary layer water flows downstream until it reaches the adverse pressure gradient at approximately 0.2 to $0.3l$, where the flow direction turns backward (upstream direction). A small recirculation vortex that circulates in a counter-clockwise sense is formed (see the *Bottom* panel of Figure 16).

To be able to show and predict this smaller eddy, a boundary layer solved model such as $SST\, k-\omega$ was necessary. A fine grid in the x and y directions was required as well. The existence of this corner eddy, or secondary recirculation zone, has also been remarked by Scarano and Riethmuller [72] using a Particle Image Velocimetry (PIV) in a Backward Facing Step experiment. Their flow streamlines

show that the primary vortex extends from the step edge until the reattachment point, while the secondary vortex remains in the corner; and according to Hudy *et al.* [73] is maintained through the transmission of shear stress from the recirculating water of the primary vortex.

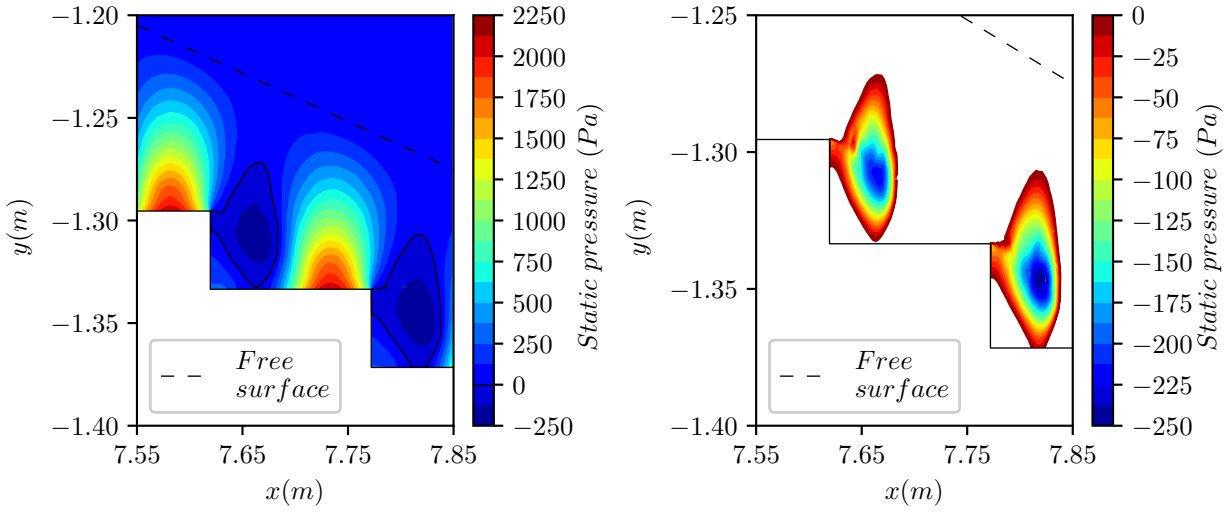

Figure 12: Mean flow static pressure P contours modeled with $q = 0.28m^3/ms$, $k_s = 0.0mm$ and $h/l = 0.25$. *Left* - Total range, *Right* - Negative range

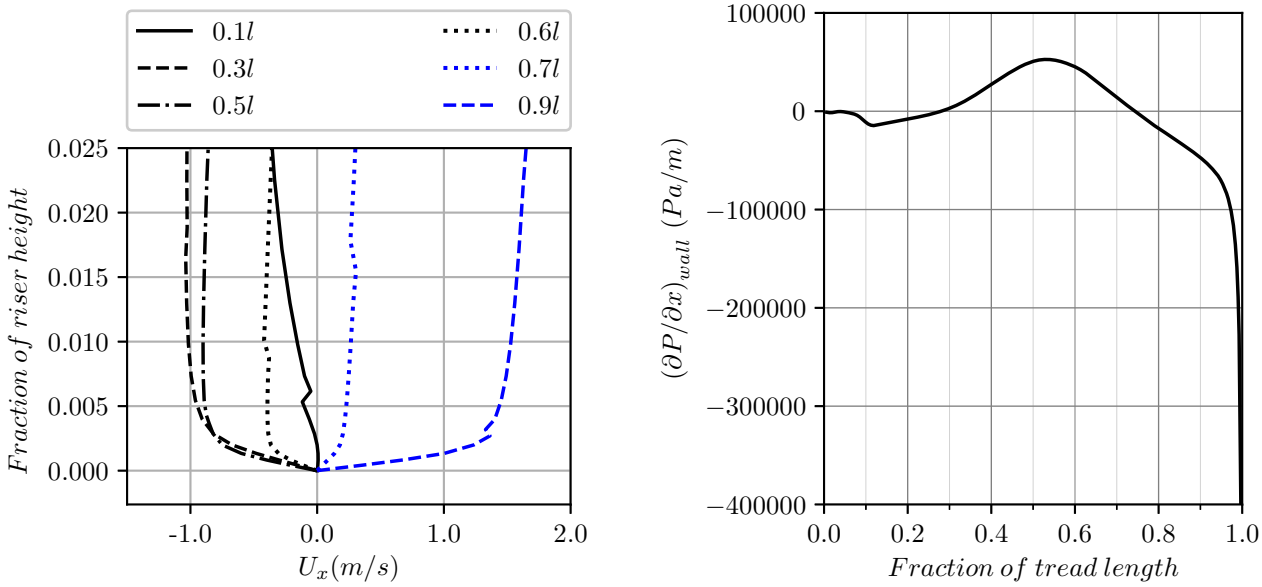

Figure 13: *Left* - Mean flow velocity profiles zoomed close to a typical tread, *Right* - Static pressure gradient at the same tread $(\partial P/\partial x)_{wall}$. Modeled with $q = 0.28m^3/ms$, $k_s = 0.0mm$ and $h/l = 0.25$

From $0.3l$ to $0.7l$ there is an adverse pressure gradient $(\partial P/\partial x > 0)$ (see Figure 12 and the *right* panel of Figure 13), so that $\left(\partial^2 U_x/\partial y^2\right)_{wall} > 0$ which can be verified in the *left* part of Figure 13,

where the velocity profile curvature is positive close to the wall at 0.3, 0.5 and $0.6l$. In that region, the adverse pressure gradient is big enough to make the flow next to the wall reverse direction and cause flow separation. That is why in the above mentioned profiles at 0.3, 0.5 and $0.6l$, which match the flow separation region close to the wall, negative velocities are found in the *left* part of Figure 13.

The boundary layer water flows upstream close to the wall, until it reaches the favourable pressure gradient explained above. There, the flow surrounds the small vortex and when reaches the riser, it flows towards the step edge (positive y direction) as displayed in Figure 16, due to the positive pressure gradient at the riser wall (see pressure contours close to the riser in Figure 12 where the pressure decreases in the y direction). Consequently, in this flow separation region, a larger recirculation vortex that circulates in a clockwise sense is found, as shown in the *top* panel of Figure 16.

Finally, downstream the separation region, from $0.7l$ to $1.0l$ a favourable pressure gradient is found (see the *right* part of Figure 13). In consequence, $\left(\partial^2 U_x/\partial y^2\right)_{wall} < 0$, which can be verified in the *left* panel of Figure 13, where the velocity profile curvature is negative close to the wall at 0.7 and $0.9l$ profiles.

Just where the adverse pressure gradient ends, and the favourable begins (approximately at $0.7l$), there is an stagnation point and the main stream reattaches the wall. Boundary water layer flows downstream until it reaches the adverse pressure gradient in the $-y$ direction of the next step riser; just at the edge, where the subsequent flow separation begins. Likewise, there is a big magnitude adverse pressure gradient in the x direction, just downstream the step edge, which is shown in Figure 14 and also ensures the vortex recirculation region formation at the next tread.

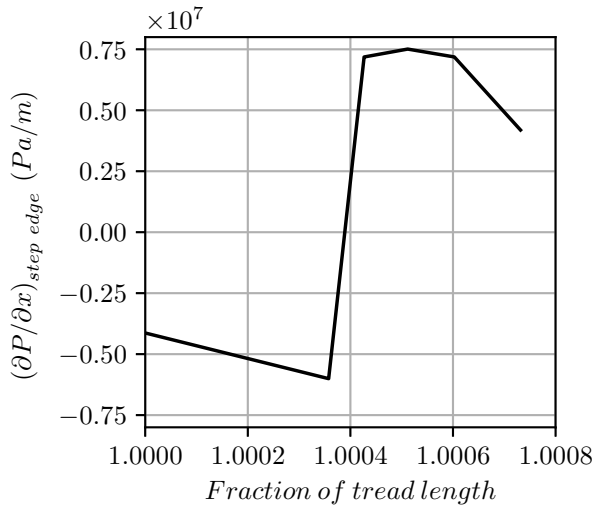

Figure 14: Static pressure gradient at a typical tread, just downstream the step edge $(\partial P/\partial x)_{step\ edge}$. Modeled with $q = 0.28m^3/ms$, $k_s = 0.0mm$ and $h/l = 0.25$

As mentioned above, velocity profiles at $0.7l$ and $0.9l$ at the attached region, have a negative curvature close to the wall. However, just above, these profiles find a point of inflection and the curvature turns to be positive (see Figure 15, where the points of inflection are reached at a fraction of the riser of less than $b = 0.25$). This can be verified with Driver and Seegmiller data

[74], measured downstream a backward facing step by a Laser Doppler Velocimeter. The positive curvature generated at the separation region, does not turn into a negative one just downstream at the reattachment region; on the contrary the flow requires a transition distance of about 32 times the step height of Driver and Seegmiller's experiment [74], so that the curvature becomes negative. In skimming flow, the presence of the next step downstream, does not allow the above mentioned complete velocity profile curvature transition, and that is why besides profiles at $0.7l$ and $0.9l$, velocity profiles at the step edges (validated ones at Figures 7 and 9) also show a positive curvature above the negative one close to the wall.

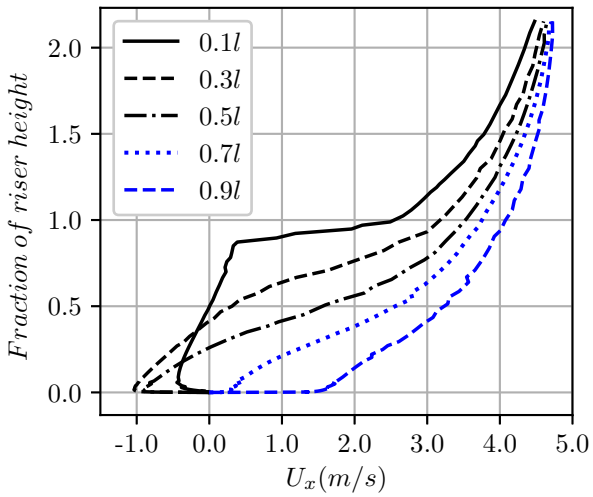

Figure 15: Mean flow velocity profiles for the total flow height. Modeled with $q = 0.28m^3/ms$, $k_s = 0.0mm$ and $h/l = 0.25$

Given that the velocity profile has to blend smoothly with the one of the main stream (flow over the pseudo-bottom), where $\partial^2 U_x/\partial y^2$ is less than zero, the positive profile curvature changes sign again and finds a second inflection point, which can be observed in Figure 15, in the five plotted curves.

8.1.1 Pressure Variations in Skimming Flow due to Wall Roughness Increments

In the previous chapter, the several regions of the boundary layer were mentioned. In this analysis, the log-law region or log-layer is brought up. In this portion of the boundary layer, which is far enough from wall so that molecular viscosity effects can be neglected compared to eddy viscosity, but close enough that advective terms can be ignored; the log-law presented in equation (8.3) relates the non-dimensional velocities $U+$ and wall distances $y+$ [20].

$$U+ = \frac{1}{\kappa} \ln (Ey+) \tag{8.3}$$

where $\kappa = 0.4$ and $E = 9.8$ for smooth walls [20]. Experiments in channels indicate that this law, modified for roughness effects has the form [70]:

$$U+ = \frac{1}{\kappa} \ln (Ey+) - \Delta B \tag{8.4}$$

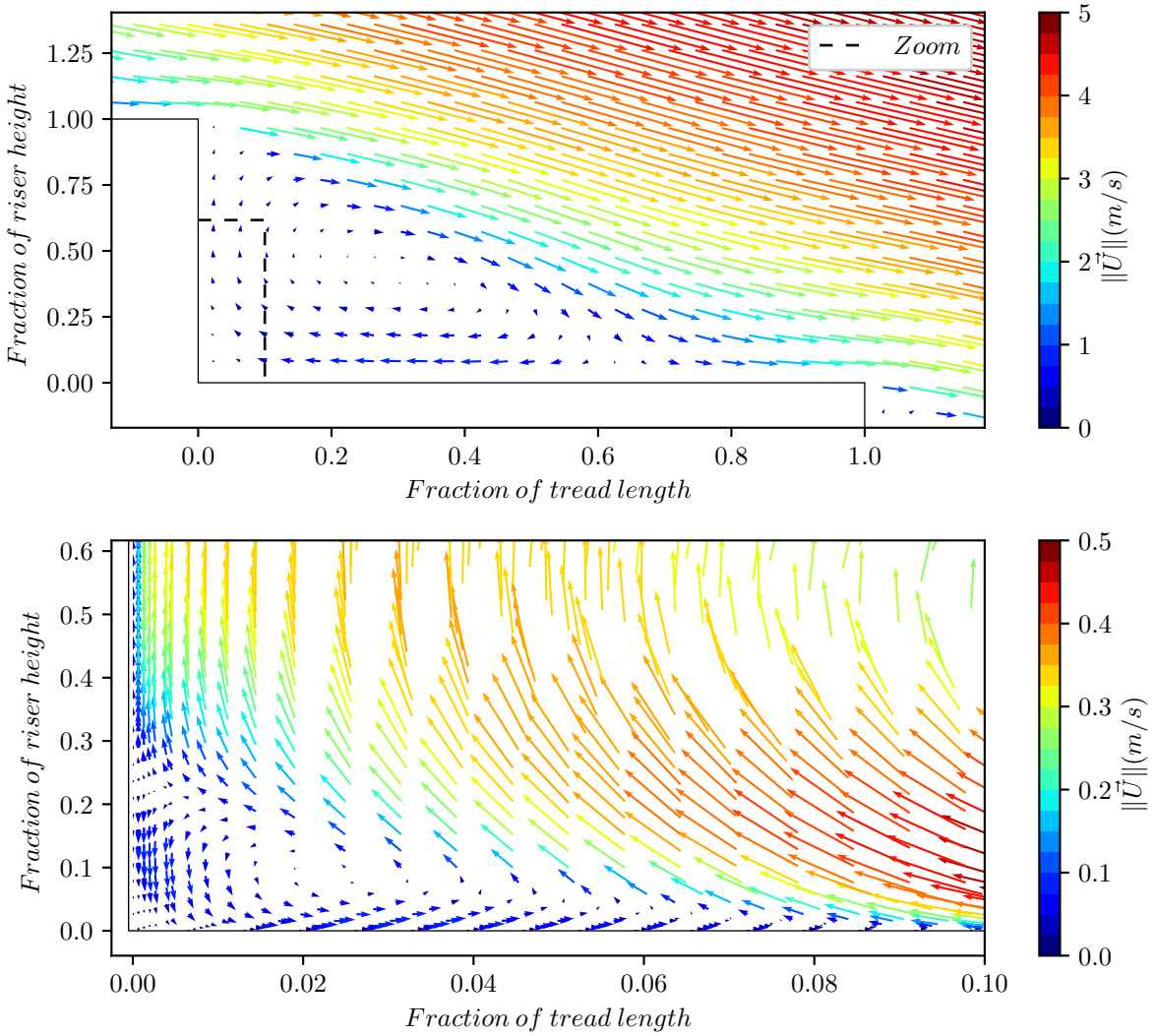

Figure 16: *Top* - Velocity vectors at a typical step. *Bottom* - Zoom of velocity vectors at the same step internal corner. Modeled with $q = 0.28m^3/ms$, $k_s = 0.0mm$ and $h/l = 0.25$

where ΔB quantifies the downward shift of the logarithmic velocity profile. This shift has been found to be well correlated with the non dimensional roughness height k_s+, which can be calculated as:

$$k_s+ = \frac{k_s u_\tau}{\nu} \tag{8.5}$$

where u_τ is the friction velocity. For ΔB determination, equations proposed by Cebeci and Bradshaw based on Nikuradse's data [75] are used in the numerical model simulations 1 through 5 (see Table 1), for which three regimes are considered: hydrodynamically smooth ($k_s+ \leq 2.25$) with $\Delta B = 0$, transitional ($2.25 < k_s+ \leq 90$), and fully rough ($k_s+ > 90$) with the largest shift ΔB.

Figure 17 shows that mean flow static pressure at $0.0l$, in the intersection between riser and tread, is not a function of wall roughness because is similar for all the k_s values tested. In the region from

$0.0l$ to $0.3l$, where $\partial^2 U_x/\partial y^2 < 0$, the effect of wall roughness is an increment of $\partial^2 U_x/\partial y^2$ value (the curvature becomes less negative), due to the ΔB shift effect of equation (8.4).

$$\left(\partial^2 U_x/\partial y^2\right)_{k_s1} < \left(\partial^2 U_x/\partial y^2\right)_{k_s2} \tag{8.6}$$

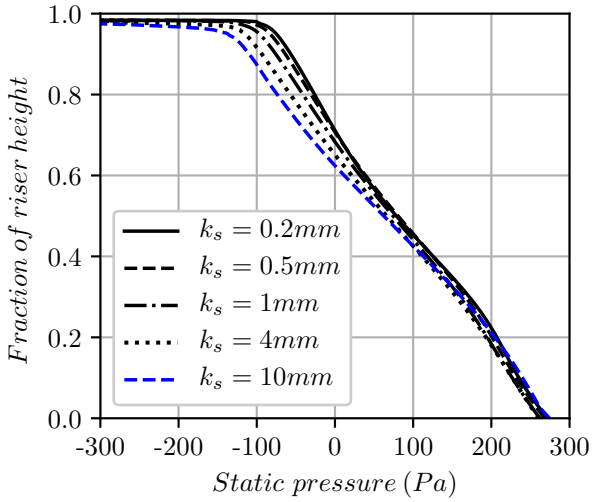

Figure 17: Mean flow static pressure P at $0.0l$ for a typical tread, for roughness k_s of 0.2, 0.5, 1, 4 and $10mm$

Then, condition of equation (8.6) is fulfilled if k_s1 is less than k_s2, which implies that $\partial P_1/\partial x$ is less than $\partial P_2/\partial x$ close to the wall. This can be verified comparing Figures 17 and 18, where it is clear that between 0.0 and $0.3l$, for larger roughnesses, the pressure gradient close to the wall is larger and in consequence the pressure decrease is smaller (if $\partial P/\partial x < 0$ between 0.0 and $0.3l$, a larger pressure gradient is a less negative one).

On the contrary in the region from $0.3l$ to $0.7l$, where $\partial^2 U_x/\partial y^2 > 0$, the effect of wall roughness increment is a decrease of $\partial^2 U_x/\partial y^2$ value (the curvature becomes smaller), due to the ΔB shift. Then, condition of equation (8.7) is fulfilled if $k_s1 < k_s2$, which implies that $\partial P_1/\partial x$ is greater than $\partial P_2/\partial x$ close to the wall. This can be verified by contrasting Figures 18 and 19, where between 0.3 and $0.7l$, for larger roughnesses, the pressure gradient close to the wall is smaller and in consequence the pressure increment too.

$$\left(\partial^2 U_x/\partial y^2\right)_{k_s1} > \left(\partial^2 U_x/\partial y^2\right)_{k_s2} \tag{8.7}$$

Finally, a roughness increment implies a smaller pressure variation at the tread close to the wall, and therefore a reduction in the magnitudes of the negative and positive pressures, at the separation and reattachment regions respectively.

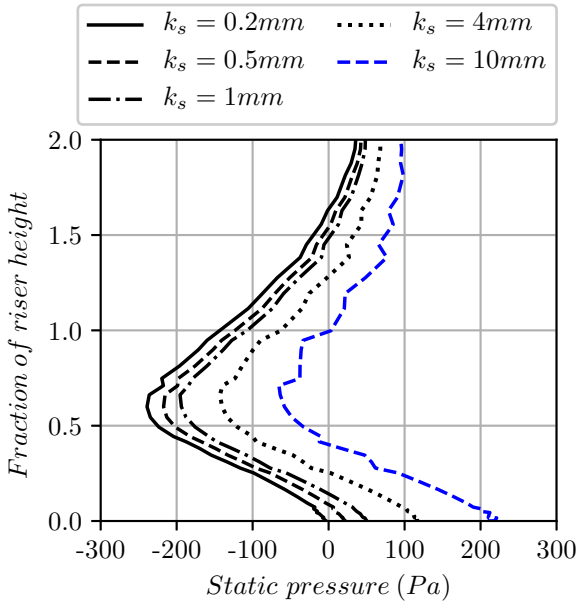

Figure 18: Mean flow static pressure P at $0.3l$ for a typical tread, for roughness k_s of 0.2, 0.5, 1, 4 and $10mm$

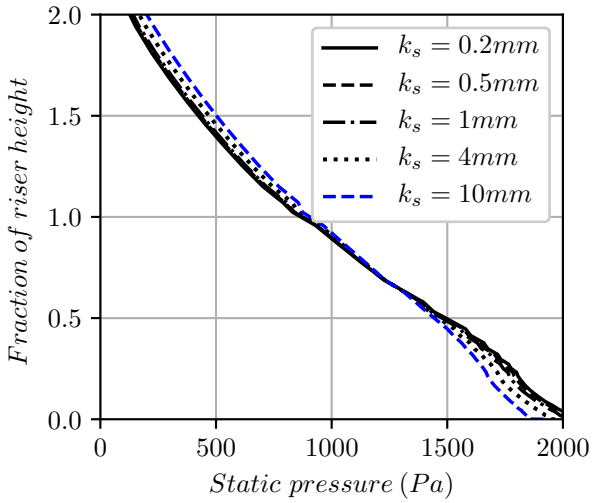

Figure 19: Mean flow static pressure P at $0.7l$ for a typical tread, for roughness k_s of 0.2, 0.5, 1, 4 and $10mm$

On the other hand, Figure 17 shows that at the riser, close to the wall, a roughness increment generates larger magnitude negative pressures, as the primary recirculation vortex flux approaches the step edge. Hence, a remarkable fact for a stepped channel designer, is that if a higher flow energy dissipation is desired through the usage of rough materials at the bottom, a low roughness or a soft finished material (in concrete for example) can be used at the riser to decrease negative pressure magnitudes at the step corners; and apply the roughness increment only at the tread.

Table 8 presents the decrease of negative mean flow static pressure at the riser upper edge, with respect to the maximum negative pressure corresponding to $k_s = 10mm$.

Table 8: Decrease of maximum negative static pressure magnitude, at a typical riser upper edge, due to lower roughness values

$k_s(mm)$	Pressure (Pa)	Pressure decrease (%)
10	-2821	Max. negative P magnitude
4	-2492	12
1	-1349	52
0.5	-1161	59
0.2	-967	66

Table 9 presents the decrease of negative mean flow static pressure at the flow separation region ($0.3l$), with respect to the maximum negative pressure corresponding to $k_s = 0.2mm$.

Table 9: Decrease of maximum negative static pressure magnitude, at a typical flow separation region ($0.3l$), due to higher roughness values

$k_s(mm)$	Pressure (Pa)	Pressure decrease (%)
0.2	-239	Max. negative P magnitude
0.5	-217	9
1	-195	18
4	-143	40
10	-65	73

Table 10 shows the decrease of positive mean flow static pressure at the flow reattachment region ($0.7l$), with respect to the maximum positive pressure, corresponding to $k_s = 0.2mm$.

Table 10: Decrease of maximum positive static pressure magnitude, at a typical flow reattachment region ($0.7l$), due to higher roughness values

$k_s(mm)$	Pressure (Pa)	Pressure decrease (%)
0.2	2060	Max. positive P magnitude
0.5	2042	0.9
1	2018	2.1
4	1967	4.5
10	1917	7.0

The main influence of roughness variations is in the negative static pressure field. A Roughness decrease at the riser causes the negative pressures to become smaller; more specifically, a change from a roughness typical of fine gravels, to one typical of fine sands can produce considerable reductions in the step corners pressures of the order of 66%. At $0.3l$, approximately at the middle section of the recirculating vortex, contrary to the riser, a reduction in the negative pressure is achieved with roughness increments, such that a variation of 73% is observed between $k_s = 0.2mm$ and $k_s = 10mm$. Despite Figure 19 and Table 10 show that actually the positive pressure field vary with roughness at the reattachment region, more specifically there is a pressure reduction close to

the wall due to a roughness rise, it is negligible; for example Table 10 indicates that a decrease of just 7% is caused by using a material with $k_s = 10mm$ instead of one with $k_s = 0.2mm$.

8.1.2 Pressure variation due to increasing tread and riser lengths, without changing relation h/l

The results obtained with numerical models corresponding to simulations 6 to 9 are analysed below. Figures 20, 21 and 22 show mean flow static pressure from the bottom of the channel, at a typical tread, at the locations $0.0l$, $0.3l$ and $0.7l$ respectively. In the ordinate axis, the vertical distance to the bottom is normalized for all the step dimensions, with respect to the riser height h of the numerical model validated with Hunt and Kadavy's experimental data.

Tables 11 and 12 present decrease of negative mean flow static pressure at the riser upper edge and at the flow separation region ($0.3l$) respectively, with respect to the maximum negative pressure corresponding to riser and tread dimensions of $2.0h$ and $2.0l$ in both cases.

Table 13 presents decrease of positive mean flow static pressure at the flow reattachment region ($0.7l$), with respect to the maximum positive pressure corresponding to riser and tread dimensions of $2.0h$ and $2.0l$ respectively.

Figure 20 shows that the positive pressure at the riser base is higher for the largest steps. As the recirculating vortex flows up parallel to the riser, the pressure decreases with the same gradient $\partial P/\partial y_n$ for all the step dimensions, and when it reaches the edge an abrupt pressure reduction occurs attaining the maximum negative pressures, which magnitude is larger for the largest step dimensions $2.00h/2.00l$ as shown in Table 11, and reducing the riser and tread lengths to $0.5h/0.5l$ causes a negative pressure decrease of 47%, as the same pressure gradient acts in a shorter riser.

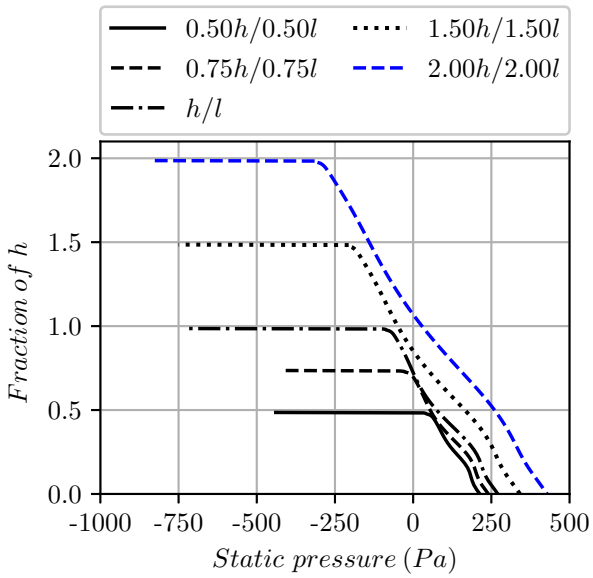

Figure 20: Mean flow static pressure P at $0.0l$ of a typical tread, for several step sizes

Figure 21 shows that at the recirculation region ($0.3l$), positive pressures are found close to the

wall and are larger for the grater steps and tend to zero as the step dimensions decrease. The pressure becomes smaller as the distance to the wall increases, and the pressure gradient is the same independent of the riser and tread lengths. At the hight of the riser upper edge, a local maximum negative value is reached, and as the same gradient acts in longer distances in the greater steps, the maximum negative pressure is found for $2.00h/2.00l$. A reduction of 65% is obtained if $0.50h/0.50l$ riser and tread dimensions are used, as shown in Table 12. Outside the recirculation vortex, the pressure starts growing with similar gradients for all the step dimensions until it turns positive close to the free surface.

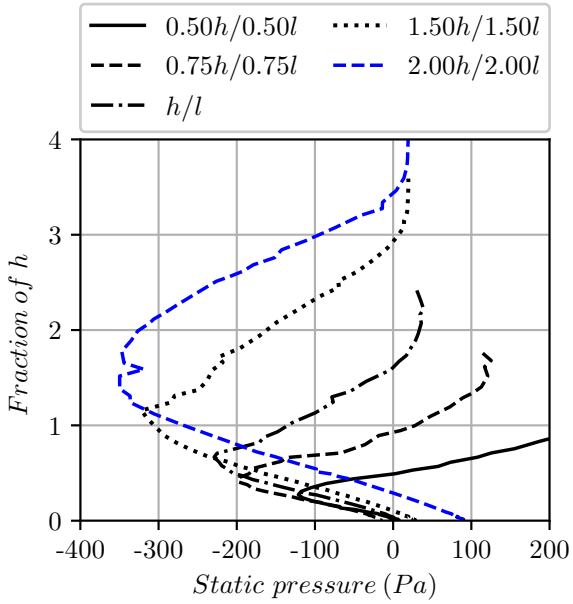

Figure 21: Mean flow static pressure P at $0.3l$ of a typical tread, for several step sizes

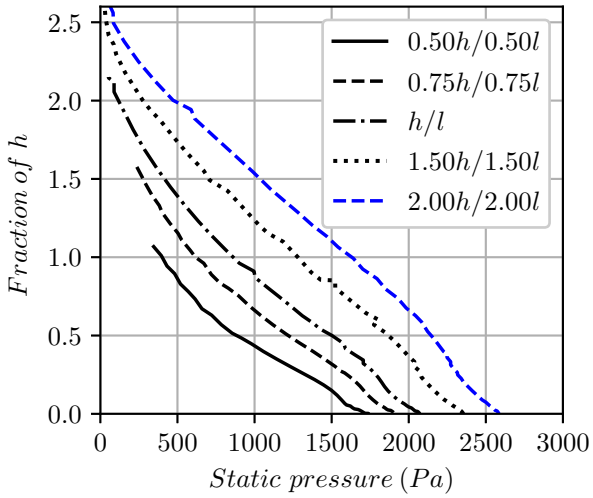

Figure 22: Mean flow static pressure P at $0.7l$ of a typical tread, for several step sizes

At the reattachment region ($0.7l$), Figure 22 shows the largest positive pressures at the wall for the greater step dimensions. Reducing the riser and tread lengths from $2.00h/2.00l$ to $0.50h/0.50l$ causes a 33% reduction in the pressure magnitude (see Table 13). As well as at the riser and at the separation region, the pressure decreases with a similar gradient for all the step dimensions and tends to zero as the flow moves away from the bottom and approaches the free surface.

Table 11: Decrease of maximum negative static pressure magnitude, at typical upper edge, due to shorter riser and tread lengths

Riser/Tread	**Pressure (Pa)**	**Pressure decrease (%)**
$2.00h/2.00l$	-826	Max. negative P magnitude
$1.50h/1.50l$	-750	9
h/l	-730	12
$0.75h/0.75l$	-407	51
$0.50h/0.50l$	-439	47

Table 12: Decrease of maximum negative static pressure magnitude, at typical flow separation region ($0.3l$), due to shorter riser and tread lengths

Riser/Tread	**Pressure (Pa)**	**Pressure decrease (%)**
$2.00h/2.00l$	-350	Max. negative P magnitude
$1.50h/1.50l$	-322	8
h/l	-229	35
$0.75h/0.75l$	-199	43
$0.50h/0.50l$	-121	65

Table 13: Decrease of maximum positive static pressure, at a typical flow reattachment region ($0.7l$), due to shorter riser and tread lengths

Riser/Tread	**Pressure (Pa)**	**Pressure decrease (%)**
$2.00h/2.00l$	2584	Max. positive P magnitude
$1.50h/1.50l$	2352	9
h/l	2070	20
$0.75h/0.75l$	1908	26
$0.50h/0.50l$	1739	33

Chanson *et al.* [71] proposed expression (8.8) to estimate the Darcy friction factor f, of the skimming flow flowing over the recirculating fluid underneath the pseudo-bottom, where the steps act as a macro-roughness. The expression is valid for flat chutes ($\alpha < 20°$), and is based on the correlation between the friction factor and the relative step roughness height ($h\cos\alpha/D_H$, where D_H is the channel hydraulic diameter); and is obtained from an adjustment to experimental data measured in approximately 38 model studies.

$$\frac{1}{\sqrt{f}} = 2.43 - 0.267\ln\left(\frac{h\cos\alpha}{D_H}\right) \tag{8.8}$$

Table 14 presents the Darcy friction factor calculated with (8.8) for all the tread and riser lengths modeled. Clearly, there is a direct proportionality between the step dimensions and the friction

factor. Figures 23 and 24 show the dynamic pressure variation with distance to the channel bottom y_n, where the dynamic pressure is the mean flow kinetic energy per unit volume:

$$Dynamic\,pressure = \frac{1}{2}\rho(U_i)^2 \tag{8.9}$$

Table 14: Darcy friction factor f calculated with equation (8.8) for several step sizes

Riser/Tread	f
$0.50h/0.50l$	0.101
$0.75h/0.75l$	0.108
h/l	0.114
$1.50h/1.50l$	0.122
$2.00h/2.00l$	0.129

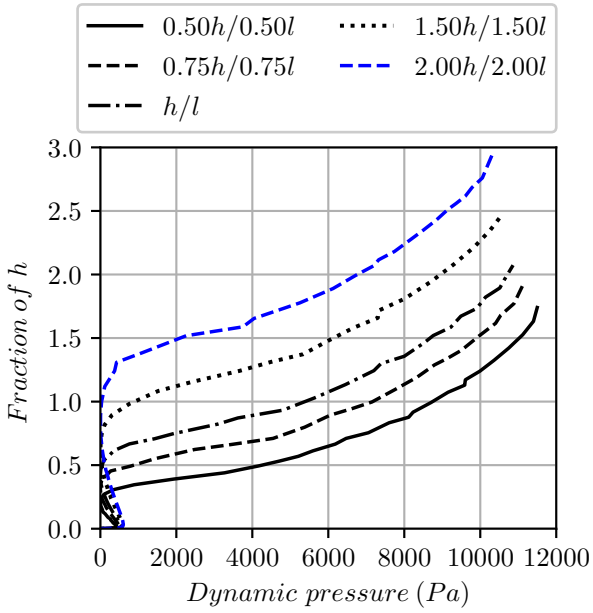

Figure 23: Mean flow dynamic pressure at $0.3l$ of a typical tread, for several step sizes

The results in mentioned Figures agree with the Darcy friction factor increase as a function of the riser and the tread growing dimensions. At the flow separation region ($0.3l$) and the flow reattachment region ($0.7l$), Figures 23 and 24 respectively, show that for step larger dimensions there is a higher flow kinetic energy dissipation, and consequently Dynamic pressure (and obviously mean flow velocities) decreases.

It was concluded from Figures 20, 21 and 22 that defining smaller tread and riser lengths ensures considerable pressure reductions at the walls, in both the separation and reattachment regions. On the other hand, Figures 23 and 24 and Table 14 relate the step dimensions increments with a friction factor rise, and the consequent higher energy dissipation. Therefore, it is an important fact for a step chute designer, that if a higher kinetic energy dissipation of the flow is meant to be

achieved through the step dimensions increment, a remarkable rise of the pressure magnitude occur along the whole bottom, as it is shown in Tables 11, 12 and 13. Then, step dimensions should be designed, such that the desired dissipation is reached without generating damaging pressures for the channel structural integrity.

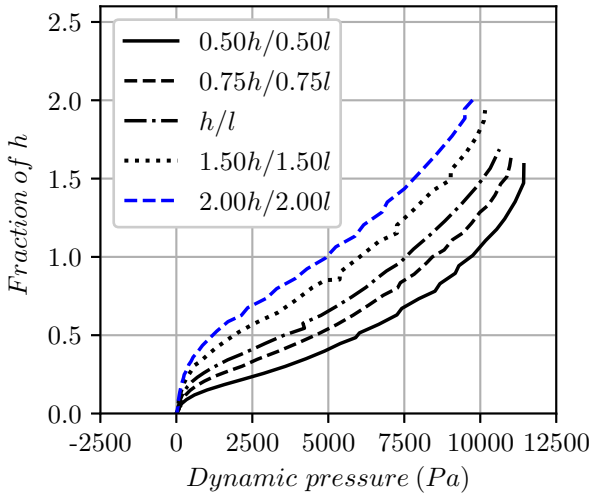

Figure 24: Mean flow dynamic pressure at $0.7l$ of a typical tread, for several step sizes

8.2 Turbulent kinetic energy production and dissipation rate

Next, turbulent kinetic energy production and viscous dissipation rate, G_k and ϵ, introduced in equations (4.23) and (4.24) respectively, and their variations within the domain are analysed. G_k term is divided by air-water mixture density ρ_m (see equation (4.26)), so that it can be compared with ϵ, as both come up with the same dimensions. As it is shown in the left and right panels of Figure 25, production and dissipation variation forms a pattern along the stepped channel, which repeats in each step. The latter means that the magnitude of these two variables changes in the stream-wise direction, but the gradients and maximum and minimum regions, are coincident in each riser-tread concavity. Besides, by comparing the mentioned panels, it can be concluded that regions of high and low production correspond to regions of high and low dissipation, respectively; and only excluding some areas (mainly those close to the wall in the recirculation zone, where there is low production but hight dissipation), the skimming flow regime under the specified conditions: $k_s = 0.0mm$ and $h/l = 0.25$, is not far from a local equilibrium condition.

The maximum values of production and dissipation are achieved at each step corner, where the maximum magnitudes of the modulus of the mean rate-of-strain tensor S are found, due to the velocity gradients caused by the presence of the bottom wall upstream, and the start of the separation region downstream.

With respect to these maximums, it is necessary to clarify that the color bars of Figure 25, in spite of having their tops in 60 and $50m^2/s^3$ respectively, in the seek of a better visualization of the contours; profiles of the *right* panels of Figures 26 and 27 at $1.0l$ of a typical tread, corresponding to the step corner, show that the real maximums are much higher: $1000m^2/s^3$ for the production and $1200m^2/s^3$ for the dissipation. As displayed in the *right* panels of those Figures, at the

reattachment zone, G_k and ϵ are large close to the wall, because of the friction with the solid boundary. G_k peak values happen in the buffer region, where the dimensionless wall distance $y+$ varies between 5 and 30, as exhibited in $0.95l$ and $1.0l$ profiles. Dissipation peak values for the same profile locations, are presented in the *right* panel of Figure 27, and happen closer to the wall, at the viscous sub-layer ($0 < y+ < 5$) for $0.7l$, and at the viscous sub-layer and the initial part of the buffer layer ($0 < y+ < 20$) as it approaches the step corner: $0.95l$ and $1.0l$.

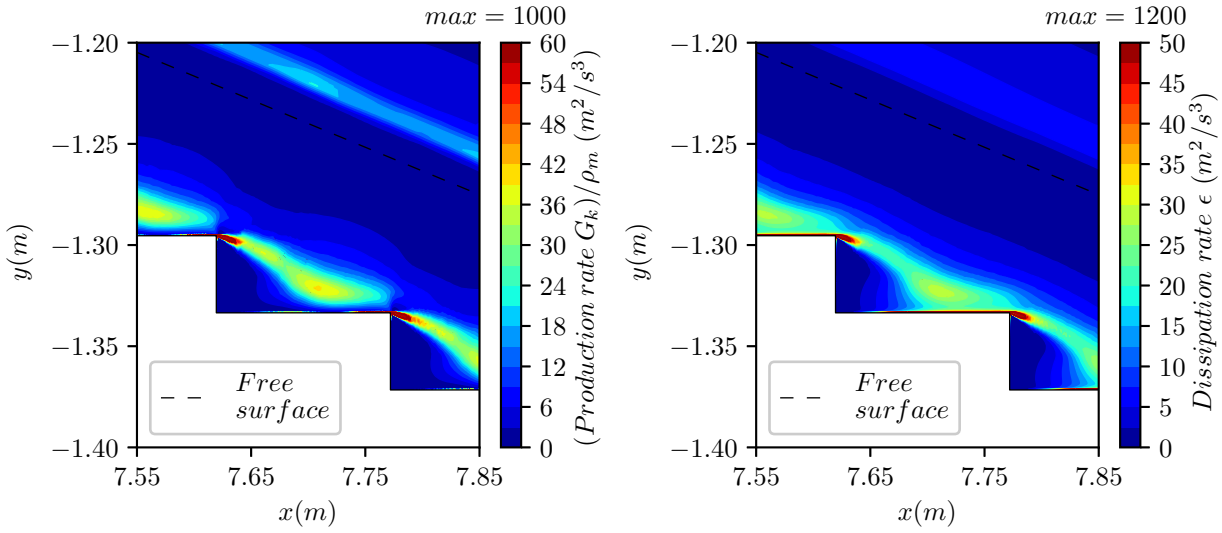

Figure 25: *Left* - Turbulent kinetic energy production rate per unit of mass contours. *Right* - Turbulent kinetic energy viscous dissipation rate per unit of mass contours. Modeled with $q = 0.28m^3/ms$, $k_s = 0.0mm$ and $h/l = 0.25$

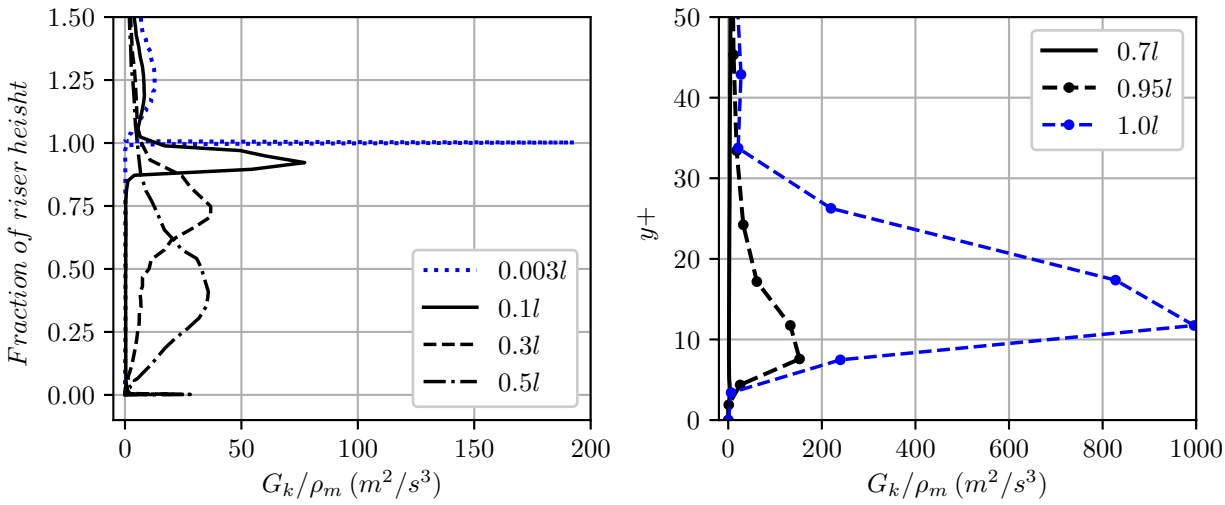

Figure 26: Turbulent Kinetic Energy production rate per unit of mass profiles, for a typical tread. *Left* - at the separation region. *Right* - at the reattachment region

Left panels of Figures 26 and 27, show that G_k and ϵ maximums at the step corner, where the

fraction of the riser height is one, and the wall distance $y_n = h = 0.038m$, extend downstream to the initial part of the recirculation vortex, as presented in $0.003l$ and $0.1l$ profiles. Below this distance, including the corner eddy area, production and dissipation are negligible.

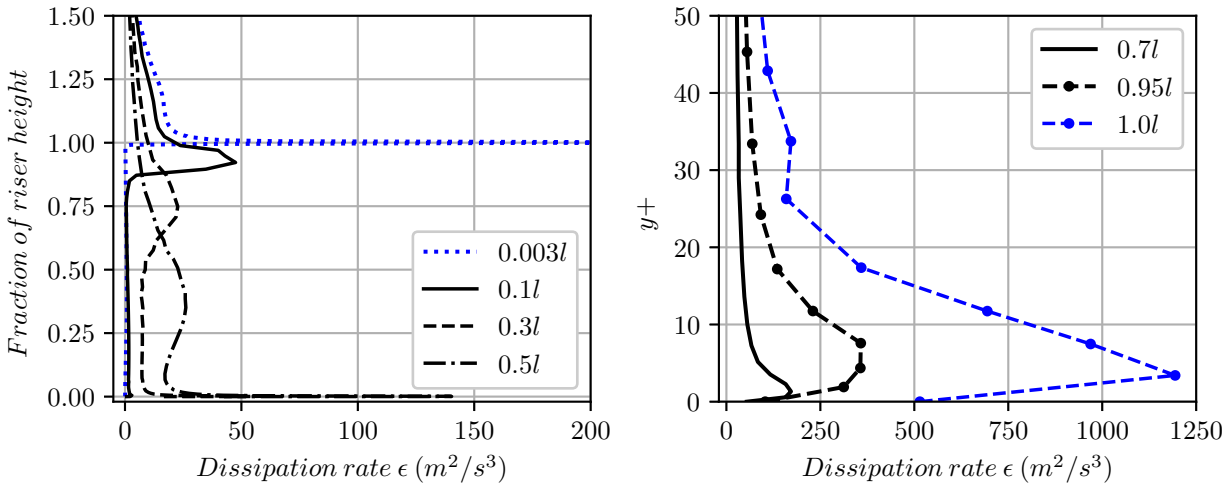

Figure 27: Turbulent Kinetic Energy viscous dissipation rate per unit of mass profiles, for a typical tread. *Left* - at the separation region. *Right* - at the reattachment region

In the remaining separation region, profiles $0.3l$ and $0.5l$, as well as the left and right panels of Figure 25, illustrate that turbulent kinetic energy gain and loss regions match the boundary between the stream passing over the pseudo-bottom, and the primary recirculating vortexes, and is due to the velocity gradients characteristic of that zone. That boundary is found at approximate fractions of the riser height of 0.75 and 0.4, for $0.3l$ and $0.5l$ locations respectively, where indeed, G_k and ϵ peak magnitudes are depicted in profiles of Figures 26 and 27. However at these locations ($0.3l$ and $0.5l$), Figures 25 and 27 show that the maximum dissipation at that zone of the separation region happens close to the wall, and is much higher than the production term.

8.2.1 Production and dissipation rate variations in skimming flow due to wall roughness

Table 15 presents the variation of the corner eddy and the total separation region (which includes the corner eddy and the primary recirculation vortex) fractions of the tread length, due to increasing wall roughnesses.

Table 15: Fraction of the tread length (l) occupied by the corner eddy and the total separation region, for the modeled k_s values

$k_s(mm)$	Corner eddy (%)	Separation region (%)
0	11.5	68.0
0.2	8.9	66.6
0.5	7.6	66.0
1	6.2	65.4
4	–	62.7
10	–	60.0

The corner eddy encompasses less and less portions of the step, as the k_s value gets higher. For k_s of $4.0mm$ and $10.0mm$, spaces are left intentionally in blank because the corner eddy disappears. Figures 17 and 18 show that between $0.0l$ and $0.3l$, the pressure gradient $\partial p/\partial x$ close to the wall is smaller for the mentioned roughnesses, being unable to generate the counter-clockwise secondary vortex. The separation region size also decreases as k_s increases, while the reattachment region ($l - separation\,region$) spans a larger portion of the tread.

To calculate the total turbulent kinetic energy production and dissipation rates, per unit channel width, expressions (8.10) and (8.11) are applied.

$$Total\ production\left(\frac{kg\,m^2}{m\,s^3}\right) = \sum_{i=1}^{n} G_{ki}A_i \tag{8.10}$$

$$Total\ dissipation\left(\frac{kg\,m^2}{m\,s^3}\right) = \sum_{i=1}^{n} \rho_{mi}\epsilon_i A_i \tag{8.11}$$

where:
G_{ki} is the production rate per unit of volume at cell i.
$\rho_{mi}\epsilon_i$ are the mixture density and dissipation rate per unit of mass at cell i, respectively.
A_i is the area of cell i.
n is the number of cells inside the region where total production or dissipation rates shall be calculated.

To obtain production and dissipation along the whole stepped channel (see Table 16), all the grid cells are used; while to obtain only production and dissipation accomplished in the separation region of a typical step (see Figure 28 and Table 17), just the cells inside that region are used. The same applies to the production and dissipation accomplished in solely the reattachment zone.

The fraction of the total turbulent kinetic energy dissipated at the separation region of a typical step, is of approximately 65% to 70% for all the modeled roughnesses, much larger than in the reattachment region, where the remaining 30% to 35% of the total is dissipated, as illustrated in Figure 28. Increasing k_s, together with its consequent reduction of the separation region size presented in Table 15, causes a decrease in the fraction of dissipation at the separation region, and an obvious increase in the reattachment zone.

Figure 28 also shows that the decrease of the fraction of total production accomplished at the separation region, due to increasing roughness, is higher than the one of the dissipation: production fraction decreases from 70% for smooth walls to 55% for $k_s = 10mm$, while dissipation decreases from 70% for smooth walls to just 65% for $k_s = 10mm$. For the highest roughnesses, production fractions at the separation and reattachment regions, tend to be equal (approximately $50\% - 50\%$).

Besides, total production and dissipation, calculated with expressions (8.10) and (8.11), are larger for higher roughness values, as presented in Tables 16 and 17, where the increments are depicted as a percentage of the minimum values found for $k_s = 0mm$. Bringing up the previous conclusion about the proximity of skimming flow in the validated numerical model($k_s = 0mm$), to a local equilibrium condition, in which total production is approximately equal to total dissipation; and taking into account that the results of Tables 16 and 17 show that production increments due to growing k_s, are much higher than dissipation increments; certainly, in high wall roughness stepped

channels, production becomes much higher than dissipation. The main influence of rugosity is in the total production and dissipation rates increments achieved in the reattachment region (see Table 17 that shows that the percentage increments at the reattachment zone are higher than in the separation zone), stressing in the fact that there, these phenomena are due to the friction with the bottom wall; while in the recirculation region are mainly produced by the gradients between the vortexes and the main stream.

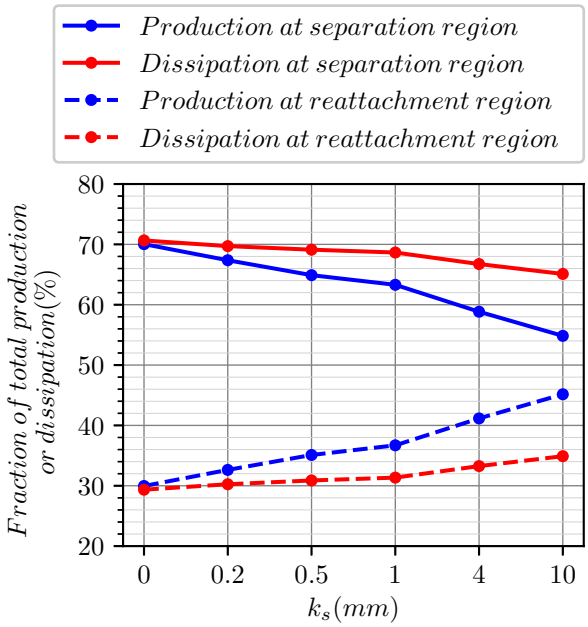

Figure 28: Fraction of total production and dissipation rates per unit channel width, at the separation and reattachment regions of a typical step, for the modeled k_s values

Table 16: Increase of total production and dissipation rates accomplished along the whole stepped channel, due to wall roughness increments; with respect to $k_s = 0$ values

k_s (mm)	Production (kgm^2/ms^3)	Production increase (%)	Dissipation (kgm^2/ms^3)	Dissipation increase (%)
0	2143.7	*Minimum*	2104.0	*Minimum*
0.2	2279.3	6.3	2128.4	1.2
0.5	2462.3	14.9	2151.6	2.3
1	2696.0	25.8	2189.9	4.1
4	3362.8	56.9	2301.9	9.4
10	4111.3	91.8	2437.1	15.8

As a complement to the above given recommendations for stepped channel designers, selecting a low roughness or a soft finished material at the riser; and selecting high roughness materials or textured finishes at the tread, mainly in its final part of 40% of the total longitude l (which coincides with the reattachment region for all the k_s values of Table 15, where the influence of roughness is higher and the height of the roughness elements doesn't perturb the recirculating vortex); besides decreasing the negative pressure magnitudes at the riser, ensures larger total

production and dissipation rates, which causes a reduction in mean flow velocity profiles. The latter can be done in the seek of preventing the mean flow static pressures and velocities to damage the channel construction materials.

Table 17: Increase of total production (*Top*) and dissipation (*Bottom*) rates accomplished at the separation and reattachment regions of a typical step, due to wall roughness increments; with respect to $k_s = 0$ values

k_s (mm)	Production (kgm^2/ms^3) separation	Production increase (%) separation	Production (kgm^2/ms^3) reattachment	Production increase (%) reattachment
0	65.8	*Minimum*	28.1	*Minimum*
0.2	66.5	1.2	32.2	14.5
0.5	68.5	4.2	37.0	31.6
1	71.7	9.1	41.6	47.8
4	80.3	22.1	56.1	99.6
10	87.8	33.6	72.3	157.2

k_s (mm)	Dissipation (kgm^2/ms^3) separation	Dissipation increase (%) separation	Dissipation (kgm^2/ms^3) reattachment	Dissipation increase (%) reattachment
6	65.5	*Minimum*	27.2	*Minimum*
0.2	65.7	0.3	28.5	4.9
0.5	65.8	0.5	29.4	8.1
1	66.1	0.9	30.2	11.0
4	66.8	1.9	33.3	22.3
10	67.1	2.5	36.0	32.3

Left and right panels of Figure 29 present production and dissipation rate profiles just downstream the step corner, at the beginning of the flow separation region at $0.003l$, illustrating how the maximum values at the corner height, become larger as k_s grows. Furthermore, the approximate local equilibrium condition for $k_s = 0mm$ profile, is reconfirmed as it has similar maximum values for both, production and dissipation. However, as the roughness increases, growth of the production maximum value is larger, until it duplicates the dissipation maximum for $k_s = 10mm$ profile.

Figure 30 presents the dissipation rate profiles for a typical tread at $0.95l$, for the modeled k_s values. The ΔB downward shift of the logarithmic velocity profile caused by the wall roughness height k_s, explained in equations (8.3) to (8.5), causes a singularity for large roughness heights and low values of y^+ characteristic of fine grids [70]. In order to avoid this issue, a virtual shift of the wall is performed. The equivalent sand-grain roughness is shown in Figure 31, in which the elements have a blockage effect of about 50% of its height, that is used to correct the first cell center $y+$ value:

$$y^+ = y^+ + K_s^+/2 \tag{8.12}$$

with this virtual shift correction, fine grids can be handled close to the wall, and the flow behaviour is correctly captured, because the viscous sub-layer is fully established only near hydraulically smooth walls ($k_s^+ \leq 2.25$), and in fully rough walls ($k_s^+ > 90$) the viscous effects become negligible as the sub-layer is embedded in the blockage effect of Figure 31 [70].

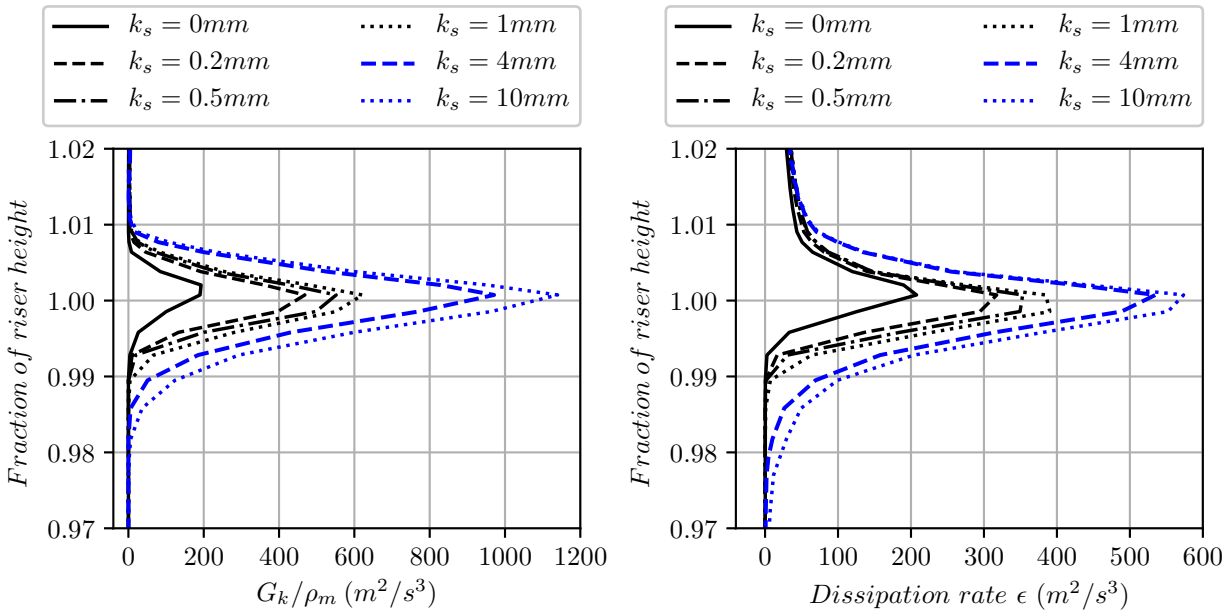

Figure 29: Turbulent kinetic energy production (*Left*) and dissipation (*Right*) rate per unit of mass profiles, for a typical tread at $0.003l$ for the modeled k_s values

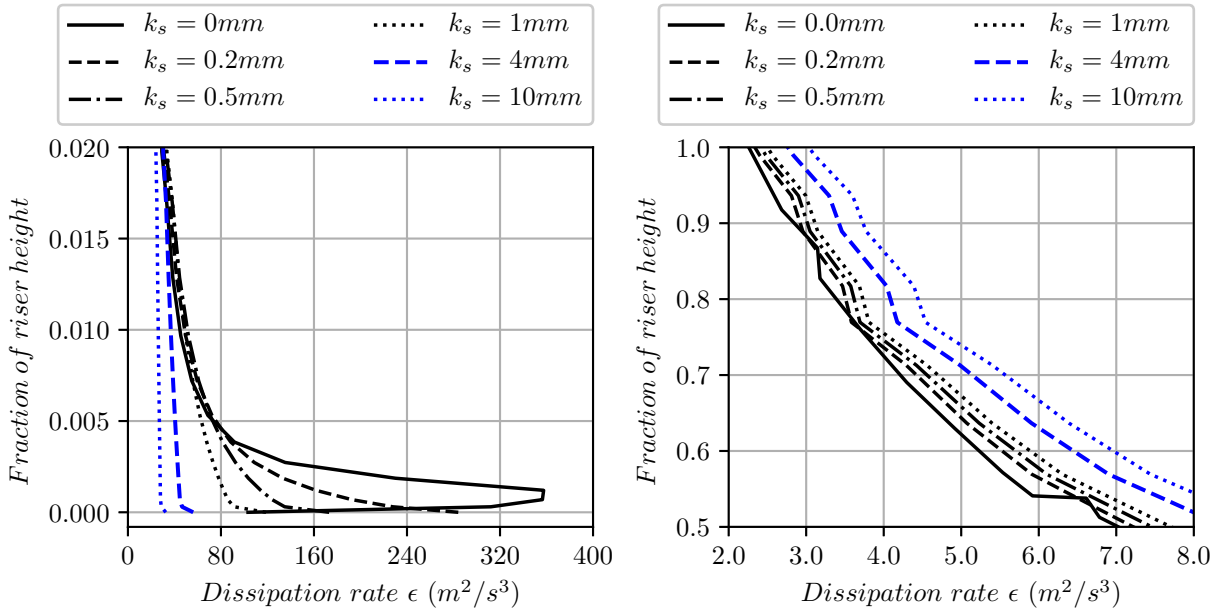

Figure 30: Turbulent kinetic energy viscous dissipation rate per unit of mass profiles, for a typical tread at $0.95l$ for the modeled k_s values. *Left* - close to the wall. *Right* - far from the wall

Table 18 demonstrates that only $k_s = 0mm$ guarantees a hydro-dynamically smooth regime and the presence of the viscous sub-layer beyond the blockage effect. As said before, the peak value of the dissipation profiles at the reattachment region, happens among the viscous and the initial

part of the buffer layer, so only for $k_s = 0mm$, the peak value is totally developed in the *Left* panel of Figure 30. For $k_s = 0.2mm$, a transitional regime is found ($2.25 < k_s^+ \leq 90$), and the ΔB shift effect causes the disappearance of the viscous sub-layer outside the $k_s/2$ blockage (no laminar flow close to the wall because of the perturbations caused by roughness height), so that the boundary layer starts with the buffer region as can be checked in Table 18; preventing the maximum dissipation value to be achieved, and thus a smaller dissipation with respect to smooth walls. For the remaining k_s values, a fully rough regime is given, and viscous effects become negligible as the boundary layer starts in the logarithmic region for roughness heights of $0.5mm$ and $1mm$, and in the external region ($y+ > 500$) for roughness heights of $4mm$ and $10mm$. The consequence is displayed in the *Left* panel of Figure 30, in which viscous dissipation decreases close to the wall as k_s magnitude grows, until for $4mm$ and $10mm$ no important increments of ϵ are perceived.

In spite of the above punctual diminution of dissipation rate close to the wall, due to roughness increments, in the rest of the domain it is higher for larger k_s values, as presented in the *Right* panel of Figure 30, so that the cumulative dissipation over the entire reattachment region area with equation (8.11) results in an increase of total dissipation as roughness heights become larger, like depicted in Table 17.

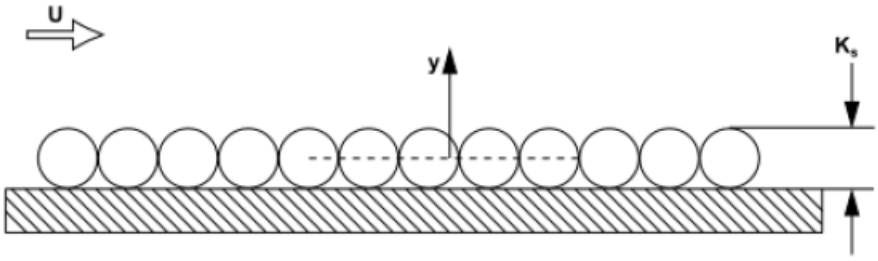

Figure 31: Virtually shifted wall procedure for wall roughness modeling in ANSYS Fluent. Taken from [70]

Table 18: Dimensionless roughness k_s^+ and wall distance values y^+, for a typical tread at $0.95l$ for the modeled k_s values

$k_s(mm)$	k_s^+	y^+
0	0	0.83
0.2	41.87	21.98
0.5	119.04	60.71
1	257.87	130.22
4	1189.01	595.99
10	3237.63	1620.37

The effect of roughness increments on the energy production rate close to the wall, at $0.95l$, is adverse to the one analized for the dissipation rate. As it is shown in the *Left* panel of Figure 32, the transition from a hydro-dynamically smooth regime for $k_s = 0mm$, to a fully rough regime for $k_s = 10mm$, generates a considerable increment of turbulent kinetic energy production at the wall. The latter, together with the fact that far from the wall the profiles show larger production at all points for higher k_s values, as shown in the *Right* panel of Figure 32, is the reason why when summing over the complete reattachment region area, total production rate percentage increments

of even 157% for $k_s = 10mm$, are displayed in Table 17.

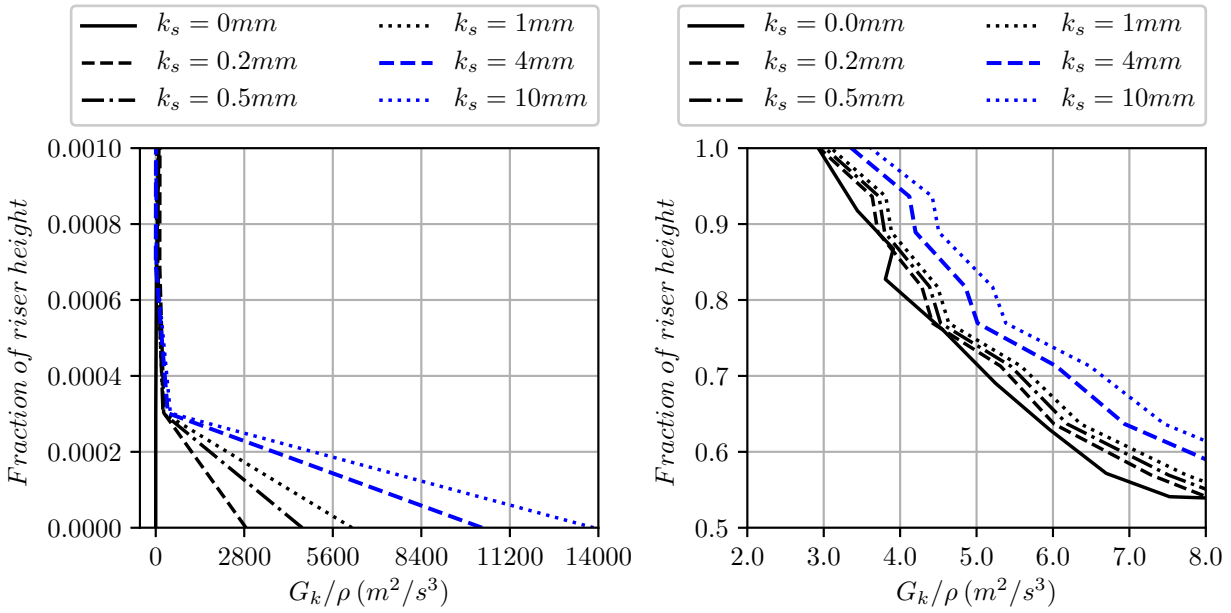

Figure 32: Turbulent kinetic energy production rate per unit of mass profiles, for a typical tread at $0.95l$ for the modeled k_s values. *Left* - close to the wall. *Right* - far from the wall

8.2.2 Production and dissipation rate variations due to increasing tread and riser lengths, without changing relation h/l

Table 19 presents the variation of the corner eddy and total separation region fractions of the tread size, due to increasing riser and tread lengths. The corner eddy spans smaller portions of the step, as the riser and tread lengths grow without changing the pseudo-bottom slope. The changes in the fraction of the tread occupied by the separation region are negligible, and as the wall roughness is set constant with a value of $k_s = 0mm$, the fraction of the total production and dissipation that take place in the separation and reattachment region, are approximately 70% and 30% respectively, for all the modeled riser and tread lengths: $0.50h/0.50l$, $0.75h/0.75l$, h/l, $1.50h/1.50l$ and $2.00h/2.00l$.

Table 19: Fraction of the tread length (l) occupied by the corner eddy and the total separation region, for the modeled riser and tread lengths

Riser/Tread	**Corner eddy (%)**	**Separation region (%)**
$0.50h/0.50l$	15.1	67.9
$0.75h/0.75l$	12.7	67.9
h/l	11.5	68.0
$1.50h/1.50l$	10.3	68.1
$2.00h/2.00l$	9.3	68.3

Table 20 presents the total production and dissipation rates calculated with equations (8.10) and (8.11) along the whole stepped spillway, for the modeled riser and tread lengths. For the largest riser and tread lengths, the total production and dissipation become higher, and it is clear that the

increments are approximately equal for both phenomena, contrary to the wall roughness variations case in Table 16 in which k_s increments cause a higher growth for production than for dissipation. The response of turbulent kinetic energy gain and loss to the step size increments, agree with the friction factor f increase predicted with equation (8.8) and presented in Table 14.

Table 20: Increase of total production and dissipation rates accomplished along the whole stepped channel, due to increasing the riser and tread lengths; with respect to $0.50h/0.50l$ values

$\frac{\textbf{\textit{Riser}}}{\textbf{\textit{Tread}}}$	**Production** ($\boldsymbol{kgm^2/ms^3}$)	**Production increase** (%)	**Dissipation** ($\boldsymbol{kgm^2/ms^3}$)	**Dissipation increase** (%)
$0.50h/0.50l$	1913.3	*Minimum*	1881.3	*Minimum*
$0.75h/0.75l$	2030.3	6.1	1992.1	5.9
h/l	2143.7	12.0	2104.0	11.8
$1.50h/1.50l$	2305.2	20.5	2269.2	20.6
$2.00h/2.00l$	2331.7	21.9	2293.3	21.9

In left and Right panels of Figure 33, the maximum values of production and dissipation rates respectively, just downstream and at the height of the step corner, are presented. In the ordinate axis, the fraction of the riser height, that is the relation between the distance measured from the step tread y_n, and the riser magnitude h, is graphed. By increasing the step dimensions, the maximum production rate value at $y_n/h \approx 1$, becomes larger; while the maximum dissipation rate value at the same location, gets smaller.

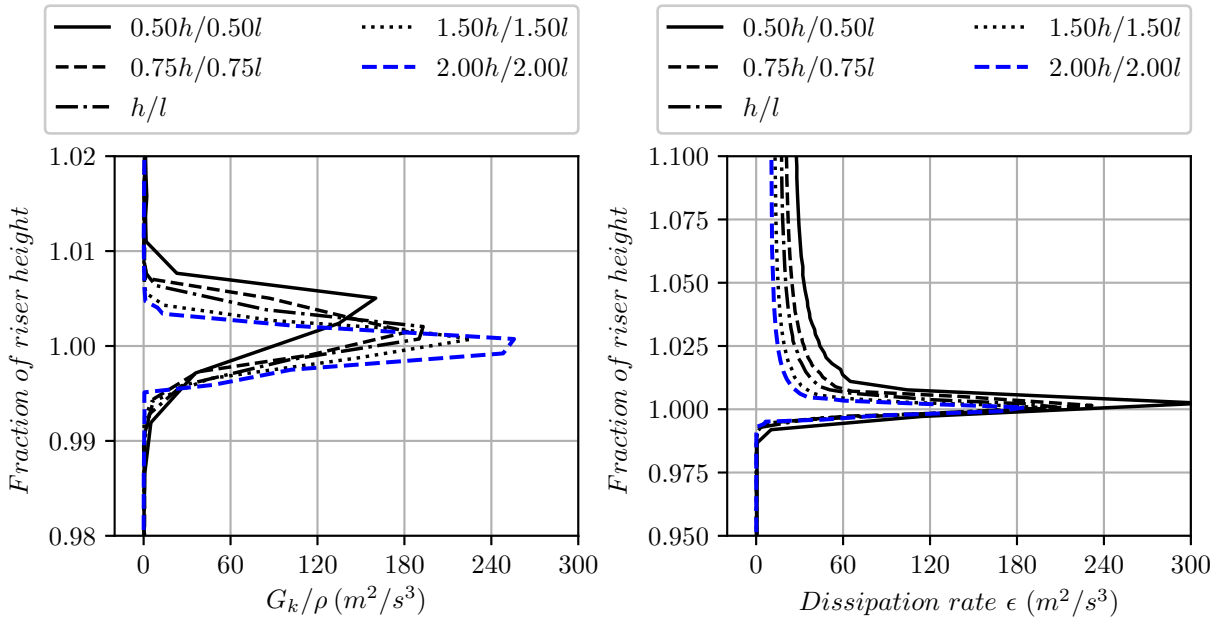

Figure 33: Turbulent kinetic energy production (*Left*) and dissipation (*Right*) rate per unit of mass profiles, for a typical tread at $0.003l$ for the modeled riser and tread lengths

At the final part of the reattachment region, the maximum production and dissipation rates close to the wall at the viscous and buffer layers, grow for the largest step dimensions modeled, as shown in the *Left* panels of Figures 34 and 35. However, at the initial part of the log-law region, at $y+ = 60$,

the production generated by the smallest steps becomes larger than the one of the biggest ones; and as shown in the *Right* panel of Figure 34, this behaviour is maintained throughout the whole logarithmic layer, and even the external boundary layer. At this external layer, the mentioned figure shows that a second production peak value is achieved, which is less than the first one, and becomes smaller for the largest step dimensions. Finally, at approximately $y+ = 2500$, the production rate generated by the largest steps overcomes again the one of the smallest ones, and maintains this way in the rest of the boundary layer.

Dissipation rate behaviour after the already mentioned maximum close to the wall at $0.95l$, is similar to the one of the production rate. The *Left* panel of Figure 35 illustrates how at the buffer region, at around $y+ = 20$, the dissipation generated by the smallest treads and risers becomes higher than the one of the largest steps. The latter is kept that way throughout the log-law region and the external boundary layer as exhibited in the *Right* panel of Figure 35, but differently from the production rate, another peak value isn't achieved; on the contrary, dissipation is less and less as the flow is further away from the solid boundary and viscous effects become negligible. At around $y+ = 2500$ (approximately the same dimensionless wall distance than for the production rate), the dissipation rate generated by the largest steps overcomes again the one of the smallest ones, and maintains this way in the rest of the boundary layer.

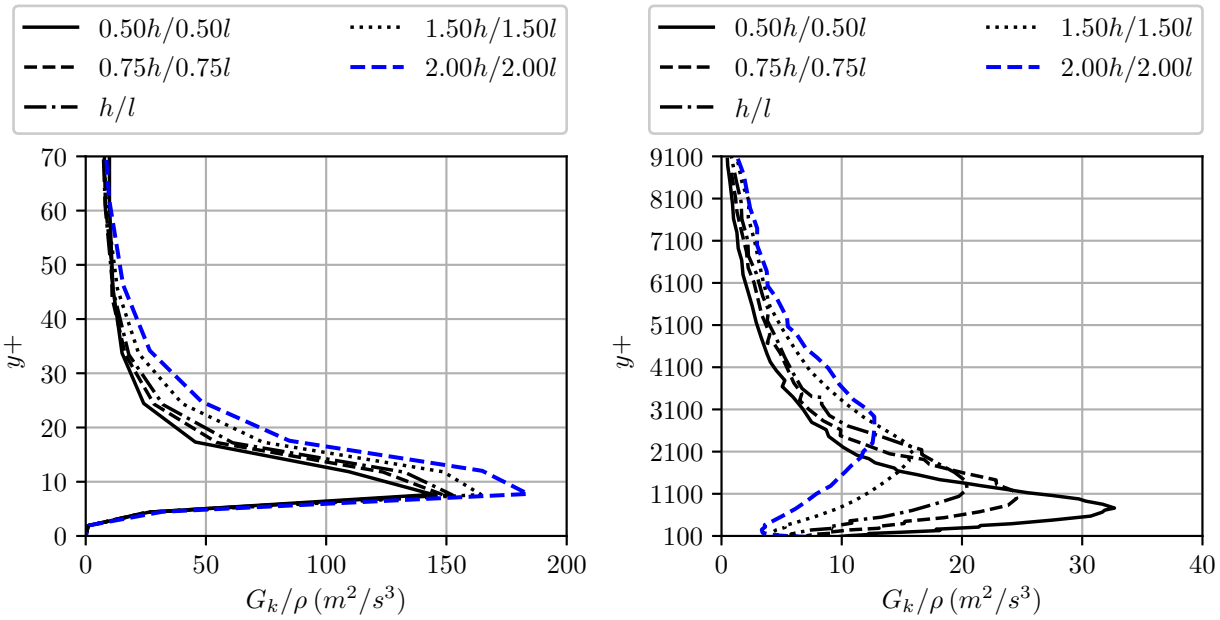

Figure 34: Turbulent kinetic energy production rate per unit of mass profiles, for a typical tread at $0.95l$ for the modeled riser and tread lengths. *Left* - close to the wall. *Right* - far from the wall

Although in the previously analyzed profiles of Figures 33, 34 and 35, there are portions where dissipation and production are higher for the largest steps dimensions, but others where they decrease as riser and tread grow; when applying equations (8.10) and (8.11), the total production and dissipation rates obtained from the summation over the separation and reattachment regions areas, become higher for largest step dimensions. For example, at a typical step, total production for $2.00h/2.00l$ model, is about 366% and 285% of total production over $0.50h/0.50l$ separation and reattachment regions respectively, in a step situated in the same abscissa; and total dissipation, of

about 369% and 301%. The above situation is simply explained by the fact that when building stepped chutes with bigger riser and treads, for one step there is a growth of the areas of the skimming flow domain in which the flow recirculation and reattachment takes place; so obviously the production and dissipation summations happen over greater flow areas, giving larger results. When considering all the steps, production and dissipation are still higher for the the largest risers and treads as shown in Table 20, but the increments with respect to the $0.50h/0.50l$ values, are lower: 21.9% for production and dissipation in the $2.00h/2.00l$ model.

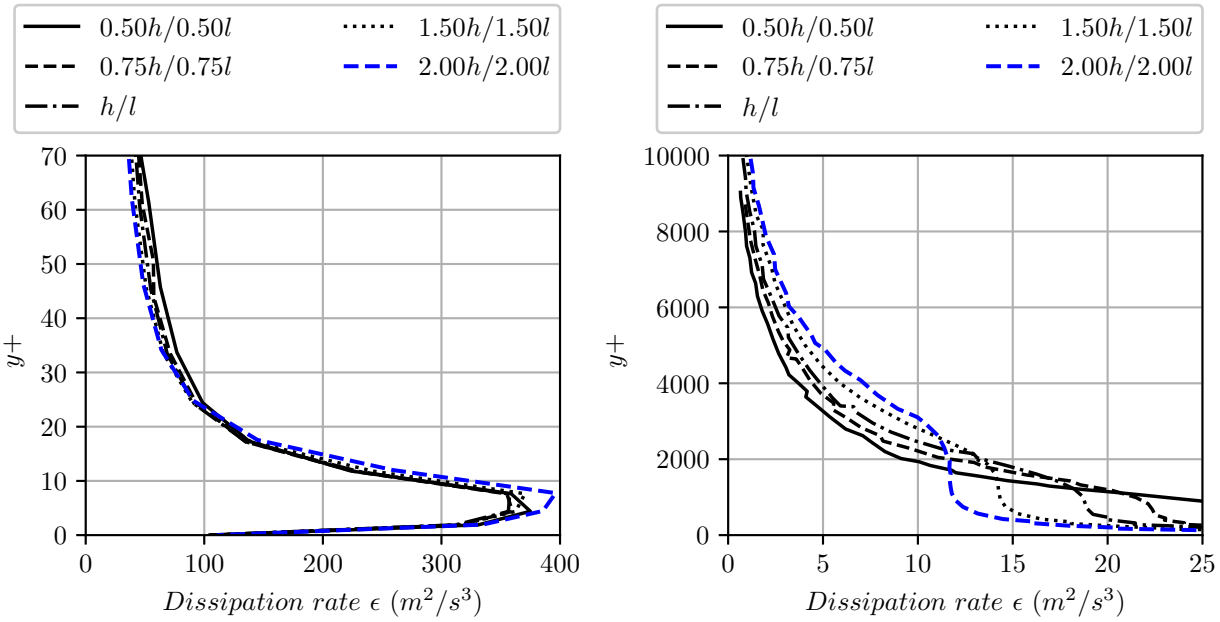

Figure 35: Turbulent kinetic energy viscous dissipation rate per unit of mass profiles, for a typical tread at $0.95l$ for the modeled riser and tread lengths. *Left* - close to the wall. *Right* - far from the wall

8.2.3 Production and dissipation rate variations due to h/l relation increments

Table 21 presents the variation of the corner eddy and the total separation region fractions of the tread length, due to increasing h/l relation.

Table 21: Fraction of the tread length (l) occupied by the corner eddy and the total separation region, for the modeled h/l relations

h/l	Corner eddy (%)	Separation region (%)
0.19	10.2	61.3
0.21	10.7	64.1
0.23	11.2	65.5
0.25	11.5	68.0

The corner eddy encompasses more and more portions of the step, as the h/l relation value gets higher. The fraction of the tread occupied by the separation region also increases as relation h/l grows, while the reattachment region spans a shorter portion of the step.

The fraction of the total turbulent kinetic energy dissipated at the separation region of a typical step, is of approximately 65% to 70% for all the modeled h/l relations, much larger than in the reattachment region, where the remaining 30% to 35% of the total is dissipated, as illustrated in Figure 36. Increasing h/l relation, together with its consequent enlargement of the separation region fraction of the tread, presented in Table 21, causes an increase in the fraction of total dissipation at the separation region, and an obvious decrease in the reattachment zone.

Figure 36 also demonstrates that the fraction of total production that takes place at the separation region, is approximately equal to the fraction of total dissipation, for all the modeled slopes. The same is valid for the reattachment region.

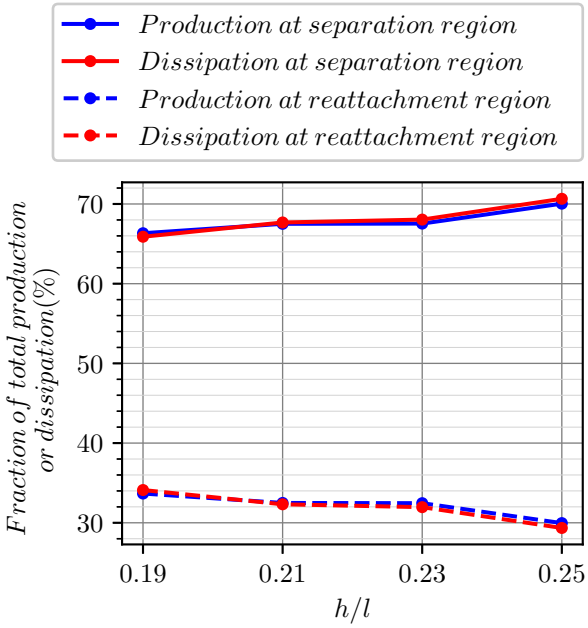

Figure 36: Fraction of total production and dissipation rates per unit channel width, at the separation and reattachment regions of a typical step, for the modeled h/l relations

It is then important to note that for the range of the relations h/l modeled, which can be described as flat slopes that guarantee SK1 sub-regime flow pattern, and for the wide ranges of roughnesses k_s (that varies from fine sands to fine ravels) and step magnitudes contemplated in the present thesis, the fraction of the total turbulent kinetic energy dissipation accomplished at the separation region of a typical step, is of approximately 70%, and the remaining 30% takes place at the reattachment region. The same deduction is valid for the fractions of total turbulent kinetic energy production accomplished at the separation and reattachment regions of a typical step, but only if smooth walls are considered. If a flat slope stepped channel with a rough bottom is projected, the above $70\% - 30\%$ relation should be reconsidered for the fractions of total production, as the reattachment region fraction shows important increments in Figure 28 as k_s gets higher, until for fine gravels ($k_s = 10mm$) the production at the separation and reattachment regions is very similar (almost $50\% - 50\%$ of the total, respectively).

Table 22 presents the total production and dissipation rates calculated with equations (8.10) and (8.11) along the whole stepped spillway, for the modeled h/l relations. For the largest pseudo-bottom slopes, the total production and dissipation become higher, and like happened for the riser and tread lengths variations, it is clear that the increments are approximately equal for both phenomena.

Table 22: Increase of total production and dissipation rates accomplished along the whole stepped channel, due to increasing the h/l relation; with respect to $h/l = 0.19$ values

h/l	Production (kgm^2/ms^3)	Production increase (%)	Dissipation (kgm^2/ms^3)	Dissipation increase (%)
0.19	1545.3	*Minimum*	1519.2	*Minimum*
0.21	1717.5	11.1	1692.2	11.4
0.23	1923.9	24.5	1884.8	24.1
0.25	2143.7	38.7	2104.0	38.7

8.2.4 Turbulent kinetic energy k

By contrasting turbulent kinetic energy production and dissipation rate contours from the *Left* and *Right* panels of Figure 25, and profiles from Figures 26 and 27, it is clear that the maximum production values found just downstream of the step corner (profile $0.003l$), don't generate a maximum k value at that point, as can be verified in Figure 37, because the highest dissipation values are achieved at that same location. Additionally, close to the riser, at the corner eddy and initial part of the primary recirculation vortex, there is no production and no dissipation, and Figure 37 shows the lowest k values. It is a region with no (or very small) turbulent fluctuations and with low velocities, where the molecular viscosity plays an important role in momentum transfer.

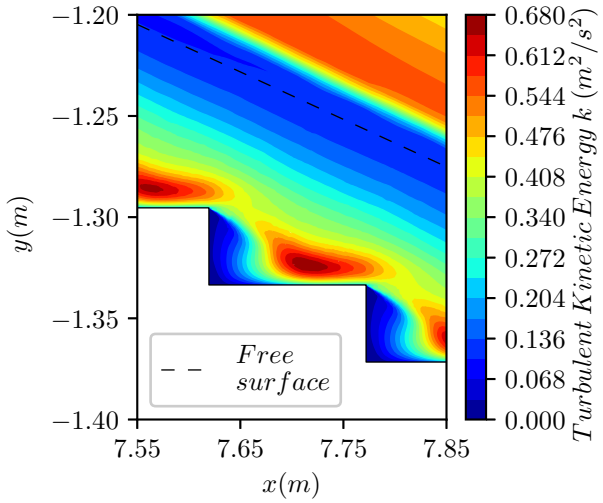

Figure 37: Turbulent kinetic energy k per unit of mass contours, modeled with $q = 0.28m^3/ms$, $k_s = 0.0mm$ and $h/l = 0.25$

Figure 37 shows that the deeper in water from the free surface, the higher the turbulent kinetic energy becomes, until the largest values are achieved around the pseudo-bottom, in the boundary

between the separation region and the main skimming flow stream passing over the recirculation vortexes. The maximum turbulent kinetic energy contour is found far from the tread wall (external boundary layer) and is coincident in each step with the final part of the separation region, and the beginning of the reattachment zone.

8.2.5 Darcy friction factor

To obtain an estimation of the friction factor f_{na} in the non-aerated flow region over a typical step, the Darcy-Weisbach expression to calculate the head loss due to the friction between the flow and a solid rough boundary is used in the present research. The original equation is multiplied by the product of the fluid density ρ, the gravity constant g and the total area occupied by the fluid over a single step A_s:

$$E_D = f_{na} \frac{L}{D} \frac{V^2}{2g} \rho g A_s \tag{8.13}$$

where:
E_D is the total flow energy dissipated per unit width of the channel (kgm^2/ms^2) in a step.
L is the length of the imaginary line joining the two outer edges of the step.
D is replaced by four times the hydraulic radius R_H, to be able to use the expression in open channel flows. In the present case, for a two-dimensional stepped spillway, R_H is approximately the flow normal depth in the non-aerated region y'_{cw}.
V is the mean flow velocity.

After some simple modifications, expression (8.13) can be rewritten as:

$$E_D = f_{na} \frac{Lq^2}{4(y'_{cw})^3 2g} \rho g A_s \tag{8.14}$$

The total dissipated energy can be related to the hydrodynamic variables of the numerical model, by calculating it as the sum of the total turbulent kinetic energy viscous dissipation rate, obtained with equation (8.11), and the total mean flow viscous dissipation rate in the step. The mean flow dissipation can be obtained by a summation of the term $2\nu S_{ij} S_{ij}$ in each cell, over the area A_s. Then, E_D would be:

$$E_D = \left(\sum_{i=1}^{n} \rho_{mi} \epsilon_i A_i + \sum_{i=1}^{n} \rho_{mi} 2\nu S_{ij} S_{ij} A_i \right) \frac{L y'_{cw}}{q} \tag{8.15}$$

It can be noticed that both, turbulent and mean flow viscous dissipation, are multiplied by Ly'_{cw}/q in expression (8.15), which is an approximation of the time a fluid particle would take to go in a straight line from the upstream to the downstream outer edges of the step. Finally, after equating expressions (8.14) and (8.15), the friction factor in the non-aerated flow region for a typical step can be estimated:

$$f_{na} = \left(\sum_{i=1}^{n} \rho_{mi} \epsilon_i A_i + \sum_{i=1}^{n} \rho_{mi} 2\nu S_{ij} S_{ij} A_i \right) \frac{8(y'_{cw})^4}{q^3 \rho A_s} \tag{8.16}$$

Table 23 shows the non-aerated flow Darcy friction factor calculated with expression (8.16), for a typical step and for the the riser and tread lengths analysed with the numerical models. The friction factor is higher as the riser and tread lengths grow, the same as the factors calculated with

Chanson *et al.* expression (8.8), and showed in Table 14. However, the factor magnitudes in Table 14 and Table 23 are not comparable because Chanson *et al.* expression is valid for f calculation when skimming flow has reached uniform flow aerated conditions. Instead, expression (8.16) is used with the present thesis numerical model results, in which the air entrainment is not captured, and hence the values from Table 23 are valid upstream the inception point.

Table 23: Non-aerated flow Darcy friction factor f_{na} for a typical step, calculated with equation (8.16) for several step sizes

Riser/Tread	$\boldsymbol{f_{na}}$
$0.50h/0.50l$	0.070
$0.75h/0.75l$	0.078
h/l	0.084
$1.50h/1.50l$	0.087
$2.00h/2.00l$	0.089

For the validation of the results from Table 23, the experimental measures from Hunt and Kadavy [42] upstream the air entrainment point are used. Between abscissas $1.83m$ and $2.44m$ of the experimental set-up of Figure 2, Hunt and Kadavy reported a head loss of $\Delta H = 0.082m$. For determining the friction factor between the abscissas, the Darcy-Weisbach expression is used:

$$f_{na} = \frac{4\Delta H(y_{cw}^{'})^3 2g}{Lq^2} \tag{8.17}$$

Despite the flow is not uniform between these two abscissas, are so close that flow normal depth change is small, therefore the average flow depth $y_{cw}^{'} = 0.086m$ is used for the calculus. Finally the f_{na} value valid for Hunt and Kadavy data between abscissas $1.83m$ and $2.44m$, is:

$$f_{na}(1.83m - 2.44m) = 0.083 \tag{8.18}$$

This result obtained from experimental data is comparable with h/l numerical model value of Table 23, which geometry and boundary conditions are a reproduction of Hunt and Kadavy's experimental set-up. Both values are approximately equal, reconfirming the numerical model prediction capabilities in the non-aerated region. An additional discussion comparing f values calculated in this thesis with the values reported in the literature, is presented in the next chapter.

9 Discussion

In Figure 11 the numerical model predictions of the specific energy H are showed for each of the measuring abscissas. The results are contrasted with the measured data from Hunt and Kadavy [5, 42], so that the numerically obtained specific energy presents a remarkable agreement with the experimental data upstream the air entrainment point in abscissa $3.05m$. With the $SST\ k-\omega$ model for turbulence and the mixture model for multiphase flow, the air entrainment to the flow was not captured and that explains the fact that the H results coefficient of variation increased from 5.65% upstream the inception point, to 11.22% downstream.

Bombardelli, Meireles and Matos [53] presented an analysis of the mean flow and turbulence in the non-aerated skimming flow region of steep stepped spillways. They used the commercial software FLOW-3D and concluded that the model needs improvement to capture the increase of flow depth due to air entrainment and the interaction of phases, stressing in the fact that it only offers a slight increment of flow depth in the aerated region, and accurate flow concentrations just close to the pseudo-bottom. About FLOW-3D it is important to mention that it has a sub-model able to simulate the natural entrainment of air due to turbulence at the free surface, which is not available in ANSYS Fluent, however it is beyond the scope of this thesis to verify the capabilities of that sub-model to quantify the air concentration downstream the inception point. However it is important to conduct further research to give clarity about whether or not that sub-model is necessary to be implemented in other commercial software like ANSYS to correctly model the aerated region. In this study, as in Bombardelli, Meireles and Matos [53], the numerical model wasn't either able to correctly model the non aerated region. Zhan, Zhang and Gong [68] obtained accurate time averaged air volume fraction profiles in the aerated region, with respect to experimental data, using LES models for turbulence and independent of the multiphase flow model: VOF or mixture. It is then important for the researches to state a conclusion of whether or not a LES model is necessary to quantify the hydrodynamic properties downstream the inception point, taking into account that the transient and 3D nature of LES, as well as its mesh resolution imply higher time and computational demands.

The Darcy friction factors obtained with equation (8.16) for several riser and tread lengths, vary from approximately $f_{na} = 0.070$ to $f_{na} = 0.090$. These results, valid in the non-aerated region, are around the friction factor obtained with experimental data from Hunt and Kadavy [5, 42] between two typical measuring abscissas located in the non-aerated region ($1.83m$ to $2.44m$ abscissas), $f_{na}(1.83m - 2.44m) = 0.083$. Chanson *et al.* [71] proposed equation (8.8) valid for $\alpha < 20°$ obtained from an adjustment to experimental data measured in approximately 38 model studies. An additional expression is deduced from an adjustment to prototype data. For prototypes, friction factor data varies from approximately 0.15 for relative step roughness height of $h\cos\alpha/D_H = 0.05$, to 4 for $h\cos\alpha/D_H = 0.2$; for models, experimental data is more scattered, and friction factor varies from approximately 0.07 to 0.15 for relative step roughness height of $h\cos\alpha/D_H = 0.2$, to approximately 0.1 to 0.2 for relative step roughness height of $h\cos\alpha/D_H = 0.6$. Different trend between model and prototype data are currently not understood. Hunt and Kadavy [5, 42] experimental set-up and h/l f_{na} value from Table 23, have a relative step roughness height of $h\cos\alpha/D_H = 0.1$ and the friction factor calculus of $f_{na} \approx 0.08$, looks to be better correlated with experimental models trend. Despite equation (8.8) friction factor f values presented in 14 vary from 0.101 to 0.129, and more expecificly for h/l riser and tread lenfths $f = 0.114$, it has to be reminded that it is an average value from model scatered information, and hence considering that friction factor decreases as $h\cos\alpha/D_H$ decreases, and that for $h\cos\alpha/D_H = 0.2$ a minimum value

of $f = 0.07$ was reported in literature, it is expected that for $h \cos\alpha / D_H = 0.1$, values close to 0.08 could be obtained. However, this comparison should be taken carefully, since the friction factor calculus for Hunt and Kadavy's data and for the numerical model results of this thesis are valid in the non-aerated region, while Chanson *et al.* [71] trends are valid for cases in which uniform aerated flow conditions are reached. This encourages to focus the research efforts in collecting data for the dissipated energy and friction factor calculus also upstream the inception point, having in mind that for short length stepped channels or large discharges, the uniform aerated conditions or even the air entrainment point could never be reached, and hence rational and empirical methods are lacking in literature to estimate flow energy dissipation in these situations.

Gonzalez, Takahasi and Chanson [44] conducted measurements in a large-size laboratory facility with two step conditions: smooth and rough, and contrary to what was expected, the results showed higher flow velocities in the aerated flow region on rough step chutes, and the inception point location further downstream than for a smooth stepped chute submitted to the same flow rate. In the present thesis, a similar study was conducted with numerical modelation of several wall roughnesses, but contrary to the results from Gonzalez, Takahasi and Chanson [44], higher production and dissipation rates of turbulent kinetic energy were obtained as the k_s values grow, and in consequence lower flow velocities than for the smooth steps case. Gonzalez, Takahasi and Chanson [44] emphasized that their conclusion was valid in the aerated region, but said nothing about the non-aerated zone where the present thesis results are valid. A possible explanation for the counterintuitive results of Gonzalez, Takahasi and Chanson, is that the roughness increment at the step faces was achieved with pourous plastic louvers, then some seepage could be seen through the screens, allowing to hypothesized that the screen porosity could has led to water infiltration through the bottom of the grid and the consequent fluid injection into the step cavity [44]. Naudascher and Rockwell [76] showed that fluid injection behind a bluff body, in this case the riser step that causes flow separation, is related with drag reduction, perhaps due to the recirculating vortex perturbation, which is responsible of part of the energy dissipation in flat slope stepped spillways. This fluid injection was not modeled in this thesis because the rough bottom is assumed to be impervious, then, secondary flows like the ones observed by Gonzalez, Takahasi and Chanson in their porous bottom, are not considered.

Studies by Amador, Sanchez-Juny and Dolz [46,47] in the non-aerated region, and by Chanson and Toombes [48], Gonzalez and Chanson [49] and Felder and Chanson [50, 51] in the aerated region, coincided in highlighting that the turbulence intensity in the mixing layer downstream the step edges, is associated with the large flow velocity gradients in there. This conclusion agrees with the high turbulent kinetic energy k values described by contours of Figure 37 obtained with the numerical models of this thesis, which are associated with the high flow velocity gradients, typical of the boundary between the recirculating vortex and the main stream passing over the pseudo-bottom.

Sánchez-Juny, Bladé and Dolz [8] observed negative prssures on the treads, at the upstream half for values of $y_c/h > 1.3$, and at the risers positive pressures were only observed close to the downstream adjacent horizontal face. These results agree with the ones numerically obtained and presented in Figure 12, where negative pressures are shown in the upstream half of the step treads, in the primary recirculating vortex domain, and in the upper portion of the riser; positive pressures are found at the riser close to the interior cavity, where the secondary recirculating vortex or corner eddy is formed. Daneshfaraz *et al.* [10] carried out several numerical modelations for various step configurations and concluded that pressure distribution behaviour was the same for all the cases, with the maximum negative value at the step outer edges; the same results that are displayed in

Figure 17 of the present thesis, where the pressure profiles predicted by the numerical model are shown along the riser height, finding their maximum values at the upper edge.

10 Conclusions

To be able to capture the hydrodynamical skimming flow variables behaviour close to the wall in flat slopes, mainly the pressure variations in the tread, it is recommended to use a near wall turbulence model, fulfilling with the mesh requirements at the boundary layer that this kind of models carry. The numerical modeler should not only be careful with the mesh resolution in the normal wall direction so that the boundary layer is solved including the viscous sub-layer, but also in the wall longitudinal direction so that the above mentioned pressure gradients in the stream-wise direction near the tread, are mesh independent. It should also be checked, if low orthogonal quality values at the tread riser intersections, affect the numerical model results; and in such a case, a punctual mesh resolution increase can be done with a vertex sizing algorithm, to improve quality at that zones. The near wall turbulence model with the above mentioned mesh specifications, is able to represent the corner eddy or secondary recirculation vortex, which is maintained due to the shear stress transfer from the primary recirculating vortex.

For the numerical models set-up performed with ANSYS Fluent in this thesis, it was not possible to capture the air entrance to the skimming flow downstream the inception point with RANS models, independently of the multiphase flow model selected: VOF or Mixture model. To be able to validate numerical model results with experimental measures downstream the inception point, a "downstream data adjustment procedure" similar to the one proposed in section 7.5.1 of this thesis, can be applied to transform potential energy due to air entrance, into kinetic energy assuming that the aerated region does not occur (as predicted by RANS models).

Upstream the inception point, the combination of $SST\ k-\omega$ + Mixture Model presents a good agreement with experimental measures: the coefficient of variation (CV) varies between 1% to 5% for numerical mean flow velocity results, with respect to data measured by the ADV and the Pitot tube, and becomes larger as it approaches the aeration region, until for abscissa $3.05m$, a maximum coefficient of variation of about 7.5% is obtained; for the mean flow normal depth, a value of $CV = 0.66\%$ demonstrates the numerical model accuracy to calculate mean flow depths. Downstream the inception point, the above mentioned "downstream data adjustment procedure" allows to compare experimental results obtained with the fiber optic probe, with numerical calculations, which are not as accurate as upstream the aeration, but are acceptable: for mean flow velocities, the CV value ranges from 5% to 11.5%; and for normal clear water depths, $CV = 1.99\%$.

By applying Prandtl boundary layer simplifications (equation (8.2)), the mean flow velocity profile curvature is found to be equal to the longitudinal pressure gradient close to the wall. For flat slope stepped channels, it was found that at the corner eddy region over the upstream portion of the tread, and at the downstream end in the reattachment zone, there is a favourable pressure gradient close to the wall, so that the mean flow velocity profile curvature is negative. However, just above the wall, due to the primary recirculating vortex effect, the curvature becomes positive. Further, close to the main stream passing over the pseudo-bottom, curvature turns to be negative again so that the profile blends smoothly with the one of the main stream. At the rest of the tread, in the contact between the primary vortex and the wall, there is an adverse pressure gradient and hence the velocity profiles curvature is positive; it keeps that way until turns to be negative at the main stream. At all the steps, negative static pressures are found in the primary vortex region, and have their maximum magnitude value at the riser upper edge; and positive static pressures at the corner eddy and the rest of the domain, that have their maximum magnitude value at the reattachment

zone.

Roughness increments imply a smaller pressure variation at the tread close to the wall, and in consequence a reduction in the magnitudes of the negative and positive pressures at the separation and reattachment regions respectively. On the contrary, at the riser, close to the wall, larger roughnesses generate larger negative pressures as the flux approaches the step edge.

Increasing the riser and tread lengths without changing the channel slope, implies a higher positive pressure at the riser base. As the recirculating vortex flows up parallel to the riser, the pressure decreases with the same gradient independent of the riser and tread lengths, and when it reaches the step edge, the maximum negative pressures are found for the largest step sizes. At the separation and reattachment regions, positive pressures are found close to the wall and are larger for the greater steps. Then, the pressures decrease as the wall distance increase, however for the recirculating vortex the pressures turn to be negative at the height of the riser upper edge, and are higher for the larger steps, while at the reattachment zone the maximum reduction is to the atmospheric pressure at the free surface (pressure never becomes negative).

Finally, bringing up turbulence, it is important to mention that the maximum values of production and dissipation are achieved at each step corner, where the maximum magnitudes of the modulus of the mean rate of-strain tensor S are found, due to the velocity gradients caused by the presence of the bottom wall upstream, and the start of the separation region downstream. At the reattachment zone, peak values of production and dissipation are found close to the wall due to the friction with the solid boundary; however, the peak of the production occurs a bit further at the buffer layer, while the one of the dissipation happens mostly at the viscous sub-layer and the initial part of the buffer layer. At the separation region, turbulent kinetic energy production and dissipation zones match the boundary between the stream passing over the pseudo-bottom, and the primary recirculating vortexes, and is due to the velocity gradients characteristic of that zone. Nevertheless, the maximum dissipation at recirculating primary vortex happens close to the wall, and is much higher than the production term.

It is also important to remark that for the range of the relations h/l modeled, and for the wide ranges of roughnesses k_s and step magnitudes considered in the present thesis; the fraction of total turbulent kinetic energy dissipation accomplished at the separation region of a typical step, is of approximately 70%; and the remaining 30% takes place at the reattachment region. The same deduction is valid for the fractions of total turbulent kinetic energy production accomplished at the separation and reattachment regions of a typical step, but only if smooth walls are considered. If a rough bottom is projected, the above $70\% - 30\%$ relation should be reconsidered for the fractions of total production, as the reattachment region fraction shows important increments as k_s gets higher, and the production at the separation and reattachment regions tends to be very similar (almost $50\% - 50\%$ of the total, respectively). The total production and dissipation rates generated along the whole stepped channel are higher for the largest roughnesses, step sizes and slopes; but as the wall roughness grows the production increments are higher than the dissipation ones; while as the step size and the pseudo-bottom slope grow, both phenomena increments are approximately equal.

With respect to turbulent kinetic energy k, it is important to mention that close to the riser, at the corner eddy and initial part of the primary recirculating vortex, there is no production and no dissipation, and the lowest k values are found. It is a region with no (or very small) turbulent fluctuations and with low velocities, where the molecular viscosity plays an important

role in momentum transfer. The maximum turbulent kinetic energy value is found in the external boundary layer and is coincident in each step with the final part of the separation region, and the beginning of the reattachment zone.

11 Recommendations for Future Investigations

Additional studies to improve the numerical model such that the air entrainment point position, the rise of the free surface due to the aeration, the interaction of the two phases and the air volume fraction profiles, can be accurately predicted. A Large Eddy Simulation is recommended to be carried out together with VOF and the mixture model, to verify if the good agreement between the numerically obtained aerated flow propeties and the measured ones, reported by Zhan, Zhang and Gong [68] in their research, is also achieved for Hunt and Kadavy's experimental data. Mean void fraction profiles are presented in Figure 3 and can be used to validate LES capability to solve the aerated region. RANS models together with a sub-model for air entrainment, similar to the one available in FLOW-3D commercial software, should also be evaluated and their performance be compared with the one of the LES. The lack of the sub-model in ANSYS fluent, and the possible issues related with the license of other commercial software that has it incorporated, can be supplied by conducing a research that includes the programming of the air entrainment sub-model into OpenFOAM, taking advantage of its open access feature and posibility to modify the source C++ code.

When a complete numerical model is finally developed, that includes an accurate simulation of the skimming flow downstream the inception point, a hydrodynamic diagnosis similar to the one performed in this thesis should be carried out to determine the pressure, velocity, turbulent kinetic energy production and dissipation field properties in the different regions of the aerated flow domain, as well as the variation due to increasing wall roughness, step sizes and the pseudo-bottom slope h/l.

A complementary investigation about the effect of wall roughness in the flow energy dissipated by the steps is required. A definite conclusion should be stated to prove whether the counter-intuitive results of Gonzalez, Takahasi and Chanson [44] of the dissipation diminution as wall roughness increase, are related or not to the fluid injection behind the primary recirculating vortex caused by the porosity of the plastic louvers with which the wall roughness was increased. A physical model of a stepped spillway can be built with a impervious roughed bottom, with several values of k_s, hopefully the same as the ones used in this thesis, to validate the numerical model results here presented.

A three-dimensional numerical model would lead to additional conclusions about the effects of the channel side walls in the flat slope skimming flow hydrodynamical variables, as well as of irregular geometries in the channel plan view; like curves, contractions and expansions. The consequences of different relations h/l (variable slope) along a same channel, are also an interesting issue to be studied.

Finally, the ANSYS Fluent capability to include more than two phases in the multiphase flow models, can be used to investigate about the characteristics of sediment transport in flat slope stepped channels, and conclude about the sediment magnitudes that can be trapped by the recirculation vortexes and analyse if that solid particles settle due to the low velocities in that zone, perhaps generating the disappearance of the separation regions.

References

[1] D. Kositgittiwong, "Validation of Numerical Model of the Flow Behaviour through Smooth and Stepped Spillways using Large Scale Physical Model," Ph.D. dissertation, King Mongkuts University of Technology Thonburi, 2012.

[2] S. Llano, "Hydraulics of Stepped Structures - Importance of Flow Regimes on Stepped Chutes and Practical Application in Developing Countries," Ph.D. dissertation, UNESCO - IHE, 2003.

[3] J. G. Chatila and B. R. Jurdi, "Stepped Spillway as an Energy Dissipater," *Canadian Water Resources Journal*, vol. 29, no. 3, pp. 147–158, 2004.

[4] H. Chanson, "Two-phase air-water flows: Scale effects in physical modeling," *Journal of Hydrodynamics*, vol. 26, no. 2, pp. 291–298, 2014.

[5] S. Hunt and K. Kadavy, "Energy Dissipation on Flat Sloped Stepped Spillways: Part 2. Downstream of the Inception Point," *Transactions of the American Society of Agricultural and Biological Engineers*, vol. 53, no. 1, pp. 111–118, 2010.

[6] H. Chanson, *The Hydraulics of Stepped Chutes and Spillways*, 2002.

[7] R. M. Boes and W. H. Hager, "Two-Phase Flow Characteristics of Stepped Spillways," *Journal of Hydraulic Engineering*, vol. 129, no. 9, pp. 661–670, sep 2003.

[8] M. Sánchez-Juny, E. Bladé, and J. Dolz, "Analysis of pressures on a stepped spillway," *Journal of Hydraulic Research*, vol. 46, no. 3, pp. 410–414, may 2008.

[9] A. Amador, M. Sánchez-Juny, and J. Dolz, "Developing Flow Region and Pressure Fluctuations on Steeply Sloping Stepped Spillways," *Journal of Hydraulic Engineering*, vol. 135, no. 12, pp. 1092–1100, dec 2009.

[10] R. Daneshfaraz, A. R. Joudi, A. Ghahramanzadeh, and A. Ghaderi, "INVESTIGATION OF FLOW PRESSURE DISTRIBUTION OVER A STEPPED SPILLWAY," *Advances and Applications in Fluid Mechanics*, vol. 19, no. 4, pp. 811–828, dec 2016.

[11] H. Chanson, "Hydraulics of Skimming Flows over Stepped Channels and Spillways," *Journal of Hydraulic Research*, vol. 32, pp. 445–460, 1994.

[12] S. Fortier and F. C. Scobey, "Permissible Canal Velocities," *Transactions of the American Society of Civil Engineers*, vol. 89, pp. 940–956, 1926.

[13] J. R. Dubler and N. S. Grigg, "Dam Safety Policy for Spillway Design Floods," *Journal of Professional Issues in Engineering Education and Practice*, vol. 122, no. 4, pp. 163–169, oct 1996.

[14] H. Chanson and L. Toombes, "Hydraulics of stepped chutes: The transition flow," *Journal of Hydraulic Research*, vol. 42, no. 1, pp. 43–54, 2004.

[15] Y. Yasuda and I. Ohtsu, "Flow resistance of skimming flow in stepped channels," IAHR Congress, Graz, Tech. Rep., 1999.

[16] H. Chanson, "A TRANSITION FLOW REGIME ON STEPPED SPILLWAYS THE FACTS," 2001.

[17] J. H. Ferziger and M. Perić, *Computational Methods for Fluid Dynamics*. Berlin, Heidelberg: Springer Berlin Heidelberg, 2002.

[18] H. K. Versteeg and W. Malalasekera, *An introduction to computational fluid dynamics: the finite volume method*. Pearson Education Ltd, 2007.

[19] ANSYS, *ANSYS Fluent Theory Guide*, 2013, vol. 15.

[20] D. C. Wilcox, *Turbulence Modeling for CFD*, 1st ed. La Cañada, California: DCW industries, Inc, 1993.

[21] G. Tryggvason, D. Juric, J. Che, M. R. H. Nobari, and S. Nas, "Computations of Multiphase Flows by a Finite Difference/Front Tracking Method," *LECTURE SERIES-VON KARMAN INSTITUTE FOR FLUID DYNAMICS*, 1998.

[22] K. Hiltunen, A. Jäsberg, S. Kallio, H. Karema, M. Kataja, A. Koponen, M. Manninen, and V. Taivassalo, *Multiphase Flow Dynamics Theory and Numerics*. VTT, 2009.

[23] M. Manninen, V. Taivassalo, S. Kallio, and Å. Akademi, *On the mixture model for multiphase flow*, VTT Publications, Ed. Espoo: Technical Research Centre of Finland, 1996.

[24] L. Schiller and A. Naumann, "A drag coefficient correlation," *Z. Ver. Deutsch. Ing*, vol. 77, pp. 318–320, 1935.

[25] J. Matos and I. Meireles, "Hydraulics of stepped weirs and dam spillways: engineering challenges, labyrinths of research," in *Hydraulic structures and society - Engineering challenges and extremes*. The University of Queensland, jan 2014, pp. 1–30.

[26] M. F. Young, "Feasibility Study of a Stepped Spillway," in *Hydraulics Division Speciality Conference, ASCE*, 1982, pp. 96–106.

[27] R. M. Sorensen, "Stepped Spillway Hydraulic Model Investigation," *Journal of Hydraulic Engineering*, vol. 111, no. 12, pp. 1461–1472, dec 1985.

[28] D. Stephenson, "Energy dissipation down stepped spillways," *Water Power and Dam Construction*, vol. 43, pp. 27–30, 1991.

[29] G. C. Christodoulou, "Energy Dissipation on Stepped Spillways," *Journal of Hydraulic Engineering*, vol. 119, no. 5, pp. 644–650, may 1993.

[30] H. Chanson, "Comparison of energy dissipation between nappe and skimming flow regimes on stepped chutes," *Journal of Hydraulic Research*, vol. 32, no. 2, pp. 213–218, jan 1994.

[31] H. Chanson, "Air Entrainment in Open Channel Flow: Application to Spillways," *La Houille Blanche*, vol. 47, no. 4, pp. 277–286, jan 1992.

[32] F. Hartung and H. Scheuerlein, *Design of overflow rockfill dams*. Paris: Commission internationale des grands barrages, 1970.

[33] H. Chanson and L. Toombes, "Experimental investigations of air entrainment in transition and skimming flows down a stepped chute: application to enbankment overflow on stepped spillways," *Canadian Journal of Civil Engineering*, vol. 29, no. 1, pp. 145–156, 2002.

[34] H. Chanson, *Hydraulic design of stepped cascades, channels, weirs, and spillways.* Pergamon, 1994.

[35] R. Boes and H. Minor, "Hydraulic design of stepped spillways for RCC dams," *International Journal of Hydropower and Dams*, no. 3, pp. 87–91, 2002.

[36] H. Chanson, "Air bubble entrainment in open channels: Flow structure and bubble size distributions," *International Journal of Multiphase Flow*, vol. 23, no. 1, pp. 193–203, feb 1997.

[37] H. Chanson and L. Toombes, "Energy Dissipation and Air Entrainment in Stepped Storm Waterway: Experimental Study," *Journal of Irrigation and Drainage Engineering*, vol. 128, no. 5, pp. 305–315, oct 2002.

[38] H. Chanson, "Discussion of Inception Point Relationship for Flat-Sloped Stepped Spillways by Sherry L. Hunt and Kem C. Kadavy," *Journal of Hydraulic Engineering*, vol. 138, no. 11, pp. 1002–1004, nov 2012.

[39] M. Pfister, W. H. Hager, and H.-E. Minor, "Bottom Aeration of Stepped Spillways," *Journal of Hydraulic Engineering*, vol. 132, no. 8, pp. 850–853, aug 2006.

[40] A. S. Zamora, M. Pfister, W. H. Hager, and H.-E. Minor, "Hydraulic Performance of Step Aerator," *Journal of Hydraulic Engineering*, vol. 134, no. 2, pp. 127–134, feb 2008.

[41] J. Matos and I. Meireles, "Skimming Flow in the Nonaerated Region of Stepped Spillways over Embankment Dams," *Journal of Hydraulic Engineering*, vol. 135, no. 8, pp. 685–689, aug 2009.

[42] S. Hunt and K. Kadavy, "Energy Dissipation on Flat Sloped Stepped Spillways: Part 1. Upstream of the Inception Point," *Transactions of the American Society of Agricultural and Biological Engineers*, vol. 53, no. 1, pp. 103–109, 2010.

[43] S. André, "High velocity aerated flow on stepped chutes with macro-roughness elements," Ph.D. dissertation, jan 2004.

[44] C. A. Gonzalez, M. Takahasi, and H. Chanson, "An experimental study of effects of step roughness in skimming flows on stepped chutes," *Journal of Hydraulic Research*, vol. 46, no. 1, pp. 24–35, 2008.

[45] S. Felder and H. Chanson, "ENERGY DISSIPATION DOWN A STEPPED SPILLWAY WITH NON- UNIFORM STEP HEIGHTS," *Journal of Hydraulic Engineering*, vol. 137, no. 11, pp. 1543–1548, 2011.

[46] A. Amador, M. Sanchez-Juny, and J. Dolz, "DPIV study of the turbulent boundary layer over V-shaped cavities," in *Proceedings of the International Conference on Fluvial Hydraulics River Flow*, Lisbon, Portugal, 2006, pp. 1813–1821.

[47] A. Amador, M. Sanchez-Juny, and J. Dolz, "Characterization of the Nonaerated Flow Region in a Stepped Spillway by PIV," *Journal of Fluids Engineering*, vol. 128, no. 6, p. 1266, nov 2006.

[48] H. Chanson and L. Toombes, "AIR-WATER FLOWS DOWN STEPPED CHUTES : TURBULENCE AND FLOW STRUCTURE OBSERVATIONS," *Intl Jl of Multiphase Flow*, vol. 28, no. 11, pp. 1737–1761, 2002.

[49] C. A. Gonzalez and H. Chanson, "Turbulence and cavity recirculation in airwater skimming flows on a stepped spillway," *Journal of Hydraulic Research*, vol. 46, no. 1, pp. 65–72, 2008.

[50] S. Felder and H. Chanson, "Turbulence, dynamic similarity and scale effects in high-velocity free-surface flows above a stepped chute," *Experiments in Fluids*, vol. 47, no. 1, pp. 1–18, jul 2009.

[51] S. Felder and H. Chanson, "Triple decomposition technique in airwater flows: Application to instationary flows on a stepped spillway," *International Journal of Multiphase Flow*, vol. 58, pp. 139–153, jan 2014.

[52] M. Tabbara, J. Chatila, and R. Awwad, "Computational simulation of flow over stepped spillways," *Computers & Structures*, vol. 83, no. 27, pp. 2215–2224, 2005.

[53] F. A. Bombardelli, I. Meireles, and J. Matos, "Laboratory measurements and multi-block numerical simulations of the mean flow and turbulence in the non-aerated skimming flow region of steep stepped spillways," *Environmental Fluid Mechanics*, vol. 11, no. 3, pp. 263–288, 2011.

[54] S. Benmamar, A. Kettab, and C. Thirriot, "Numerical Simulation of Turbulent Flow Upstream of the Inception Point in a Stepped Channel," in *30th IAHR Congress*, Thessaloniki, 2003.

[55] K. Unami, T. Kawachi, M. M. Babar, and H. Itagaki, "Two-Dimensional Numerical Model of Spillway Flow," *Journal of Hydraulic Engineering*, vol. 125, no. 4, pp. 369–375, apr 1999.

[56] R. F. de Carvalho and A. T. Amador, "Physical And Numerical Investigation of the Skimming Flow Over a Stepped Spillway," in *Advances in Water Resources and Hydraulic Engineering*. Berlin, Heidelberg: Springer Berlin Heidelberg, 2009, pp. 1767–1772.

[57] K. Morovati, A. Eghbalzadeh, and M. Javan, "Numerical investigation of the configuration of the pools on the flow pattern passing over pooled stepped spillway in skimming flow regime," *Acta Mechanica*, vol. 366, pp. 353–366, 2015.

[58] R. Tadayon and A. S. Ramamurthy, "Turbulence Modeling of Flows over Circular Spillways," *Journal of Irrigation and Drainage Engineering*, vol. 135, no. 4, pp. 493–498, aug 2009.

[59] B. Chakib and H. Mohammed, "Numerical Simulation of Air Entrainment for Flat-sloped Stepped Spillway," *Journal of Computational Multiphase Flows*, vol. 7, no. 1, 2015.

[60] G. Zhang and H. Chanson, "Self-aeration in the rapidly- and gradually-varying flow regions of steep smooth and stepped spillways," *Environmental Fluid Mechanics*, 2015.

[61] Z. Qian, X. Hu, W. Huai, and A. Amador, "Numerical simulation and analysis of water flow over stepped spillways," *Science in China Series E: Technological Sciences*, vol. 52, no. 7, pp. 1958–1965, jul 2009.

[62] S. Li, S. Cain, M. Wosnik, C. Miller, H. Kocahan, and R. Wyckoff, "Numerical Modeling of Probable Maximum Flood Flowing through a System of Spillways," *Journal of Hydraulic Engineering*, vol. 137, no. 1, pp. 66–74, jan 2011.

[63] F. Bombardelli, "Computational multi-phase fluid dynamics to address flows past hydraulic structures," in *4th IAHR International Symposium on Hydraulic Structures*, 2012.

[64] J. Matos, K. H. Frizell, S. André, and K. W. Frizell, "On the Performance of Velocity Measurement Techniques in Air-Water Flows," in *Hydraulic Measurements and Experimental Methods 2002*. Reston, VA: American Society of Civil Engineers, oct 2002, pp. 1–11.

[65] "OpenFOAM — Free CFD Software — The OpenFOAM Foundation." [Online]. Available: https://openfoam.org/

[66] Instituto Nacional de Vías - Colombia, *Normas de Ensayo de Materiales para Carreteras sección 100 - SUELOS*, 2012.

[67] P. K. Kundu, I. M. Cohen, and D. R. Dowling, *Fluid Mechanics*, 5th ed., 2012, vol. 40, no. 6.

[68] J. Zhan, J. Zhang, and Y. Gong, "Numerical investigation of air-entrainment in skimming flow over stepped spillways," *Theoretical and Applied Mechanics Letters*, vol. 6, no. 3, pp. 139–142, may 2016.

[69] W. Rodi, G. Constantinescu, and T. Stoesser, *Large-eddy simulation in hydraulics*. CRC Press/Balkema, 2013.

[70] ANSYS, *ANSYS Fluent User's Guide*, 2013.

[71] H. Chanson, Y. Yasuda, and I. Ohtsu, "Flow Resistance in Skimming Flows in Stepped Spillways and its Modelling," *Can Jl of Civ. Eng*, vol. 29, no. 6, pp. 809–819, 2002.

[72] F. Scarano and M. L. Riethmuller, "Iterative multigrid approach in PIV image processing with discrete window offset," *Experiments in Fluids*, vol. 26, no. 6, pp. 513–523, may 1999.

[73] L. M. Hudy, A. Naguib, and W. M. Humphreys, "Stochastic estimation of a separated-flow field using wall-pressure-array measurements," *Physics of Fluids*, vol. 19, 2007.

[74] D. M. Driver and H. L. Seegmiller, "Features of a reattaching turbulent shear layer in divergent channelflow," *AIAA Journal*, vol. 23, no. 2, pp. 163–171, feb 1985.

[75] T. Cebeci and P. Bradshaw, *Momentum transfer in boundary layers*. New York: Hemisphere Publishing Corp., 1977.

[76] E. Naudascher and D. Rockwell, *Flow-induced vibrations : an engineering guide*, 1994.